Magnetoelasticity for Integration of Quantum Defects

Adi Jung

Electrical Engineering and Computer Sciences
University of California, Berkeley

Technical Report No. UCB/EECS-2024-42
http://www2.eecs.berkeley.edu/Pubs/TechRpts/2024/EECS-2024-42.html

May 1, 2024

Acknowledgement

Would like to thank my advisor Sayeef Salahuddin, committee members Boubacar Kante, Clark Nguyen, and Alex Pines for their time and advice over the years. Would also like to thank Dominic Labanowski for his mentorship.

Magnetoelasticity for Integration of Quantum Defects

By

Adi Jung

A dissertation submitted in partial satisfaction of the

requirements for the degree of

Doctor of Philosophy

in

Engineering - Electrical Engineering and Computer Sciences

in the

Graduate Division

of the

University of California, Berkeley

Committee in charge:

Professor Sayeef Salahuddin, Chair
Associate Professor Boubacar Kante
Professor Clark Nguyen
Dr. Dominic Labanowski

Fall 2023

Magnetoelasticity for Integration of Quantum Defects

Abstract

Magnetoelasticity for Integration of Quantum Defects

by

Adi Jung

Doctor of Philosophy in Engineering - Electrical Engineering and Computer Sciences

University of California, Berkeley

Professor Sayeef Salahuddin, Chair

Integration of atomic-defect spin qubits into memory or computing remains a challenging task due to a range of engineering problems, including microwave power delivery and material compatibility. While approaches exploiting spin-wave dipolar coupling have been explored in the past, they are reliant on Yttrium Iron Garnet (YIG), a model magnetic material which displays long spin coherence length, but cannot be integrated on-chip except under relatively restrictive conditions. Therefore, despite a growth in research interest in recent years, such hybrid quantum magnonic systems currently remain confined to laboratory conditions.

In this thesis, I will present a method by which surface acoustic wave (SAW) driven magnetoelastic waves can be used as an effective near-field antenna for interfacing with spin qubits. Beginning with a set of experiments on resonant coupling of acoustic waves to magnetic dynamics, we will show that the magnetoelastic interaction acts as linear method of conversion of acoustic waves into magnetic dynamics at high microwave power levels. Following this, experimental results demonstrating a dipolar coupling to the nitrogen-vacancy center in diamond will be shown, along with a set of conditions under which this dipolar coupling is dominant over incoherent off-resonant coupling mechanisms. With these conditions identified, we implement them and demonstrate the phase-coherent coupling of acoustic waves to nitrogen-vacancy dynamics mediated by a magnetoelasticity in a ferromagnet. This approach is in theory applicable across a wide range of materials, and offers the capability to integrate atomic qubits in a more power efficient manner compatible with commercial nanofabrication.

To my parents, who have made everything possible.

Contents

List of Figures

List of Tables

Acknowledgments

To begin with, I would like to thank my advisor Professor Sayeef Salahuddin, for his support throughout the duration of my PhD. Coming into the program, I had some confidence in my ability to solve technical problems on paper, but I quickly learned that practical progress involved much more than just academic knowledge. Sayeef's patience and suggestions as I worked through challenges were critical to my learning experience, and I can attribute a great deal of my current skillset and growth to his willingness to lend me a great deal of rope to work with. Beyond his advice, I have consistently been impressed by Sayeef's imaginative approaches to problem solving, and for me he remains a reminder of just how much more can be done. I'm certain that my PhD experience will be valuable for the rest of my life, both personally and professionally, and I will always be grateful for his willingness to give me this opportunity.

I would also like to thank my collaborators, Professor Ausrine Bartasyte and Samuel Margueron from Institute FEMTO-ST institute and frecInIsys, without whom much of this work would not have been possible. It is impossible for any one person to solve every problem, and the work she and her group did to fabricate IDTs accelerated every piece of the work in this thesis. Though our opportunities to chat face to face were rare due to the time difference, I look forward to opportunities to work together again in the future. I would also like to thank Dr. Walid Redjem and Dr. Satcher Hsieh for going out of their way to help a confused graduate student solve optics problem out of the blue. Also, thank you to Dr. Jan Rhensius and the QZabre AG team for going well beyond any reasonable expectations to support my research over our brief week together.

A big thank you also goes to the members of the NSF TANMS center, particularly the members of the 2D and Materials thrusts for their collaborative support. As someone pursuing a research project somewhat separated from the interests of my broader research group, having experienced and passionate researchers with a diverse set of backgrounds and experiences to count on for input and feedback was invaluable to my progress. In addition, TANMS acted as a great source in my studies, as I was regularly exposed to the center's wide-ranging research across multiple domains of engineering, a source of much needed breadth in understanding.

I of course must thank my fellow members of the Salahuddin research group, who maintained my strings of sanity throughout both my undergraduate and graduate years. Thanks go to almost a decade's worth of students, including Korok, Niklas, Ava, Pratik, Chirag, Nirmaan and many more for helping build and maintain a fun community over such a long period of my life. Thanks also to the members of the spin group, Jason and Steve; whether productive or not, our chats and discussions always had a positive effect. Thanks to my cubicle mate and fellow UC Berkeley undergrad survivor Saavan for putting up with my questionably coherent ranting for 6 years – with any luck they will continue in years to come. Lastly, thank you to Dominic; I probably would never have pursued graduate studies without your mentorship during my undergrad years, and I don't regret a second of it.

Chapter 1

Introduction

Originally identified in the mid-19th century by Joule [1], the coupling between elastic deformation and magnetization known as magnetostriction has been a well known property of ferromagnetic materials for almost two centuries. While its existence was known early, much of the scientific study of magnetostriction occurred in the 1950s-1960s, where an exceptionally strong resonant absorption of elastic waves in magnetic films was theoretically predicted [2]. Typical studies of magnetoelasticity at this time typically utilized the resonant damping magnetic films as a source of acoustic waves [3] due to technological limitations of the time. While radar and microwave technology had made it possible to generate GHz electromagnetic excitation with relative ease, excitation of acoustic waves within that frequency range was considerably more challenging.

The study of magnetoelasticity saw a further resurgence in the 1980s, along with the development of the surface acoustic wave (SAW) filter technology [4]. Such piezoelectric SAW filters saw use in early cell-phones as high frequency filters, and SAW delay-lines offered an ideal platform for applying acoustic wave excitation to magnetic thin films and exploring reciprocal effects of the studies of yesteryear. At this time, experimental data began to confirm the theoretical predictions of exceptionally high power absorption made decades prior [5], and early devices relying on SAW-driven magnetic dynamics were proposed and tested [6]. Despite this progress, technological limitations of the time remained a constraint, as the maximum operating frequency of the piezoelectric interdigital transducers (IDTs) was set by the speed of sound and the minimum feature size of photolithographic devices. Devices of this time approached the GHz regime, but were typically too low-frequency to efficiently overlap with magnetic resonances. However, as Moore's law progressed, sub-micron feature fabrication became reliably feasible, and SAW delay lines within the GHz regime became accessible. This progress in SAW technology has, in the modern day, created a wide-ranging toolbox of capabilities, ranging across multidisciplinary fields including quantum information processing, microfluidics, and communication [7].

Utilizing these advances, the theoretical predictions of efficient magnetoelastic absorption made by Kittel 60 years prior could be directly confirmed, and were done so in the 2010s [8]. Around this time, parallel developments in materials science and micro-electromechanical

systems (MEMS) had led to a growth in studies of magnetoelectric materials such as bismuth ferrite, and piezoelectric-ferromagnet bilayers slotted well into the growing field of composite multiferroics [9, 10]. As a result, a range of novel methods for applying high frequency strain to ferromagnetic materials became available, offering wide-ranging applications in sensing, filters, and energy harvesting.

Independent of the study of multiferroic systems, atomic defects in carbon and silicon lattices have seen significant interest in the 21st century as potential implementations of quantum bits. While a range of such defects have been studied, the nitrogen-vacancy (NV) center in diamond has been the model system that has been studied in the most depth. Originally discovered in 1976 [11] in a study of optical fluorescence of nitrogen defects in diamond; subsequent studies showed that the NV center displayed a spin-dependent fluorescence and exceptionally long room-temperature spin coherence time, making it a plausible candidate for solid state quantum information processing [12].

Wide ranging studies of the NV center over the past few decades have established a strong understanding of its electronic structure and quantum performance, and diamond processing techniques have improved significantly over the same time. The nitrogen vacancy center consists of a substitutional nitrogen atom adjacent to a vacancy within the tetrahedral carbon lattice of diamond. Under typical conditions, an electron from the diamond lattice ionizes the NV center, resulting in the nitrogen atom containing four electrons in its 2p orbital states, leaving two holes. These holes together behave as a spin-1 particle whose electronic states lie within the relatively wide band-gap of diamond, limiting interactions with the continuum of electronic states within diamond's conduction and valence bands and contributing to the NV center's exceptionally long room temperature spin coherence time. These states have been well-characterized both through a various spectroscopic techniques [12] and theoretically following a symmetry and group theory approach [13].

Beyond a long spin-coherence time, the NV center displays another property which makes it an exciting prospect for study, namely the capability to readout its spin state via optical fluorescence intensity. The ground state of the NV center contains a three level system with a fine structure splitting of approximately 2.87 GHz at room temperature. When the spin-1 particle is excited to a higher energy state optically, if it sits in the $m_s = 0$ initial state , it radiates a visible photon, while if it sits in the $m_s = \pm 1$ state, it takes a series of non-radiative transitions, returning to the $m_s = 0$ state with a high probability. In addition to spin dependent readout, this also offers a simple method of initializing the NV center to a known state, as an exciting laser pulse will polarize an NV center into the $m_s = 0$ initial state, where it will remain over a timescale of up to milliseconds [14], depending on sample quality and coherence time. A simple model of this process is overviewed in Figure 1.1. This model is sufficient to understand the data discussed in this thesis, however, NV centers are sensitive to a wide range of external factors, including strain, magnetic and electric fields, and temperature, which can introduce significant complexity into the system. As a consequence of these properties, the NV center has been a promising candidate for defect-based quantum information processing for over a decade [15].

Yet, despite this, practical applications of the NV center in magnetometry and quan-

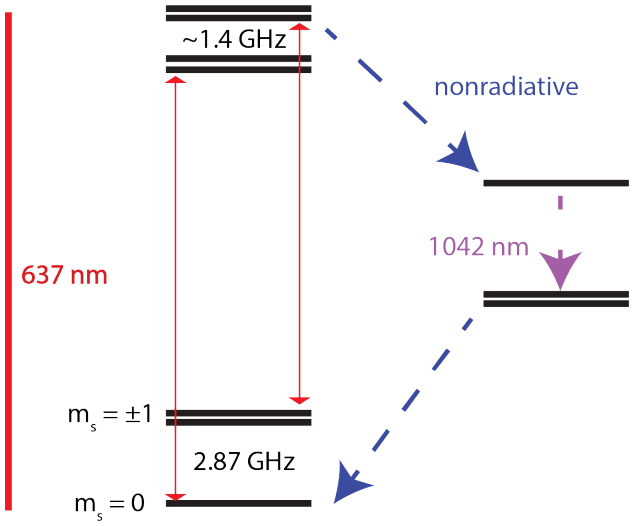

Figure 1.1: Simple model of the NV center spin-dependent fluorescence. Depending on initial occupied state, the NV center fluorescence intensity in the visible regime will shift. This provides a simple method of reading out the NV spin-state, and enables various schemes for spin-photon entanglement, a valuable tool for quantum information processing.

tum computing remain elusive for a range of engineering reasons. One such challenge in integration of NV centers is a practical method of driving spin transitions at low power. Typical laboratory approaches utilize antennas or microwave striplines to generate GHz fields [16, 17, 18], but these approaches almost invariably require exceptionally large input power, and designing such antennas in a way that enables uniform excitation of large area ensembles without unacceptable microwave power variation remains a challenging problem. An alternative acoustic approach to coherent control of NV centers has been experimentally demonstrated [19, 20] as well, exploiting acoustic perturbations on the NV center energy levels, but this approach again requires relatively high microwave power consumption, typically between 100 mW and 1 W.

As such, here lies the original motivation for the work presented in the following thesis. The excitation of magnetic dynamics in a power efficient manner is a significant challenge, but an acoustically driven approach has been well-established as an effective attack vector to the problem. Hybrid quantum magnonic systems are an emerging area of study showing promise for effectively driving atomic quantum defects [21, 22], and by exploiting the strength of spin-wave dipolar stray fields, such systems have been shown to reduce the power required to drive NV centers [23]. Even in this systems, however, a significant source of power inefficiency is linked to the initial excitation of spin wave dynamics, for which magnetoelasticity offers a promising solution. Conveniently, as fabrication technology has advanced, it has become readily possible to excite surface acoustic waves in frequency ranges comparable

to the NV center magnetic resonance, and using magnetic bias field to tune the coupling via the Zeeman effect. Magnetoelastic excitation of resonant spin dynamics in comparable frequency ranges has been shown experimentally to be orders of magnitude more power efficient than more traditional waveguide excitation [24], and large fluorescence shifts in NV centers in proximity to resonant magnetoelastic dynamics have already been observed [25], indicating that acoustic excitation of spin waves may have the potential to outperform traditional hybrid magnonics.

Another separate challenge associated with hybrid magnonics is that it largely remains restricted to magnetic systems optimized for quantum coherence, such as the model system Yttrium Iron Garnet (YIG). YIG displays low magnetic damping and long spin wave coherence lengths, but is challenging to integrate on-chip, as epitaxial thin film growth of YIG requires a lattice-matched Gadolinium Gallium Garnet (GGG) substrate [26]. Because the low damping of YIG is critical to the coherence of these interactions, attempts to substitute it have been challenging, and proposed alternative magnetic materials are highly specialized [27]. By investigating the coupling of magnetoelastic systems to such atomic quantum defects, we hypothesize that a more practical approach to quantum system integration could emerge based on magnetoelastic coupling, piggybacking on established fabrication technology, possibly with additional flexibility in material design and engineering.

Initial studies focused on ensuring that the underlying magnetoelastic excitation dynamics scaled effectively to the power levels required for effective excitation of atomic quantum systems without unreasonable power consumption. Following an effective demonstration of this performance, studies of direct coupling were undertaken, and it was found that the coupling mechanisms could be distinguished into two separate regimes, and dipolar models previously established for traditional spin wave excitation were effective at predicting the coupling mechanism. This initial work also provided the insight required to predict the conditions under which a phase-coherent coupling between magnetoelastic waves and NV centers might be possible. Finally, the coherent coupling between magnetoelastic waves and NV centers was demonstrated via the observation of Rabi oscillations, confirming that a magnetoelastic approach is viable and performant even under academic design and fabrication.

This thesis describes my work on magnetoelastic wave driven quantum systems, and is divided into six chapters:

1. This introductory chapter discusses the historical context and motivations behind pursuing the work discussed in the thesis.

2. The second chapter introduces the underlying physics of magnetoelasticity, acoustically-driven ferromagnetic resonance (ADFMR), and experimental work demonstrating its performance at high microwave powers.

3. The third chapter provides an overview of the construction of a optical test setup capable of characterizing NV center dynamics compatible with a magnetoelastic device.

4. Chapter four provides an overview and detailed discussion of experimental results collected from the optical test setup detailed in the prior chapter.

5. The penultimate chapter discusses the work performed using a commercial NV characterization microscope to demonstrate coherent coupling to magnetoelastic waves.

6. Finally, a summary of the total work in the thesis is provided, along with a discussion of various proposed next steps and possible avenues for further development of the work.

Chapter 2

Acoustically Driven Ferromagnetic Resonance

The phenomenon of acoustically driven ferromagnetic resonance (ADFMR) has gained attention in recent years in a number of novel application spaces. The theoretical framework for ADFMR was initially developed by Kittel in 1956, who predicted a highly efficient conversion of energy from acoustic phonons into spin wave modes of a ferromagnetic film.[2] Typical experiments by Kittel's contemporaries studied the phenomenon by evaporating a magnetic film onto a quartz rod, driving the film into ferromagnetic resonance, and measuring the amplitude of the generated acoustic wave via a microwave cavity.[3, 28]. In recent years, photolithography and nanofabrication techniques have advanced to the point where GHz surface acoustic waves (SAWs) can be transmitted and received via interdigitated transducers (IDTs).[4] This has enabled a variety of novel studies of magnetoelasticity in thin films, including film characterization [29, 30] and interactions with quantum defects.[25] ADFMR has also been explored for use in various commercial device applications, most commonly for nonreciprocal electronics for signal processing [31, 32, 33, 34] and for magnetic field sensing [24].

2.1 Surface Acoustic Wave Excitation

Rayleigh Mode Shape in 128° YX Lithium Niobate

In a typical modern ADFMR study, SAWs are generated on a piezoelectric substrate and propagate through a ferromagnetic thin film under an applied magnetic bias field. SAW devices discussed in this thesis have been fabricated on a 128° YX-cut $LiNbO_3$ substrate. A known challenge with such piezoelectric substrates is their pyroelectric response. In sufficiently large wafers, thermal gradients within the material due to typical bake steps may lead to sizeable induced strain. These strains may result in fractures during processing, making large scale fabrication of piezoelectric wafers challenging. To mitigate this problem, "black"

lithium niobate wafers were used in all devices in this thesis. Under chemical reduction in nitrogen/hydrogen atmosphere, pure transparent lithium niobate becomes conductive at low frequencies, and the build-up of pyroelectric charge and strain due to thermal gradients is mitigated [35]. Such devices do not display any degraded piezoelectric performance at high frequencies, however, making them ideal for use in integrated surface acoustic wave applications.

While a range of cuts of $LiNbO_3$ are commercially available for surface acoustic wave applications, the 128° YX-cut was used here for a combination of reasons. This cut displays strong electromechanical coupling compared to other common crystal cuts [36], ensuring high conversion efficiency between electromagnetic and acoustic modes and vice versa. This is critical to ensure that power efficiency in the device is maintained for future applications to quantum systems. In addition, piezoelectric crystals are anisotropic, and their propagation velocity is known to be highly dependent on crystal direction. The 128° YX-cut offers a relatively high wave velocity in a non-leaky wave mode, increasing the minimum feature size required to deliver acoustic waves in the frequency band of interest.

To estimate the Rayleigh wave mode shape and strain amplitudes in 128° YX cut $LiNbO_3$, standard linear piezoelectric theory was used, following the theory of Rayleigh waves in anisotropic substrates [37, 38]. In a linear piezoelectric solid, the local substrate potential Φ and deformation components $u_{1,2,3}$ are coupled, and the equations of motion governing their behavior are given by:

$$\rho \frac{\partial^2 u_i}{\partial t^2} = \sum_j \sum_k \left\{ e_{kij} \frac{\partial^2 \Phi}{\partial x_j \partial x_k} + \sum_l c^E_{ijkl} \frac{\partial^2 u_k}{\partial x_k \partial x_l} \right\} \tag{2.1a}$$

$$\sum_i \sum_j \left\{ \epsilon^S_{ij} \frac{\partial^2 \Phi}{\partial x_i \partial x_j} - \sum_k e_{ijk} \frac{\partial^2 u_j}{\partial x_i \partial x_k} \right\} = 0 \tag{2.1b}$$

where e_{kij} is the substrate's piezoelectric tensor, c^E_{ijkl} is the substrate's stiffness tensor under constant electric field, and ϵ^S_{ij} is the substrate's dielectric tensor, which is typically anisotropic.

In a linear piezoelectric, the constitutive relations for stress and displacement field are given in Einstein summation notation by the tensor equations

$$T_{ij} = c^E_{ijkl} S_{kl} - e_{nij} E_n \tag{2.2a}$$

$$D_m = e_{mkl} S_{kl} + \epsilon^S_{mn} E_n \tag{2.2b}$$

where T_{ij} is the stress tensor, S_{kl} is the strain tensor, and E_n is the electric field vector.

Surface wave solutions to these equations of motion can be found when appropriate boundary conditions are applied. Here, we apply conditions corresponding to a infinitely thin, perfectly conducting metallized surface above a piezoelectric half-space. In this scenario, the

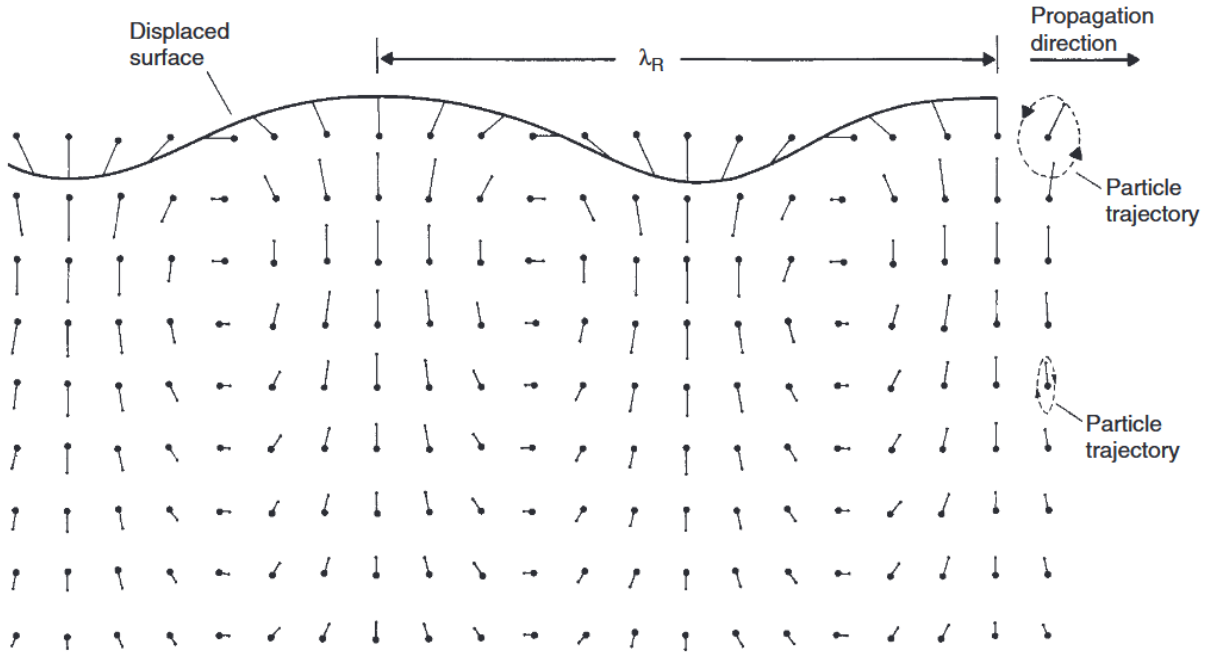

Figure 2.1: The displacements of the atomic lattice in a Rayleigh mode wave are periodic along the direction of propagation, and decay exponentially deeper into the substrate. In a piezoelectric substrate with the crystal symmetry of $LiNbO_3$, such waves consist of a weighted sum of four partial wave solutions, where the relative amplitudes are set by surface boundary conditions. Adapted from [37].

surface of the piezoelectric is stress-free, and the electric potential ϕ at the surface can be set to 0 without loss of generality. These conditions can be represented as

$$T_{3j} = 0 \ @ \ z = 0 \tag{2.3a}$$

$$\phi = 0 \ @ \ z = 0 \tag{2.3b}$$

Rayleigh waves in anisotropic substrates such as $LiNbO_3$ are a superposition of 4 partial wave solutions, such that displacement from equilibrium and electric potential take the form:

$$u_i = \sum_{r=1}^{4} \beta_i^{(r)} e^{-\alpha^{(r)} kz} e^{i(\omega t - kx)} \tag{2.4a}$$

$$\phi = \sum_{r=1}^{4} \beta_4^{(r)} e^{-\alpha^{(r)} kz} e^{i(\omega t - kx)} \tag{2.4b}$$

The horizontal wavenumber k can be related to the wave velocity and frequency by the linear dispersion relation $k = \frac{\omega}{v_s}$. As a result, solving for the values of v_s, $\alpha^{(r=1,2,3,4)}$, and

Table 2.1: Non-normalized Rayleigh partial wave parameters

α	β_1	β_2	β_3	β_4
1.95	-7.5e-11	8.0e-12	-2.4e-11	1
0.45+0.37j	-2.6e-11+6.6je-11	9.6e-12+4.4je-12	6.8e-11-6.3je-11	1
0.45-0.37j	2.6e-11+6.6je-11	9.6e-12-4.4je-12	6.8e-11+6.3je-11	1
0.31	3.6je-11	8.1e-10	2.1e-11	1

the normalized values of $\beta_i^{(r=1,2,3,4)}$ provides an exact set of surface wave solutions. Material coefficients were taken from the work of Warner [39], and were transformed under tensor transformation rules to the 128° Y-cut, X-propagating coordinate system. The resulting stiffness tensor c^E, piezoelectric tensor e, and dielectric tensor ϵ in the rotated reference frame are converted to Voigt notation for clarity and given below:

$$c^E = 10^{10}\begin{bmatrix} 20 & 7.0 & 5.8 & 1.3 & 0 & 0 \\ 7.0 & 19 & 9.1 & 0.97 & 0 & 0 \\ 5.8 & 9.1 & 22 & 0.85 & 0 & 0 \\ 1.3 & 0.97 & 0.85 & 7.6 & 0 & 0 \\ 0 & 0 & 0 & 0 & 5.7 & -0.51 \\ 0 & 0 & 0 & 0 & -0.51 & 7.8 \end{bmatrix} \tag{2.5a}$$

$$e = \begin{bmatrix} 0 & 0 & 0 & 0 & 4.45 & 0.31 \\ -1.85 & 4.43 & -1.54 & 0.08 & 0 & 0 \\ 1.70 & -2.68 & 2.32 & 0.62 & 0 & 0 \end{bmatrix} \tag{2.5b}$$

$$\epsilon = 10^{-10}\begin{bmatrix} 3.89 & 0 & 0 \\ 0 & 3.38 & -0.644 \\ 0 & -0.644 & 3.07 \end{bmatrix} \tag{2.5c}$$

Following calculation of the roots α, boundary conditions were applied, again creating a system of linear equations which can be solved to find values of β. This process is repeated with successive guesses of v_s to minimize the determinant of this 2nd linear system, eventually yielding a wave velocity of 3887.7 m/s,. The corresponding values for α and β are given in Table 2.1.

Interdigital Transducer Design and Fabrication

The design and fabrication of all interdigitated transducers used in this thesis were performed by collaborators from Institute FEMTO-ST institute and frec—n—sys, Dr. Samuel Margueron and Professor Ausrine Bartasyte. This section is intended to provide additional reference data and context for the results of studies detailed later in the document.

The standard structure for a study of acoustically-driven ferromagnetic resonance (ADFMR) utilizes a surface acoustic wave delay-line structure, as depicted in Figure 2.2. The delay-line

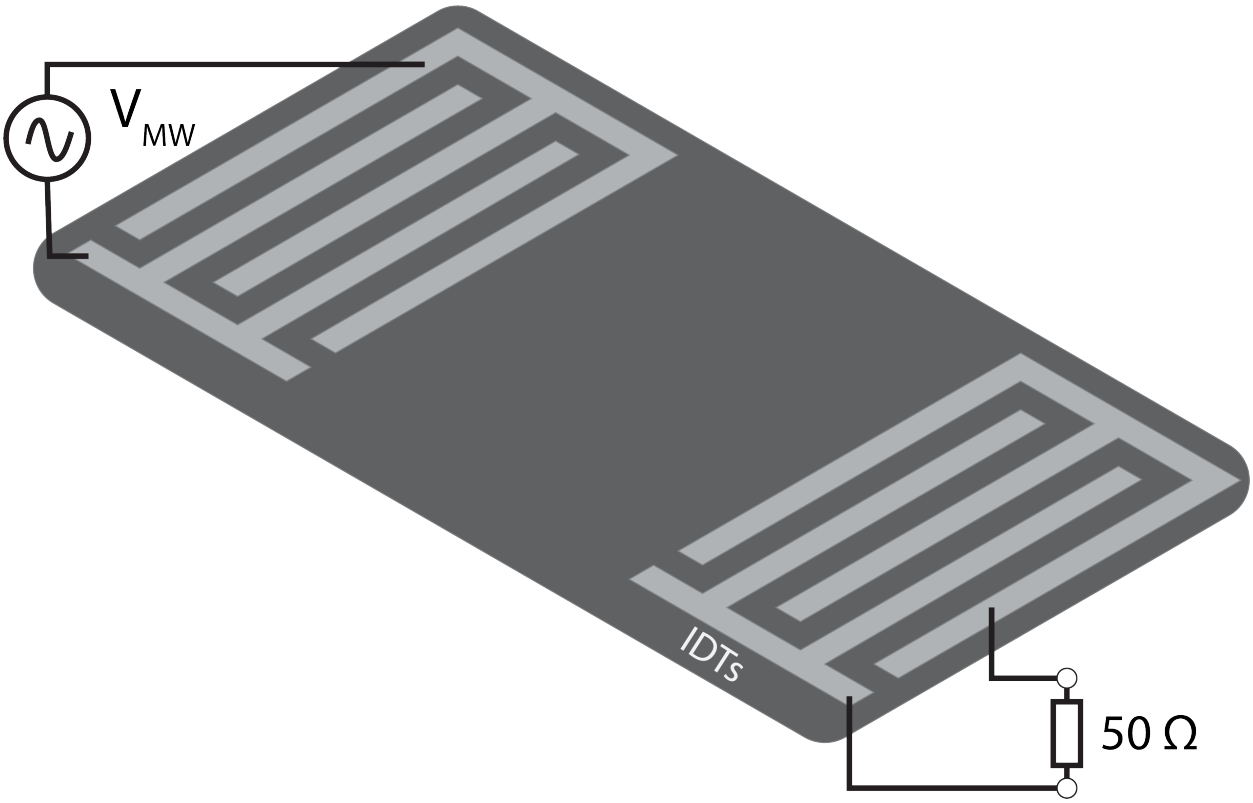

Figure 2.2: Structure of an Interdigitated Transducer (IDT) pair in a delay-line configuration. IDTs are designed with a nominal input impedance of 50 Ω to minimize reflection losses. Finger width is approximately 370 nm, leading to an effective acoustic wavelength of 1.48 μm. For the Rayleigh wave mode of interest, this leads to a center frequency of 2.6 GHz. IDT fingers are 80 nm thick Al, patterned via lift-off.

structure provides sufficient space for a magnetic film to be deposited between the transducers, however, the spacing adds additional loss to the structure. IDTs used throughout this thesis are bidirectional, resulting in a minimal 6 dB insertion loss due to the fact that both transducers emit waves in the reverse direction as well. Should it be necessary to reduce this loss, unidirectional IDT designs exist [40]. A far greater contribution to insertion loss in the ADFMR literature, however, is the common usage of IDTs with a lower fundamental frequency driven at high harmonics to excite high frequency acoustics [29, 30, 41, 42]. This approach allows for ease of fabrication, as the IDT feature size is much larger, but comes with the trade-off of high insertion loss, as well as the risk that electromagnetic radiation from the IDTs acts as a confounding excitation of magnetic dynamics inside the film.

Four different IDTs were designed and fabricated by Dr. Samuel Margueron and Professor Ausrine Bartasyte, each with slightly different design parameters, but approximately the

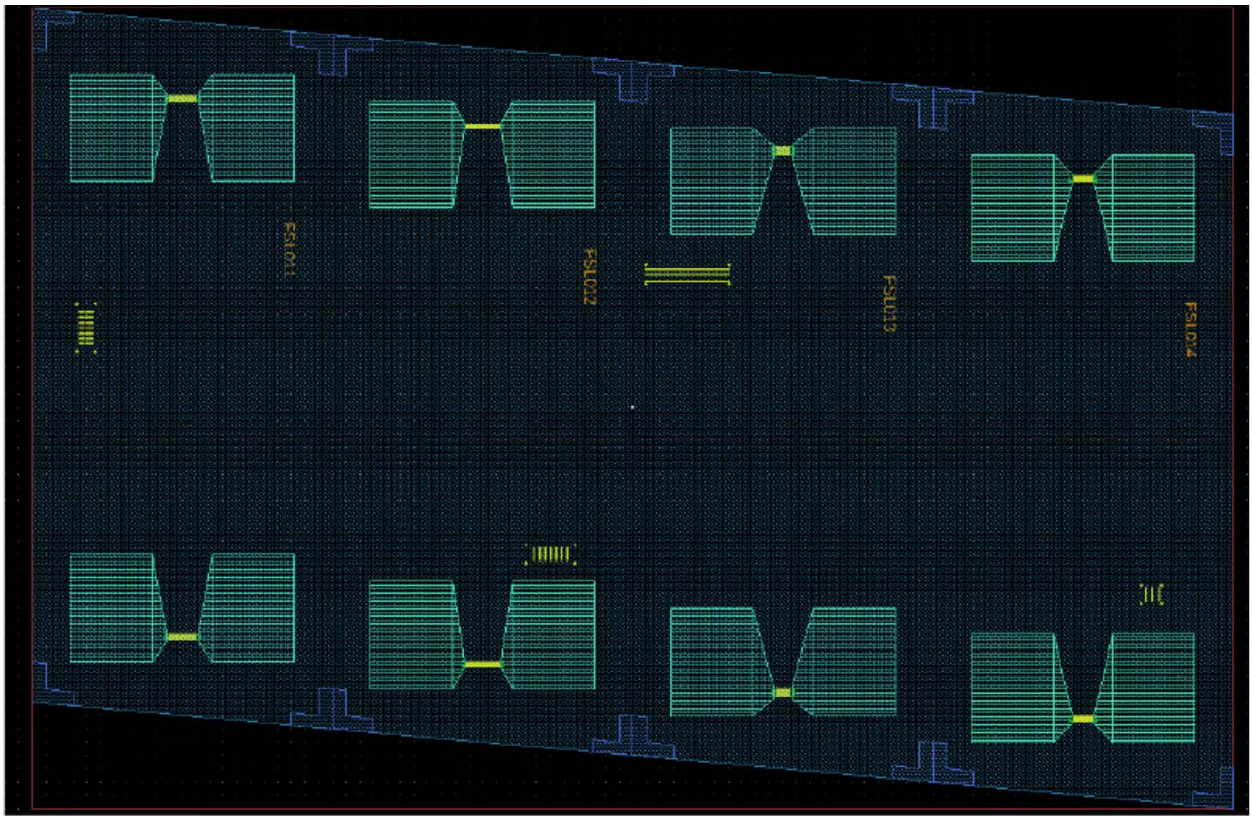

Figure 2.3: Layout of the fabricated interdigitated transducers. Each transducer has slightly different design parameters. In addition, due to their close proximity, weak couplings between the IDTs are present, which are in part mitigated by time-gating techniques.

same center frequency and insertion loss. IDTs were fabricated using 80 nm thick evaporated aluminum, patterned via lift-off. The layout of the IDT structure is provided in Figure 2.3; each IDT is labeled (from left to right) FSL01(1-4), and each has a separation distance of 2 mm. The structure displayed in the layout is repeated many times over a 4-inch wafer of 128° YX-cut $LiNbO_3$. Due to the dense packing of transducers, spurious acoustic reflections off of nearby transducers are present, as are weak couplings between transducers. Time-gating (discussed later), addresses much of this error, but some deviation from nominal performance remains. Table 2.2 provides details of the individual IDT design parameters, and Figure 2.5 provides a comparison of nominal theoretically predicted performance and measured transmission with use of 50 Ω impedance matched RF probes.

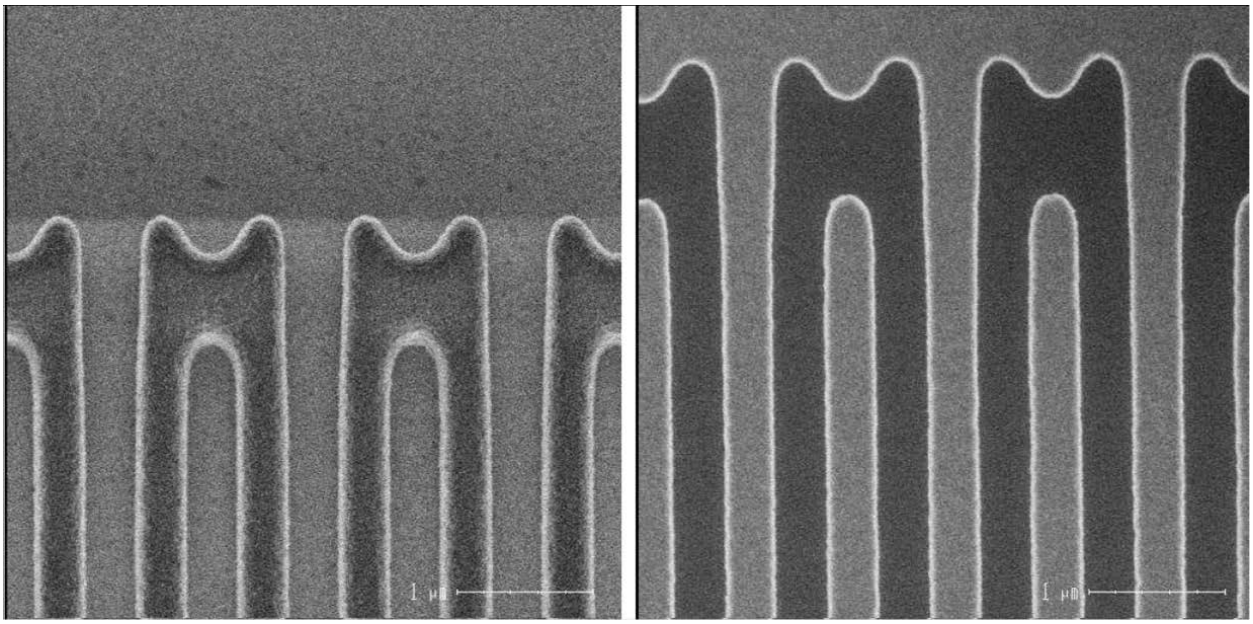

Figure 2.4: Electron microscope image of the fabricated fingers. Finger width and spacing are both approximately 370 nm.

Table 2.2: Design Parameters of IDT in use

Device	FSL011	FSL012	FSL013	FSL014
Number of Electrodes per IDT	30	20	40	30
Acoustic opening (μm)	100	120	50	70

2.2 Acoustically Driven Ferromagnetic Resonance Theory

Theoretical models for ADFMR in thin films are developed beginning from the contributions to magnetic free energy density. With magnetization vector $\vec{m} = \frac{\vec{M}}{M_s}$ normalized to saturation magnetization, a common model for this free energy density G is given by [8]

$$G = \mu_0 \vec{H_{ext}} \cdot \vec{m} + B_d m_z^2 + B_u (\vec{m} \cdot \vec{u})^2 - \mu_0 \vec{H}_{ex} \cdot \vec{m} \tag{2.6}$$

This model incorporates energy contributions from (in order) the Zeeman effect with an externally applied bias field $\vec{H_{ext}}$, the shape anisotropy coefficient B_d, the uniaxial in-plane anisotropy coefficient B_u, and exchange field, where $\mu_0 \vec{H}_{ex} = D_s \Delta \vec{m}$, and D_s is the exchange stiffness. The in-plane easy axis is given by the vector $\vec{u}$. At the acoustic wavelengths of interest, the exchange bias Laplacian is typically small compared to other energy contributions, and is neglected.

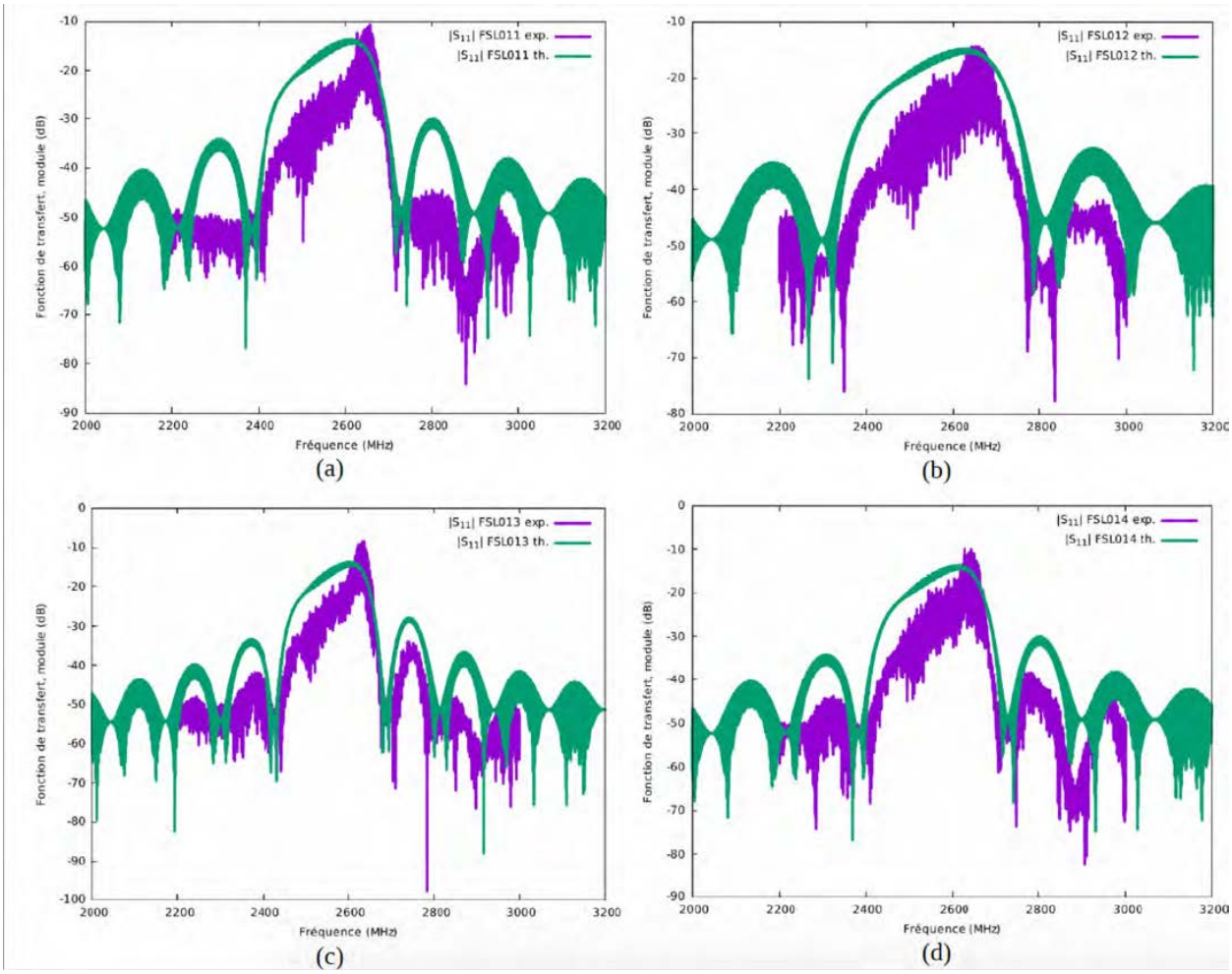

Figure 2.5: Transmission parameters of all four IDT designs. While slight variations in bandwidth and shape are present, all IDTs display a center frequency of around 2.6 GHz, with an insertion loss of approximately 14 dB. Primary contributions to this loss are the bidirectional transmission of acoustic waves and propagation losses across the 2 mm long delay-line.

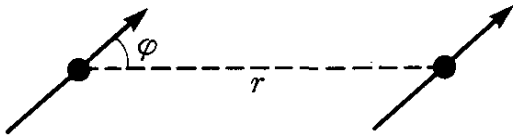

Figure 2.6: Pair energies in spins are dependent on their variable bond lengths and relative orientations. By expanding this scalar energy in a multipolar expansion and summing first order terms over a lattice, the expression for total magnetoelastic energy is derived. Adapted from [43].

In addition to these terms, a magnetoelastic free energy density G_{me} is present. This magnetoelastic energy is calculated by expressing pair energy of adjacent spins as a multipolar expansion in spatial distance and relative spin orientation, truncating the series to first order, and summing over a lattice [43]. In crystalline films, this free energy density is parameterized by two material parameters b_1 and b_2 and given by [43]

$$G_{me} = b_1 \sum_{i=1}^{3} \epsilon_{ii} m_i^2 + b_2 \sum_{i \neq j} \epsilon_{ij} m_i m_j \tag{2.7}$$

However, in polycrystalline films, such as the ones used in this thesis, $b_1 = b_2$, yielding the simpler expression

$$G_{me} = b \sum_{i \neq j} \epsilon_{ij} m_i m_j \tag{2.8}$$

Under a sinusoidal acoustic excitation, an effective magnetoelastic "tickle" field is produced as a consequence of this coupling term, given by $\mu_0 \vec{H}_{me} = -\nabla_{\vec{m}} G_{me}$. The general expression for this tickle field is given in [8], but for the special case of an in-plane magnetized film, the in-plane and out-of-plane components perpendicular to DC magnetization are given by

$$\mu_0 h_{IP} = 2b \sin\theta \cos\theta [\epsilon_{xx} - \epsilon_{yy}] - 2b\epsilon_{xy} \cos(2\theta) \tag{2.9a}$$

$$\mu_0 h_{OOP} = 2b(\epsilon_{xz} \cos\theta + \epsilon_{yz} \sin\theta) \tag{2.9b}$$

where $\hat{x}$ is the direction of acoustic propagation and $\hat{z}$ is perpendicular to the surface plane of the magnetic film. θ is the angle between the magnetization and acoustic propagation direction. As shown in Figure 2.7, magnetoelastic tickle fields display a distinct 4-lobed pattern that acts as a qualitative signature of this kind of drive.

Under an effective excitation field, the magnetic dynamics of a ferromagnet are phenomenologically described by the damping parameter α in the well-known Landau-Lifshitz-Gilbert (LLG) equation. [44]

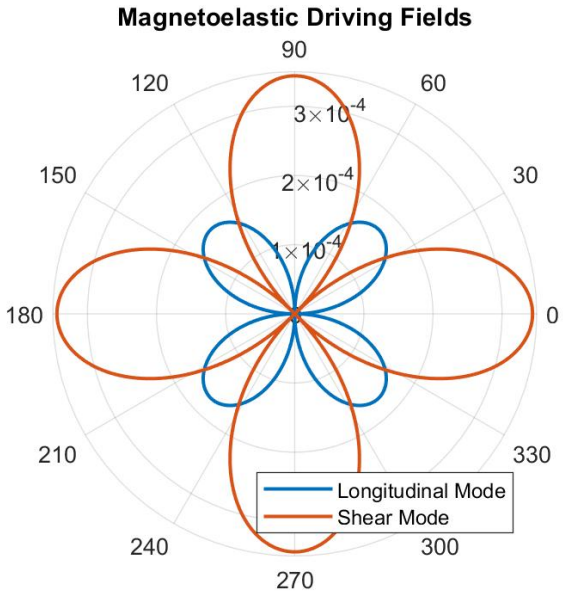

Figure 2.7: Optimal applied magnetization orientations for magnetoelastic coupling are dependent on the type of strain applied to a ferromagnet. Neglecting magnetic anisotropy effects, the magnetoelastic fields are maximized when magnetization is at a 45° angle to the acoustic propagation axis. Shear wave coupling is maximized when magnetization is parallel or perpendicular to acoustic propagation.

$$\frac{d\vec{M}}{dt} = -\gamma\vec{M} \times \vec{H}_{eff} - \frac{\alpha}{M}\vec{M} \times \frac{d\vec{M}}{dt} \tag{2.10}$$

This equation provides a model for the effective susceptibility tensor $\overline{\overline{\chi}}$, a material dependent property. This susceptibility displays a strong frequency dependence, with a resonant maximum typically in the GHz regime, though this can be shifted via the Zeeman effect with sufficiently strong applied magnetic field. The power absorption in a ferromagnetic film is given by

$$P_{abs} = \frac{\mu_0\omega}{2}\int_V Im[\vec{h}^*_{AC}\overline{\overline{\chi}}\vec{h}_{AC}] \tag{2.11}$$

2.3 Experimental Methods

In order to characterize acoustic absorption, diced chips containing IDTs were wirebonded to a PCB, as shown in Figure 2.8. SMA connectors were linked to two devices on the chip, one with a Ni magnetic layer and one without to ensure that lift-off processing of the Ni

Figure 2.8: Devices were wirebonded to a PCB with 6 SMA connectors soldered to a 50 Ω waveguide in a hexagonal layout. Single wirebonds were found to have a parasitic inductance which prevented efficient coupling from the PCB waveguide to the transducers, so two wirebonds were used per pad, for a total of eight bonds per IDT pair. As the PCB surface was coated in a solder mask, a diamond-tipped scribe was used to scrape off coating layers to expose the underlying copper layer for bonding. The copper layer was scraped within 15-20 minutes of bonding, as surface oxidation of the copper made Al bonding challenging after longer periods.

pad did not impact the IDT performance. Due to the presence of inductive wirebonds, the input impedance of the IDTs was slightly shifted, manifesting as a 3 dB reflection loss. As a result, nominal insertion loss of the IDTs in use in this system totalled approximately 17 dB at center frequency. The PCB was then mounted onto a rotational stage, depicted in Figure 2.9.

2.4 Time Gating Methodology

As detailed in prior work on pulsed surface acoustic wave driven ADFMR, accurate measurements of transmitted acoustic power requires a temporal isolation of the primary acoustic wave pulse from surrounding signals [45, 8, 29]. Common causes of time-separated transmission are an electromagnetic pulse produced by the IDTs which travels at the speed of light, triple-transit signals caused by partial reflections of the acoustic wave from the receiving IDT, and in the case of our device, spurious reflections from nearby IDTs pairs.

Following microfabrication, the IDTs were wirebonded to 50 Ω coplanar waveguides on a custom built PCB. The total transmission loss in the PCB alone was approximately 3 dB, due to impedance mismatch caused by the self-inductance of the wirebonds. To quantify the

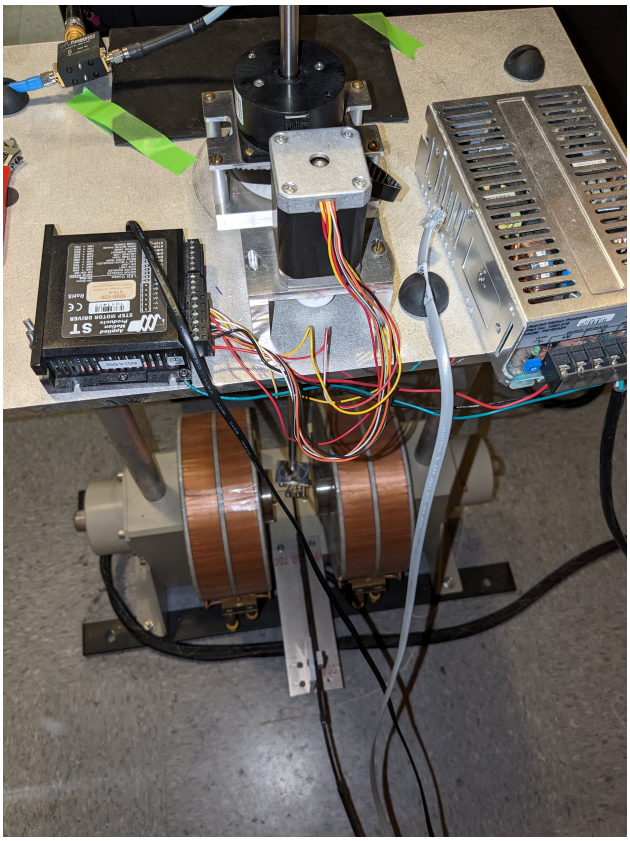

Figure 2.9: Experimental characterization setup for acoustically driven ferromagnetic resonance. A rotational dipstick with PCB attached mounted between the poles of an electromagnet.

total transmission loss of the combined PCB-IDT system, 2-port S-parameters for control IDT pairs with no Ni layer between them were measured using a vector network analyzer. The acoustic transmission was time-gated, isolating the signal from spurious signals due to electromagnetic transmission and SAW triple-transit signals, similar to the methodology detailed in prior SAW-driven ADFMR measurements. [42] The transmitted signal consisted of an electromagnetic pulse, the primary acoustic pulse, and a number of smaller pulses related to triple-transit and spurious reflections off of adjacent IDTs. To guarantee that these spurious reflections did not overlap with the primary pulse in the time domain, potentially compromising the time-gating process, IDT transmission was measured with adjacent IDTs coated in photoresist. Transmitted power was found to be unchanged relative to measurements without the photoresist, indicating that spurious reflections due to nearby transducers were successfully filtered out by the time-gating process.

Initially, 2-port S-parameters of the FSL011 IDT were measured using an HP 8722D

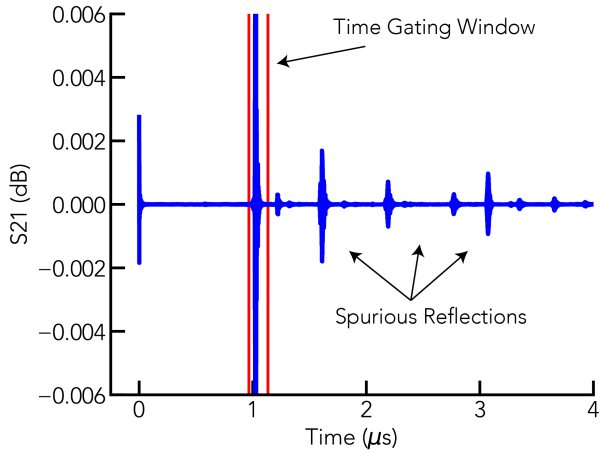

Figure 2.10: Plot of S_{21} following an inverse Fourier transform. The initial pulse at 0μs is due to electromagnetic waves emitted by the transmitter IDT, while the primary acoustic pulse and time-gating window are found at 1μs. Subsequent pulses are attributed to a combination of triple-transit signals and reflections from nearby IDTs on chip.

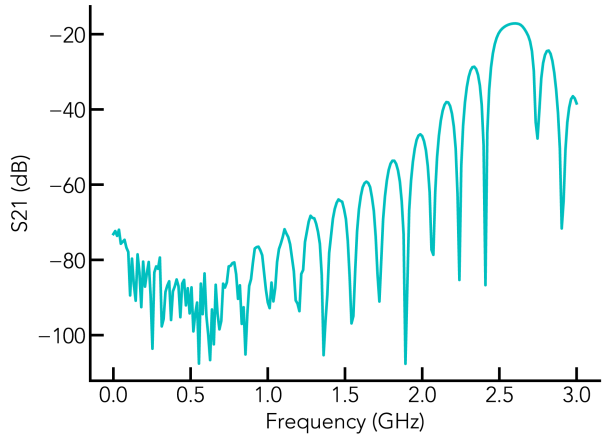

Figure 2.11: Plot of S_{21} following time gating around the primary acoustic pulse in Figure 2.10. The acoustic transmission is seen to be centered around 2.6 GHz, with an insertion loss of approximately 17 dB.

vector network analyzer from 50 MHz to 3GHz over 16000 points. Data was zero-padded at frequencies below 50 MHz to produce accurate Fourier transforms; this is justified by the fact that power transmission at DC and low frequencies is insignificant for these devices. An inverse Fourier transform was applied to this data to obtain the time-domain representation of the signal, shown in Figure 2.10. Pulses corresponding to the electromagnetic wave, primary acoustic pulse, and spurious reflections can be seen. A time window was chosen to contain the primary acoustic pulse, and was Fourier transformed back into frequency domain, as shown in Figure 2.11. Following characterization and time-gating, the control IDT pairs without a Ni pad were found to have an insertion loss of approximately 17 dB. 3 dB of this was found to be reflected from the PCB back into the network analyzer due to impedance mismatch from wirebond parasitic inductance. With the addition of the Ni magnetic pad, additional losses, even at high magnetic fields, resulted in a total insertion loss of 25 dB.

2.5 ADFMR Data Collection Methods

To characterize ADFMR power absorption, 20nm thick Ni thin films were deposited between FSL014 IDT pairs by e-beam evaporation, and patterned by lift-off. The resulting Ni pad was of width 150 μm and length in the SAW propagation direction of 600 μm. A diagram of the resulting device is provided in Figure 2.12. PCBs with a deposited Ni film were placed on a rotational stage between coils of an electromagnet, and SAW transmission was characterized under a sweep of DC magnetic bias field and direction.

To reduce measurement times, the vector network analyzer was replaced by a pulsed RF function generator at the input port, and the output port was fed into a spectrum analyzer. The function generator was configured to output 2.6 GHz pulses with a pulse width of 700 ns via an Agilent E8257D function generator, and the Keysight CXA 9000A spectrum analyzer measurement was synchronized to these pulses, by manually adding a propagation time delay based on the time-gating measurements from the network analyzer. This effectively implements an equivalent time-gating process in the test hardware, but without requiring data collection over a wide frequency band. The applied DC magnetic field was swept through 360° and through field magnitudes of 0 to 300 G at varying microwave input powers. To ensure that hysteretic effects within the magnet did not impact measurement, at each angle, 500 G fields were applied prior to the field sweep to fully saturate the magnetic film, a procedure repeated for all radial magnetic field sweeps throughout this thesis.

2.6 Resonant Magnetoelastic Power Absorption

Power absorption over a radial magnetic field sweep is provided in Figure 2.13. The 4-lobed pattern characteristic of ADFMR seen in prior studies [29] is observed, consistent with the expected qualitative angular dependence of a longitudinal strain excitation. Discontinuous outlier data is present at certain angles; this is due to occasional power supply errors leading

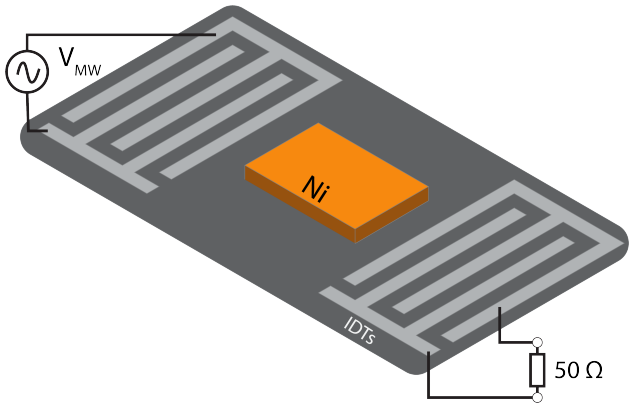

Figure 2.12: Structure of fabricated ADFMR device. Transmitter and receiver IDTs are wirebonded to the PCB waveguide by Al wire. The acoustic opening of the IDTs along the $LiNbO_3$ is 100μm. The Ni pad is 600 μm long, 150 μm wide, and 20 nm thick.

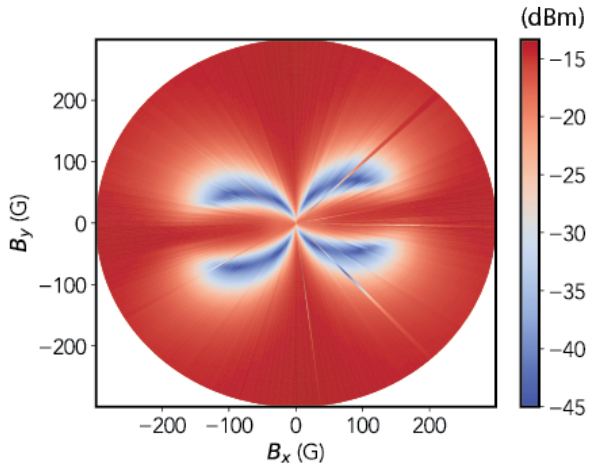

Figure 2.13: Angular field sweep of 20 nm thick Ni film at an applied input power of +10 dBm. The color bar indicates the transmitted power in dBm, where the X direction represents the propagation direction of the SAW. A 4-lobed absorption pattern is clearly observed, characteristic of ADFMR driven by primarily longitudinal strain.

to current spikes in the electromagnet. While ideal magnetoelastic theory predicts that the lobe maxima should be seen at 45° angles, slight deviation is present; this is attributed to magnetic anisotropy fields.

To illustrate key details of the SAW absorption, two line-cuts of the absorption data are plotted: along curves of peak absorption, and along field sweeps at angles of maximum

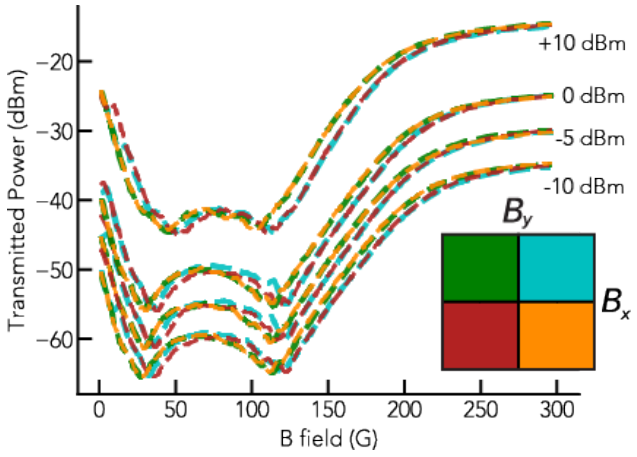

Figure 2.14: Curves of peak absorption are plotted for each of the 4 lobes (color-coded) for various input powers. Two points of maximum absorption are clearly visible within each lobe. At +10 dBm input power, a qualitative shift in power absorption is seen, indicating that some component in the system is beginning to behave nonlinearly. The absorption curves deviate from each other slightly for lobes rotated by 90°; this is attributed primarily to magnetic anisotropy.

absorption. Curves of peak absorption for each absorption lobe are plotted in Figure 2.14 at various input powers. The angle of maximum power absorption at each given field value is determined, and the value of maximum absorption is plotted as a function of field value. The trajectories being followed in Figure 2.14 are overlaid over the field-swept absorption data in Figure 2.15. Two absorption peaks within each lobe can be clearly seen, in contrast to prior measurements of ADFMR absorption in $LiNbO_3$/Ni stacks.[30] The slight variation in resonance peak depth and position at +10 dBm compared to the lower applied powers is attributed to an onset of nonlinear behavior in the system.

For the field sweeps at angles of maximum absorption, the two angles at which absorption peaks occur within each lobe are determined, and power absorption is plotted vs. applied field for these angles in Figure 2.16. While two separate maxima are observed over the full range of applied DC magnetic fields and angles, the absorption line-shapes remain consistent with those previously reported, and are qualitatively similar to those of traditional FMR measurements.

2.7 Strain Amplitude Estimation

Following evaluation of the partial wave solutions, and the relative amplitudes of the partial waves, the amplitudes were normalized based on the experimentally transmitted power. This was performed by evaluating the complex piezoelectric Poynting vector and integrating

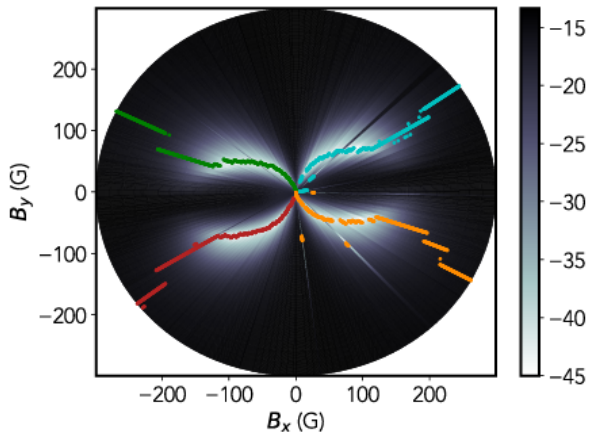

Figure 2.15: The trajectory of the linecut in Figure 2.14 is overlaid over the field sweep data for the +10 dBm input power level. The variability of the optimal resonance angle with applied field indicates the presence of magnetic anisotropy fields of the same order as the applied fields within the film. The data plotting color is altered to make the colored trajectory paths more visible.

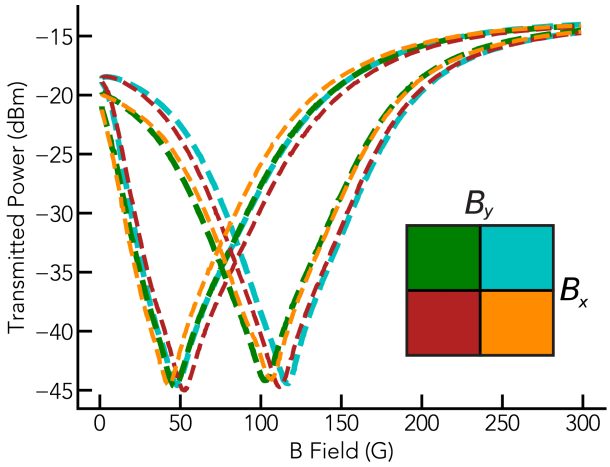

Figure 2.16: Field sweeps along angles of maximum absorption are plotted for each lobe (color-coded) here at an input power of +10 dBm. The fields of maximum absorption are $\approx$ 50 G and $\approx$ 110 G for each lobe, and the lineshapes remain approximately Lorentzian, consistent with prior studies on ADFMR.

Table 2.3: Estimated strain components for acoustic waves at varying applied RF power.

Input Power (dBm)	ϵ_{xx} (um/um)	ϵ_{xy} (um/um)	ϵ_{xz} (um/um)
+10	2e-4	1e-5	1e-6
0	6e-5	4e-6	3e-7
-5	3e-5	2e-6	2e-7
-10	2e-5	1e-6	1e-7

it over the plane perpendicular to the acoustic wavevector. The Poynting vector can be represented as

$$\vec{P} = -\frac{\dot{u_i^*} T_{ij}}{2} + \frac{\phi(i\omega D^*)}{2} \tag{2.12}$$

The SAW strain amplitude within the Ni film was estimated following the methodology of Warner et.al.[39] In order to normalize the wave amplitudes to the experimentally delivered power, two critical assumptions are made. Firstly, the SAW amplitude within the ferromagnet is approximated to be equal to the strain at the surface of an infinitesimal conductive layer above $LiNbO_3$. Secondly, losses were assumed to be symmetric across the device, meaning that the power loss in dB from transmitter IDT to magnetic film was 12.5 dB, half of the total insertion loss. Furthermore, the acoustic excitation was assumed to be roughly uniform across the IDT opening width of 100 μm. As a consequence of these approximations, the calculated acoustic strain is treated as only a rough approximation of the actual strain within the Ni layer. The resulting approximations of longitudinal and shear strain components are provided in Table 2.3.

Chapter 3

NV Experimental Setup Construction

Following initial characterization of efficient SAW transducers and magnetic absorption, the next step was to develop a system capable of optical characterization of NV centers in close proximity to a magnetic film undergoing ADFMR. This chapter overviews the equipment, design, and construction of such a setup, and discusses the constraints and design reasoning. Owing to time and budget limitations, occasional compromises in performance were made at various points in the construction process; areas where room for improvement is available are discussed as well.

3.1 Equipment List

In order to perform a standard continuous wave NV center optically detected magnetic resonance (ODMR) measurement, a range of capabilities need to be provided. NV centers must be optically excited, typically by a focused laser. Examples of NV-ODMR characterization setups in the literature are ubiquitous, and simple benchtop setups capable of simple quantum readout can be constructed with relative ease [46]. Depending on the complexity of the intended experiment, diamond geometry, and required photon collection efficiency, such setups can rapidly increase in complexity. More advanced characterization setups may include confocal elements, multiple excitation wavelengths, and complex laser and microwave pulse schemes [47]. In the commonly used epifluorescence configuration for illumination and fluorescence collection, the NV fluorescence is collected by the same objective lens which focuses the excitation light; typically with a high numerical aperture [48]. Atypical to standard practice, the fluorescence intensity in the setup constructed here is characterized by pulsing the laser via a pulse generator and acousto-optic modulator (AOM) and measuring the intensity at the modulation frequency via lock-in.

In typical ODMR measurement, high power microwaves are used to drive the NV center via an antenna or stripline, often making use of some form of RF power amplifier. While such an amplifier was originally intended to be used, early measurements showed that due to the power efficiency of magnetoelastic excitation, the required input power was within

Table 3.1: NV ODMR Setup Key Components

Name	Vendor	Model Number
2-axis Vector Electromagnet	EastChanging	EM3-2
532nm Green Laser	Coherent	OBIS 532
Acousto-optic modulator	Gooch & Housego	3080-125
Signal Generator	Stanford Research Systems	SG386 Option 03
Lock-in Amplifier	Zurich Instruments	MFLI MF-MD Option
Pulse Generator	SpinCore	PulseBlaster ESR-PRO-300
3-Axis Motorized Stage	Newport	CONEX-MFACC
Avalanche Photodiode	Thorlabs	APD430A2
Objective Lens	Nikon	TU Plan Fluor 50x/0.8 NA

the output power range of our original signal generator, which we used to excite 2.6 GHz microwaves. Due to the slow speed of the measurement, and the variation in transmitted power over frequency, ODMR was characterized at a single frequency and magnetic field was swept radially, in contrast to the common approach where frequency and field are both swept.

Many components were used within the constructed setup; key items are provided in Table 3.1.

3.2 PCB Design

Due to limited space between the 2-axis electromagnet poles, a new PCB was designed and fabricated for characterization in this setup. 2 SMA connectors were linked to 50 Ω waveguides, which were again wirebonded to the substrate. Aluminum wire was used for bonding between immersion gold pads on the PCB and the aluminum IDT contact pads. Three screw holes were also included in the PCB to hold it in fixed position. Nonmagnetic fasteners were used for mounting to minimize movement and strain due to changing magnetic bias fields. A diagram of the PCB is provided in Figure 3.1. SMA connectors were reflow soldered to the PCB, and an example of the final wirebonded PCB-device structure is provided in Figure 3.2.

3.3 Mounting and Mechanical Noise Mitigation

The PCB was mounted on a custom machined connector, which was in turn screw mounted onto the 3-axis CONEX MFACC motorized stage. Initially, a 3D printed ABS connector was used, but was found to vibrate unacceptably over the course of a multi-hour fluorescence measurement, resulting in continuous degradation of the fluorescence signal due to misalignment with the input laser beam. With assistance of Dorotea Macri, the final aluminum machined part was produced; shown in Figure 3.3.

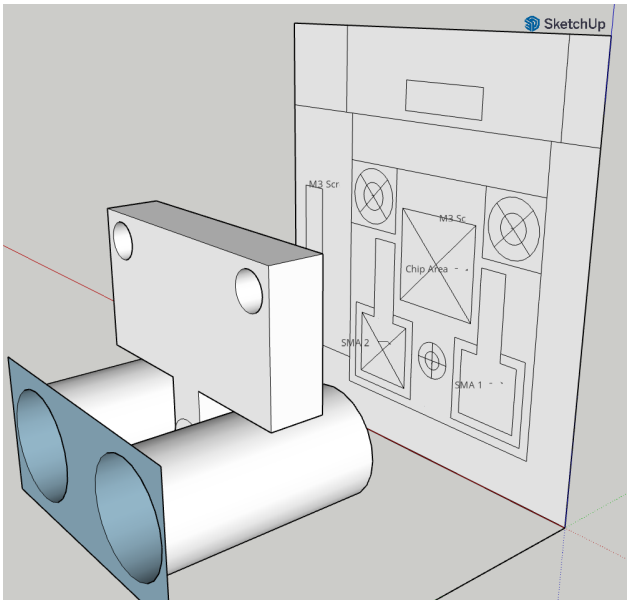

Figure 3.1: CAD Model of PCB Layout, along with mounting plate structure and approximation of SMA connectors. A 1 cm square was budgeted for the 8mm x 9mm parallelogram chip. Magnetic field Hall sensors were intended to be mounted around the PCB, but non-uniformity of the electromagnet field made this impractical.

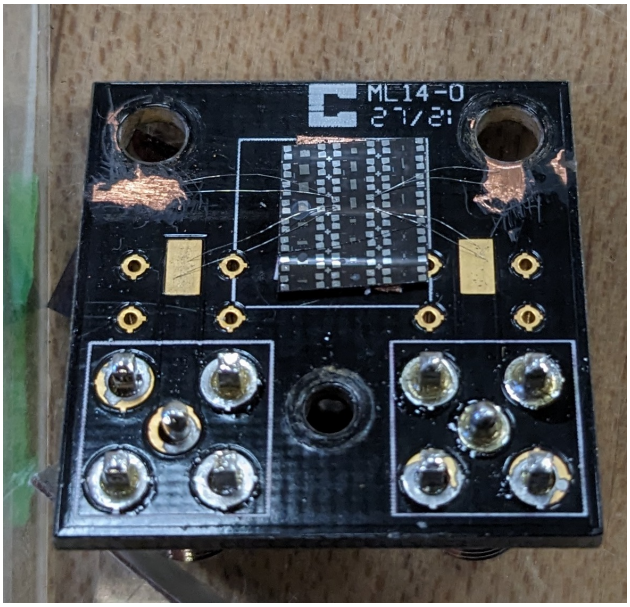

Figure 3.2: Soldered and wirebonded PCB; later used for characterization in Chapter 4.

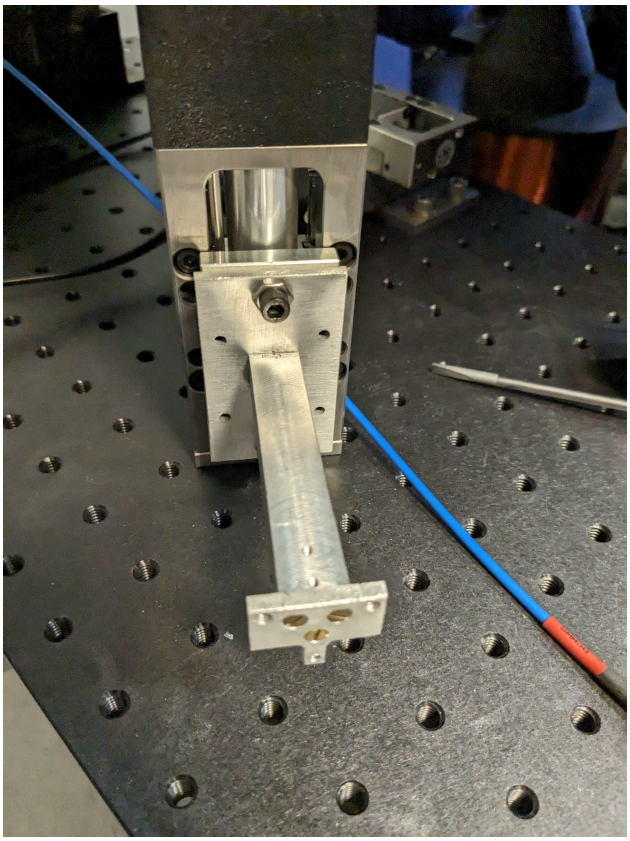

Figure 3.3: Custom machined Al mount attached to the CONEX MFACC stage. Consists of three screw-attached parts, with a nearly square cantilever cross-section to minimize bending. Brass screws were used instead of tool steel for components between the electromagnet poles to avoid magnetic deflections.

Initially, even with a rigid aluminum mount, mechanical drift reached unacceptable levels over the course of a single scan. Active mechanical correction through the motorized 3-axis stage was used to maintain focus on a chosen point. As the measurement occurred at a single pixel, and no parallel widefield imaging of fiducial features was present, measurements were limited to locations that were local maxima of NV fluorescence. While piezoelectric stages providing single nanometer precision are commonly used for NV characterization, these were unavailable at the time of construction. As a consequence, the positioning accuracy over the course of a measurement was limited to the minimum repeatable step size of the CONEX MFACC stages, namely 800 nm. In the event that measured fluorescence intensity dropped below a particular threshold, position would be scanned within a 5 μm range in all dimensions to refocus the laser on the local maximum of NV fluorescence. As a consequence of the 800 nm positioning precision, the setup was chosen to be non-confocal, as the improved optical

resolution in a confocal imaging system would be useless without a comparably precise positioning system, and would reduce the total fluorescence collection efficiency.

After initial measurements, it was found that the dominant source of drift in the system was due to the length of the optical posts holding the objective lens. To reduce this drift further, the objective lens was placed on a raised platform, and its optical post diameter was increased from 0.5 inches to 1 inch. Unfortunately, due to the working distance of this lens, part of its steel mounting frame was positioned within the poles of the electromagnet. While it was mounted as tightly as practically achievable, small angular deviations in its position occur, particularly at high field, manifesting as a maximum 10 percent degradation in total fluorescence intensity. As ODMR contrast is normalized to total fluorescence intensity, this does not impact ODMR contrast to first order, but eventually would limit the maximum magnetic field that can be applied to the system. As the fields used in experiments here did not exceed 250 G, this was not a critical factor, but would be a point of future improvement.

3.4 Magnetic Field Calibration

Over the course of measurement, it was found that the magnetic field between poles of the electromagnet varied significantly between the center, where the device was positioned, and the positions where Hall effect probes were mounted to measure field. Due to the size and geometry of the PCB, it was not possible to place Hall probes sufficiently close to the device to get an accurate measure of the field without significant redesign of the PCB and custom mount. Instead, prior to a measurement, the intended magnetic field sweep was run with the Hall probes mounted in place of the PCB, and the measured data was used as a calibration reference for converting electromagnet pole currents to magnetic field. Referenced to the coordinate system defined in Figure 4.1, the calibration data was collected in the $\hat{y}$ and $-\hat{z}$ directions, and is plotted in Figure 3.4. In addition to compensating for nonuniformity in the magnetic field, this approach also removed the impact of a manufacturing defect in the electromagnet where poles were slightly misaligned, leading to slightly rotated fields. As a downside, the resulting grid of data points is characterized using a regular grid of currents, but the resulting grid of field points is slightly irregular.

3.5 Final Setup Structure

The final structure used a double-pass acousto-optic modulation setup, and a block diagram of all optical and electrical signals is provided in Figure 3.5. The double-pass system, detailed in [49], is a modulation scheme that decouples the focal position of the laser beam from the diffraction angle of the modulator. This has a number of advantages, as this diffraction angle depends on parameters such as modulation frequency, meaning that a single-pass system would require position correction outside a certain modulation bandwidth. A double-pass system is not strictly critical for this system, as modulation frequency was not shifted,

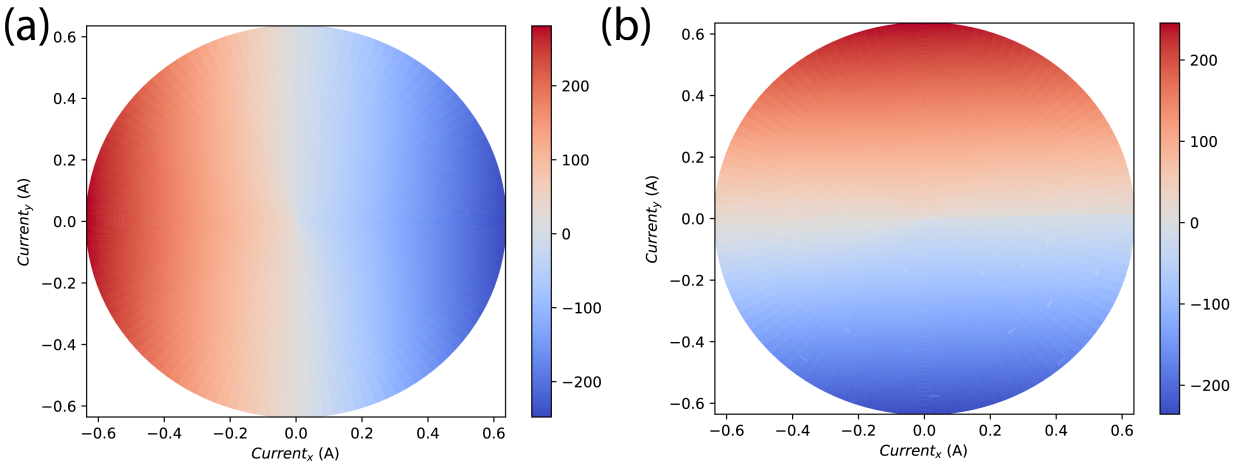

Figure 3.4: (a) Measured magnetic field in Gauss under radially stepped currents measured parallel to the direction of propagation of the acoustic wave in all measurements. (b) Measured magnetic field in Gauss under radially stepped currents measured perpendicular to the direction of propagation of the acoustic wave in all measurements.

but was convenient for construction, as the laser beam was initially aligned with mounting screw holes on the table for convenience, and the double-pass scheme also maintains this alignment. Regardless, the system is capable of modulation across the full bandwidth of the AOM without requiring realignment. A photograph of the final setup is provided in Figure 3.6, as is a display of the system in action in Figure 3.7.

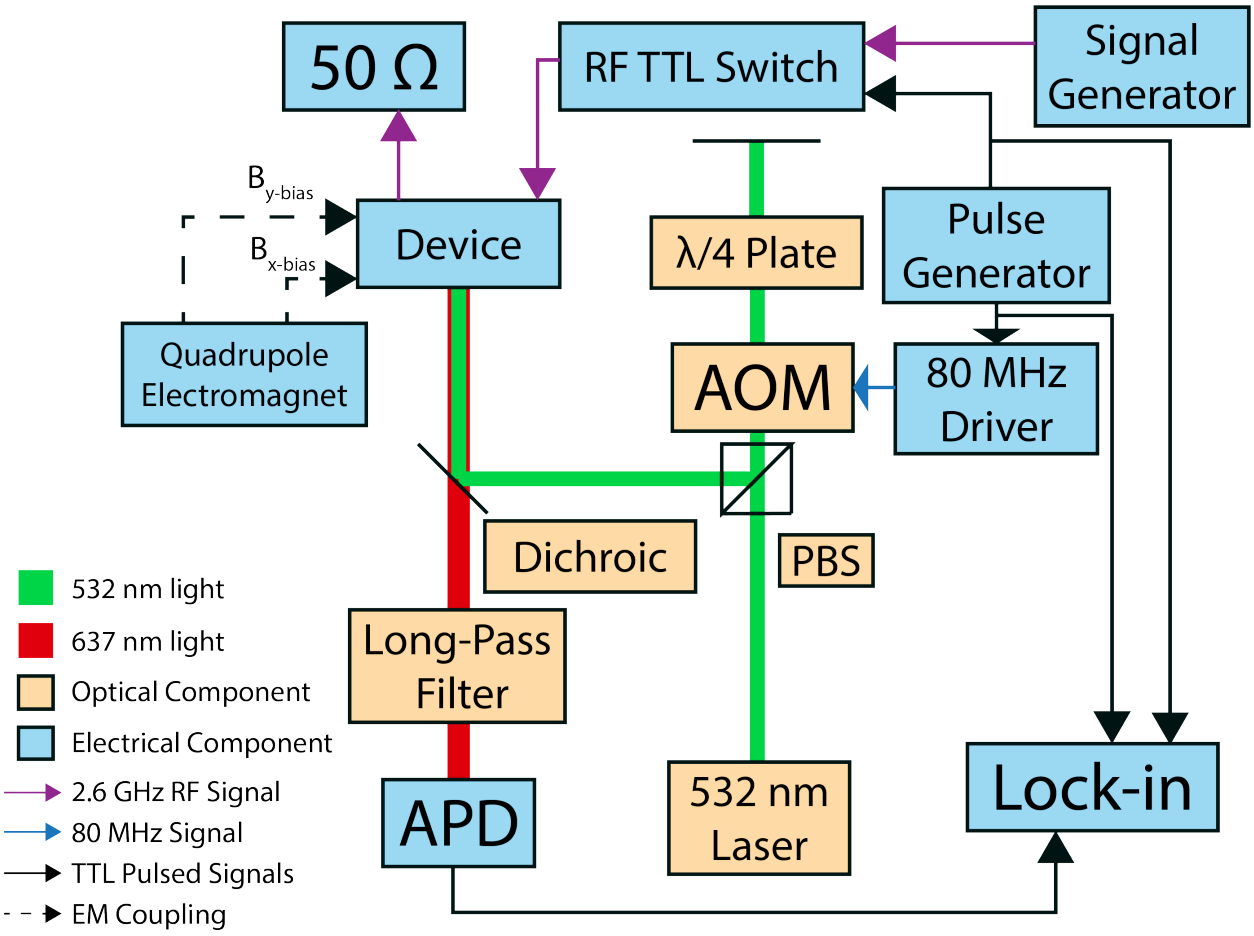

Figure 3.5: Block diagram of all critical elements in the final NV ODMR microscope.

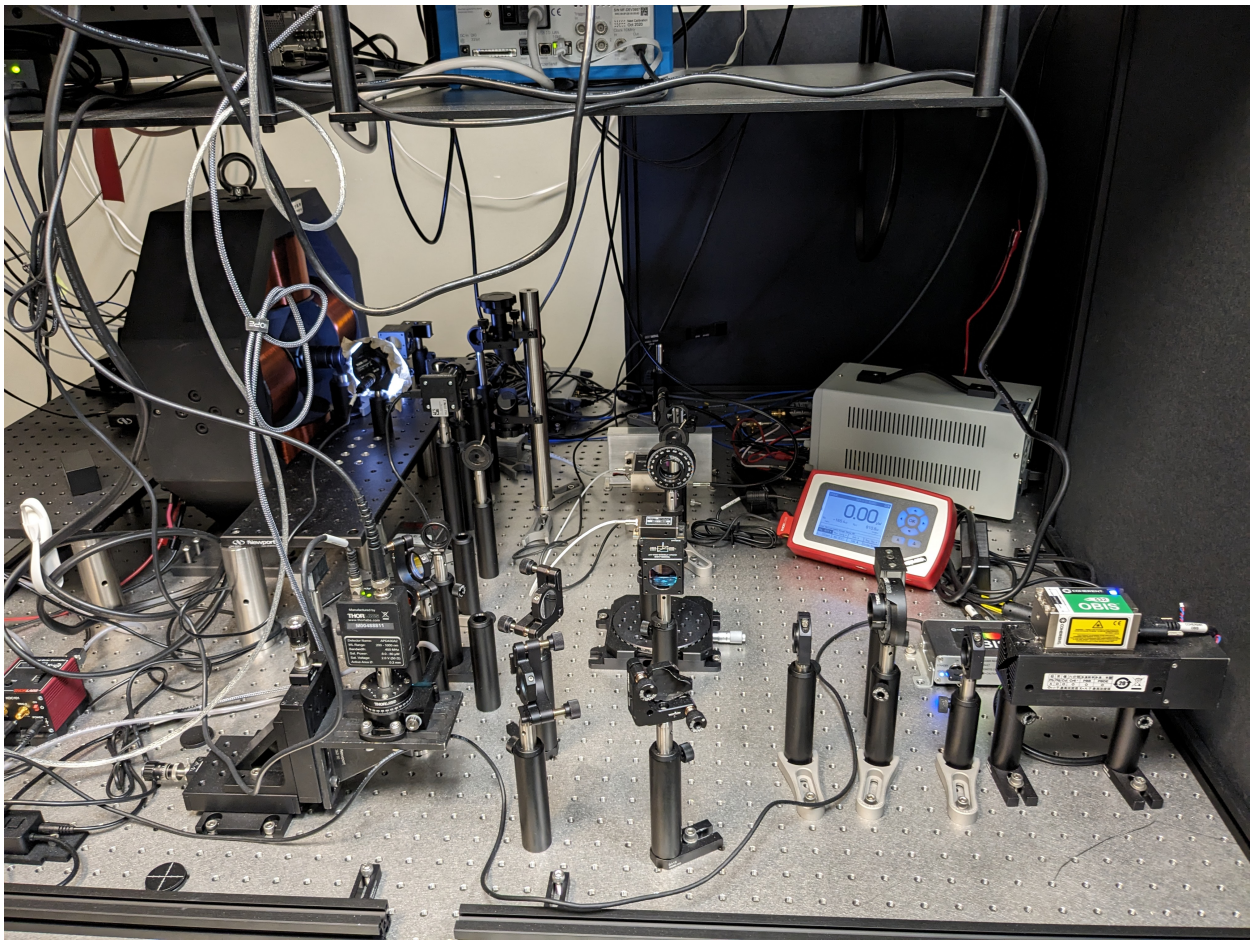

Figure 3.6: Final constructed setup with all components. Double-pass acoustic modulation scheme is implemented, and light is periscopically raised to level with the electromagnet mount.

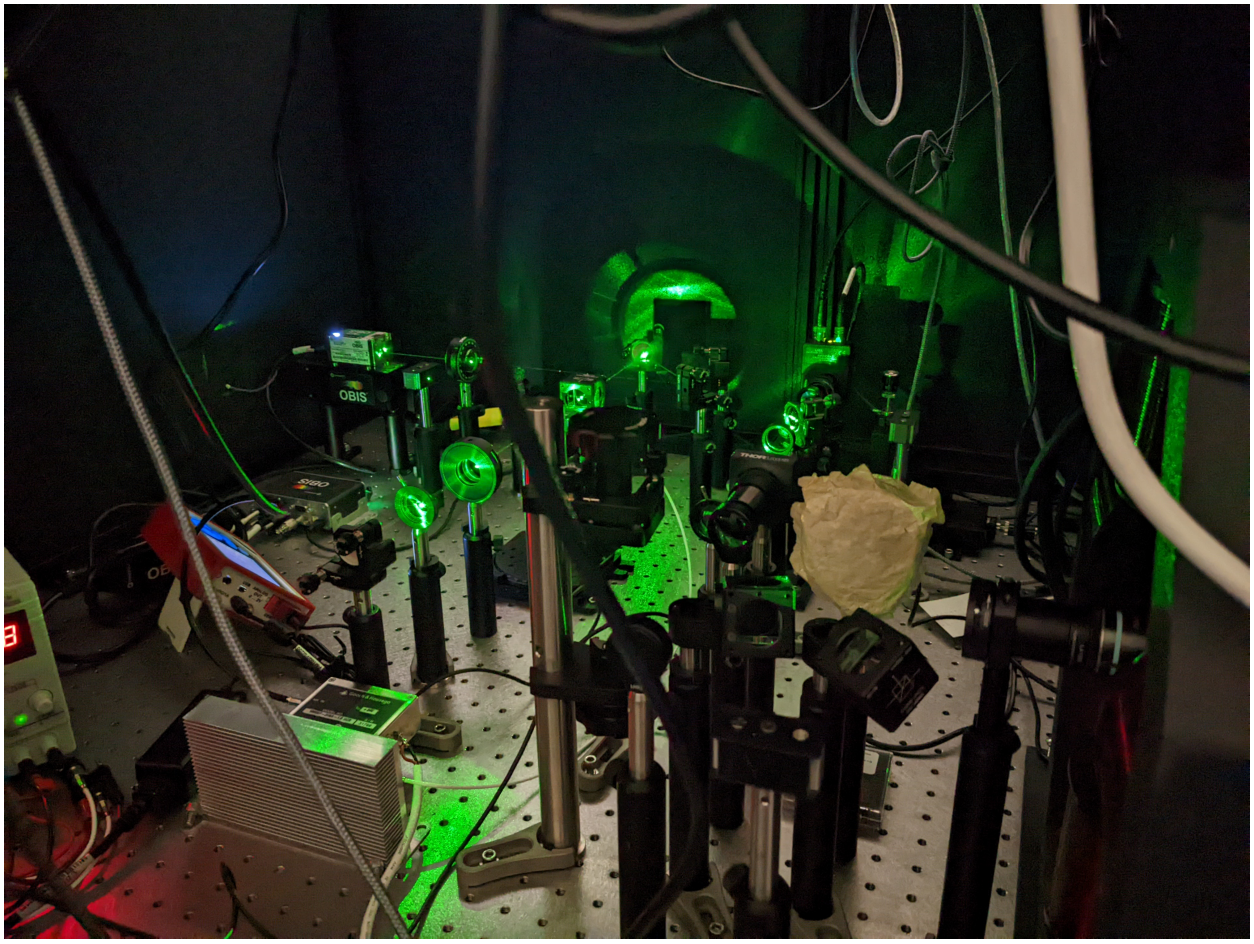

Figure 3.7: Picture of the setup when measurements are in progress.

Chapter 4

Coupling Magnetoelastic Waves and Nanodiamonds

In recent years, a wide variety of experimental results have been published in the literature exploring the coupling of ferromagnetic systems to nitrogen-vacancy defect centers [50, 25, 51, 52]. These studies have been performed via a range of techniques, including direct excitation of NV centers via magnons [23], interferometry between an external antenna and spin waves [53], and T_1 spin-lattice relaxation rate characterization [54]. In addition, direct elastic excitation has been used to excite coherent NV ensemble spin dynamics [19], an approach which also is compatible with dynamic decoupling pulse sequences [55].

Independently of this, the coherent conversion between phonons and magnons has been explored through theory and modelling. Based on acoustic and magnetic equations of motion, magnetoelastic mode shapes for simple plane-wave acoustic excitations in a ferromagnet have been derived [56, 57]. Furthermore, magnon-phonon conversion has been demonstrated experimentally [58], suggesting that NV centers can be coherently controlled by acoustically generated magnons through dipolar fields. In this chapter, we discuss the design and fabrication of a novel approach to interfacing with NV centers and other atomic defects via SAW-driven magnetoelastic waves. This approach combines the power efficiency of spin-wave driven excitation with the long-distance coherence of acoustic waves in a manner feasibly implementable in a commercial fabrication facility.

4.1 Fabrication of Solution Nanodiamond Devices

In many cases, NV centers are put in direct contact with a magnetic film to achieve the close proximity required for measurable magnon coupling. In cases where magnon dynamics are excited via an antenna or stripline, this is straightforward from a fabrication perspective; however, the resulting NV dynamics are a combination of direct antenna excitation and magnon coupling. On the other hand, should propagating magnons be used, the excitation source of the magnons must be approximately within the magnon propagation length of the

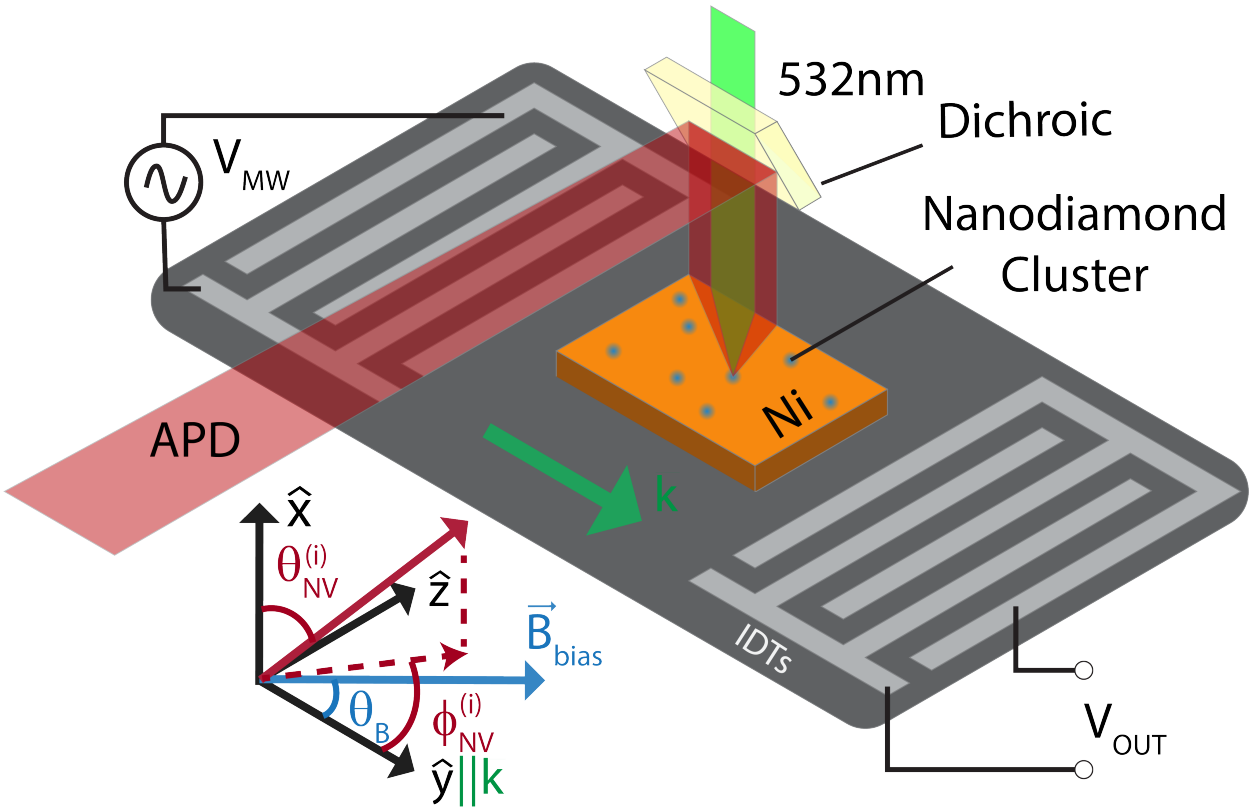

Figure 4.1: Structure of fabricated SAW device with a magnetic film and NV centers. NV centers are approximately randomly oriented, and their orientations are parameterized in spherical coordinates.

NV center.

When acoustic waves are used to excite the magnonic dynamics, this is no longer a challenge, however, a new set of fabrication complexities are introduced. For the results discussed immediately following, a magnetic film (Ni, 20 nm thick) was evaporated and lift-off patterned between FSL011 IDTs. The Ni film was 600 μm wide, much larger than the acoustic window of the IDT, and 300 μm long along the direction of acoustic propagation.

Droplets of a nanodiamond suspension in water containing NV centers (100nm diameter, 3 ppm NV concentration) were deposited on top of and adjacent to the Ni film, within the acoustic window of the IDTs; a diagram of the device is provided in Figure 4.1. Nanodiamonds were initially chosen over single crystal diamond due to commercial availability and a perceived ease of positioning relative to commercially available single-crystal diamond parts. Initially, nanodiamonds were deposited with the use of microsyringes, with typical volumes of 1 μL, as shown in Figure 4.2. However, SAWs are highly sensitive to the roughness of the propagation surface, and scattering effects off of the large droplets shown resulted in no

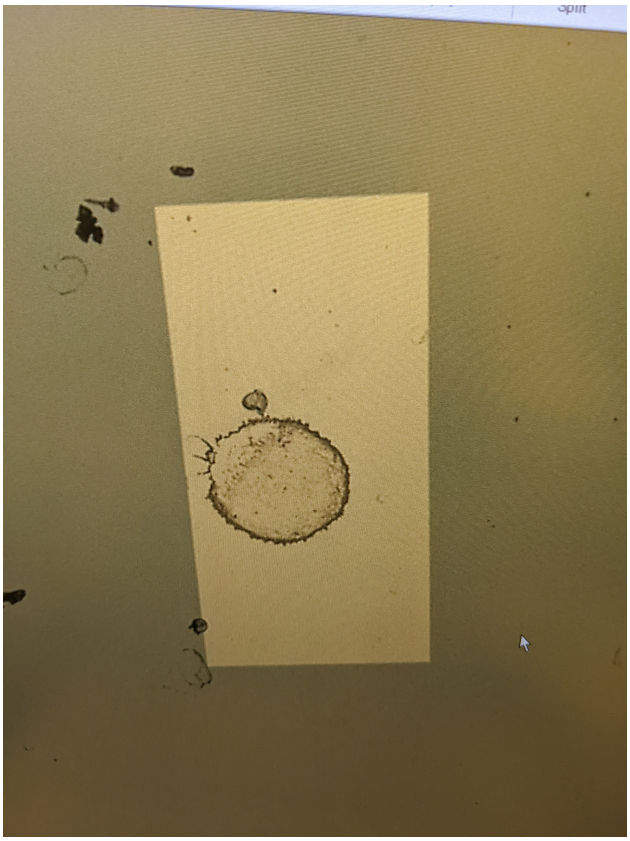

Figure 4.2: Initial attempt to deposit nanodiamonds on top of the magnetic film using a microsyringe. While droplets could be localized on the magnetic film, acoustic transmission was not detectable under these conditions.

measurable acoustic transmission.

As the smallest commercially available microsyringes were unable to deliver sufficiently small volumes of liquid for acoustic transmission, the Fujifilm Dimatix inkjet printer was used. As its print head is piezoelectrically actuated, it is capable of dispensing smaller droplets than the surface tension of water would normally allow; for the print head in use, single droplets had an approximate volume of 20 pL. A 10 drop pattern was printed twice. One pattern was intended to be positioned on the magnetic film pad, and one pattern was intended to be off, however, it was challenging to drop patterns repeatably, so the majority of both droplets were printed on the surface of the Ni pad. Regardless, stray droplets landed off the pad, and were sufficient to act as a control measurement. The resulting pattern is provided in Figure 4.3. The resulting NV proximity to device surface is estimated to be of the order of magnitude of the nanodiamond diameter, 100 nm, but is expected to vary significantly depending on the packing of the nanodiamonds.

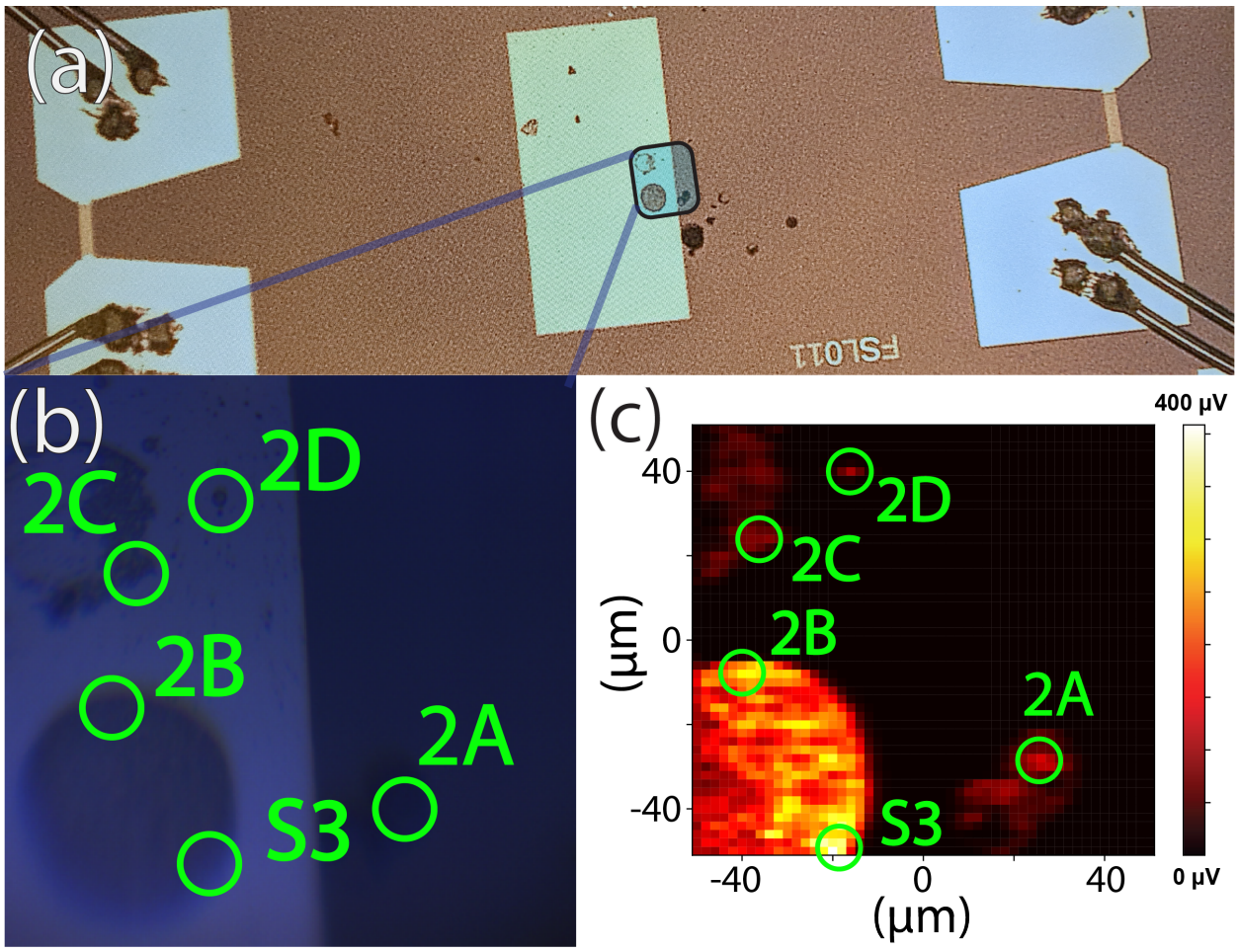

Figure 4.3: a) Droplet pattern resulting from inkjet printing using the Fujifilm Dimatix. The resulting droplets are an order of magnitude lower diameter, and measurable acoustic transmission is detectable at the receiver IDT with these present. b) Zoomed in image of the blue inset in part a. Areas where measurements were taken are labeled, with position 2A being located off the magnetic pad. c) Fluorescence intensity measured as a function of position in the same area as part b. Measured locations correspond to local fluorescence maxima

4.2 Dipolar Coupling Modelling

We model the ODMR spectrum of an NV center driven by a magnetoelastic wave using a combination of two existing models: a model for dipolar stray fields of spin waves [59] and a model of ODMR intensity for arbitrary nanodiamond orientation under magnetic field bias.[60] The first coordinate system is referenced to the geometry of the magnetic film and the direction of propagation of the magnetoelastic wave, such that $\hat{x}$ is perpendicular to the film, $\hat{y}$ is in the acoustic wave propagation direction, and $\hat{z} = \hat{x} \times \hat{y}$. In this coordinate system, the applied DC magnetic bias field $\vec{B}_{DC}$ is given by:

$$\vec{B}_{DC} = B_0 \begin{pmatrix} 0 \\ \cos\theta_B \\ \sin\theta_B \end{pmatrix} \tag{4.1}$$

Assuming that the magnetoelastic wave excitation takes the form of a spin wave with k-vector matching that of the exciting elastic wave, the expected stray field profile of the magnetoelastic wave is given by [59]

$$\begin{pmatrix} B_x(\vec{r}) \\ B_y(\vec{r}) \\ B_z(\vec{r}) \end{pmatrix} = \frac{\mu_0}{2} e^{-ik_\parallel x} e^{i\vec{k}_\parallel \cdot \vec{r}_\parallel} \int_{-t}^{0} dx' e^{ik_\parallel x'} \begin{pmatrix} k_\parallel & -ik_y & -ik_z \\ -ik_y & -\frac{k_y^2}{k_\parallel} & -\frac{k_y k_z}{k_\parallel} \\ -ik_z & -\frac{k_y k_z}{k_\parallel} & -\frac{k_z^2}{k_\parallel} \end{pmatrix} \begin{pmatrix} m_x(x') \\ m_y(x') \\ m_z(x') \end{pmatrix} \tag{4.2}$$

As the acoustic wavelength is much longer than the thickness of the Ni film, the exponential $e^{ik_\parallel x'} \approx 1$. The stray field above the magnetic film is found to be a circularly polarized drive approximately proportional to $\vec{m}_{avg} = \frac{1}{t}\int_{-t}^{0} \begin{pmatrix} m_x(x') \\ m_y(x') \\ m_z(x') \end{pmatrix}$, the average of the magnetization through the film thickness. In addition, $k_y = k$ and $k_z = 0$ in our coordinate system of choice. We define the oscillating magnetization components in terms of circularly rotating small-signal deviations from the DC magnetization direction, such that $m_x = \frac{1}{2}(m_R + m_L)$, $m_y = \frac{i\sin\theta_B}{2}(m_R - m_L)$, and $m_z = \frac{-i\cos\theta_B}{2}(m_R - m_L)$. The final oscillating stray field can be written as

$$\begin{pmatrix} B_x(\vec{r}) \\ B_y(\vec{r}) \\ B_z(\vec{r}) \end{pmatrix} \propto k \begin{pmatrix} m_x - im_y \\ -im_x - m_y \\ 0 \end{pmatrix} = k \begin{pmatrix} m_R(1+\sin\theta_B) + m_L(1-\sin\theta_B) \\ -i[m_R(1+\sin\theta_B) + m_L(1-\sin\theta_B)] \\ 0 \end{pmatrix} \tag{4.3}$$

Following this, we define an NV center orientation such that $\theta_{NV} \subset [0, \pi)$ is the angle between the NV axis $\vec{NV}$ and $\hat{x}$, and $\phi_{NV} \subset [0, 2\pi)$ is the angle between the projection of ϕ_{NV} in the Y-Z plane and $\hat{y}$. As a result,

$$\vec{NV} = \begin{pmatrix} \cos\theta_{NV} \\ \sin\theta_{NV}\cos\phi_{NV} \\ \sin\theta_{NV}\sin\phi_{NV} \end{pmatrix} \tag{4.4}$$

A second coordinate system is referenced to the $\vec{NV}$ and $\vec{B}_{DC}$ such that $\hat{z'} = \vec{NV}$, $\hat{y'} = \vec{NV} \times \hat{B}_{DC}$, and $\hat{x'} = \hat{y'} \times \hat{z'}$ sits in the plane of $\vec{NV}$ and $\vec{B}_{DC}$. The angle between $\vec{NV}$ and $\vec{B}_{DC}$ is given by $\cos\theta_{NV-B} = \vec{NV} \cdot \vec{B}_{DC} = \sin\theta_{NV}\cos(\theta_B - \phi_{NV})$. $\vec{B}'_{MW}$ is $\vec{B}_{MW}$ in the new primed coordinate frame.

Following the methods of [60], the unperturbed Hamiltonian of the NV center in the primed coordinate system is given by

$$\hat{H}_0 = D_{gs}(\hat{S}^2_{z'} - \frac{1}{3}\hat{S'}^2) + \gamma_e \hat{\vec{S'}} \cdot B'_{DC} \tag{4.5}$$

Evaluating the eigenvalues and corresponding eigenvectors, we can now list all possible transitions between states. Each transition is treated as a Gaussian centered at the transition frequency with a linewidth approximated as 54.2 MHz, based on the ODMR linewidth of nanodiamond ensembles also in [60]. The amplitude of each transition is given by

$$\begin{gathered}
\kappa = \langle\psi_f|\, \gamma_e \vec{B}'_{MW} \cdot \hat{\vec{S}'}\, |\psi_i\rangle\, |^2 (\Delta\langle\hat{\rho}\rangle)(\Delta\langle\hat{S}^2_{z'}\rangle) \\
\Delta\langle\hat{\rho}\rangle = \langle\psi_f|\, \hat{\rho}\, |\psi_f\rangle - \langle\psi_i|\, \hat{\rho}\, |\psi_i\rangle \\
\Delta\langle\hat{S}^2_{z'}\rangle = \langle\psi_f|\, \hat{S}^2_{z'}\, |\psi_f\rangle - \langle\psi_i|\, \hat{S}^2_{z'}\, |\psi_i\rangle \\
\hat{\rho} = \hat{I} - \hat{S}^2_{z'}
\end{gathered} \tag{4.6}$$

The nanodiamond clusters above the Ni film are assumed to be randomly oriented, and the ODMR signal is first calculated for an arbitrary NV crystal axis orientation. The NV center orientations are chosen in spherical coordinates following the probability distributions

$$P(\theta^{(i)}_{NV} = \theta) = \frac{1}{2\pi}, P(\phi^{(i)}_{NV} = \phi) = \frac{1}{2}\sin\phi, \tag{4.7}$$

such that $\theta^{(i)}_{NV}$ is uniformly distributed in the range $[0, 2\pi)$ and $\phi^{(i)}_{NV}$ is $\cos^{-1}(z-1)$ where z is uniformly distributed in the range $[-1, 1]$.

By summing over 10,000 NV centers and all available transitions for each NV-center, the ODMR signal strength for clusters of randomly oriented NV-centers orientation under varying applied in-plane magnetic bias field and frequency can be evaluated. The resulting ODMR pattern at a frequency of 2.6 GHz under radially swept magnetic field is plotted in Figure 4.4.

4.3 Solution Nanodiamond Experimental Results

To characterize NV center ODMR, IDTs were driven via a 2.6 GHz RF excitation at a power level of +15 dBm, pulsed at 5.74 kHz. The laser was pulsed at a frequency of 500 kHz; these frequencies were chosen to avoid any harmonic overlap. ODMR signal was collected via lock-in amplification of the fluorescence signal at the RF pulse frequency. Magnetic field was swept in amplitude and direction; prior to measurement at each angle, the field was raised

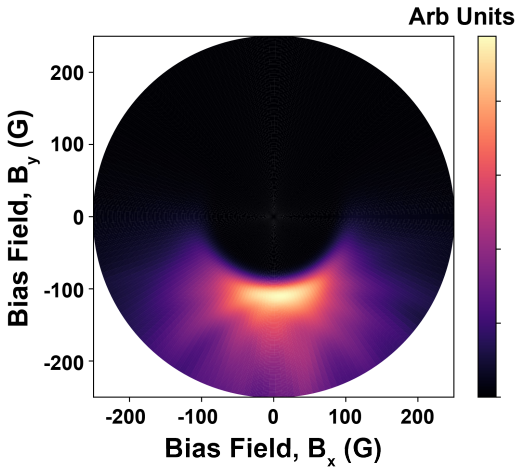

Figure 4.4: Simulated ODMR profile of randomly oriented nanodiamonds for different magnetization polarizations. A clear increase in signal strength at approximately 90 G is visible, occurring because the spin wave excitation frequency overlaps with the NV center transition.

to 500 G to saturate the magnetic film and electromagnet poles in repeatable fashion. First, ODMR response was measured at location 2A, corresponding to a nanodiamond cluster located off the magnetic pad, directly on the piezoelectric substrate. This location acts as a control, confirming that observed ODMR signals above the magnetic film are specifically due to magnetic dynamics, rather than due to piezoelectric response or radiation from the transducers. We observe no discernible fluorescence dependence on microwave excitation, as the measured signal sits at the lock-in amplified noise floor for all field values, as shown in Figure 4.5.

Following control measurement, the same magnetic field sweep was applied under measurement of each remaining location. All nanodiamond clusters were located within the acoustic window of the IDTs, however, locations 2B and S3 were located on a droplet closer to the edge of the window, while locations 2D and 2C were located on droplets approximately centered. Therefore, the expected acoustic power delivered to the magnetic pad in those areas is expected to be lower near the edge relative to the center. The resulting datasets are plotted in Figure 4.6. While the ODMR signal strength varied across all locations, this can be attributed primarily to the large variability in number of NV centers and delivered acoustic power. Acoustic power is likely the primary culprit, as SAWs are expected to scatter off surface roughness, and randomly oriented nanodiamonds would induce highly unpredictable scattering patterns. Regardless, two quantitatively distinct patterns are seen, and both patterns appear twice, providing strong evidence that these signals are replicable.

A comparison of the experimental results at locations 2B and S3 is provided in Figure 4.7. The resulting patterns, particularly in location 2B, display a strong match to the pre-

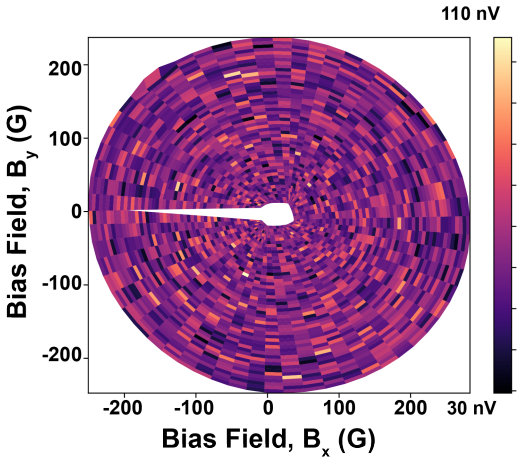

Figure 4.5: NV ODMR response under varying magnetic fields for Location 2A, off the magnetic pad. Measured lock-in signal is noise, confirming that the direct acoustic excitation and piezoelectric response have no effect on the NV center.

dictions of the dipolar field model. This suggests that the response is due to a coupling with a magnetoelastic wave containing a component with left-circular polarized magnetization. Strictly speaking, this does not rule out the presence of a right-circular component, as such a component would not be expected to couple strongly to the NV centers, as corroborated by the simulation and other studies in the literature [59]. Data in Figures 4.7a and 4.7c indicates that a field offset is present between the model and experimental data. This offset is challenging to explain directly, but plausible contributors are calibration error in magnetic field, imperfect randomness in the NV centers, and DC stray field from the magnetic film itself. For location S3, While noise levels are high, the qualitative dependence clearly matches location 2B and the model. The lower signal strength, despite location S3 having the highest overall raw NV fluorescence intensity, can be explained by lower acoustic power delivery, as location S3 is much closer to the acoustic window edge than any other location.

Before discussing locations 2C and 2D, we briefly introduce the ADFMR absorption pattern for this device, plotted in Figure 4.8. The pattern is consistent with theory and prior measurements detailed in Chapter 2, confirming that the nanodiamonds do not significantly impact the overall acoustic transmission. However, this does not exclude the possibility that significant acoustic scattering occurs within the spatially small magnetic areas below the nanodiamond clusters, simply that a majority of the acoustic power reaches the receiving transducer unimpeded.

For locations 2C and 2D, a cursory look will clearly show that they clearly do not match with the theoretical model. Furthermore, the resulting ODMR signals in these locations are much stronger than those seen in the dipolar coupling regime from locations 2B and S3.

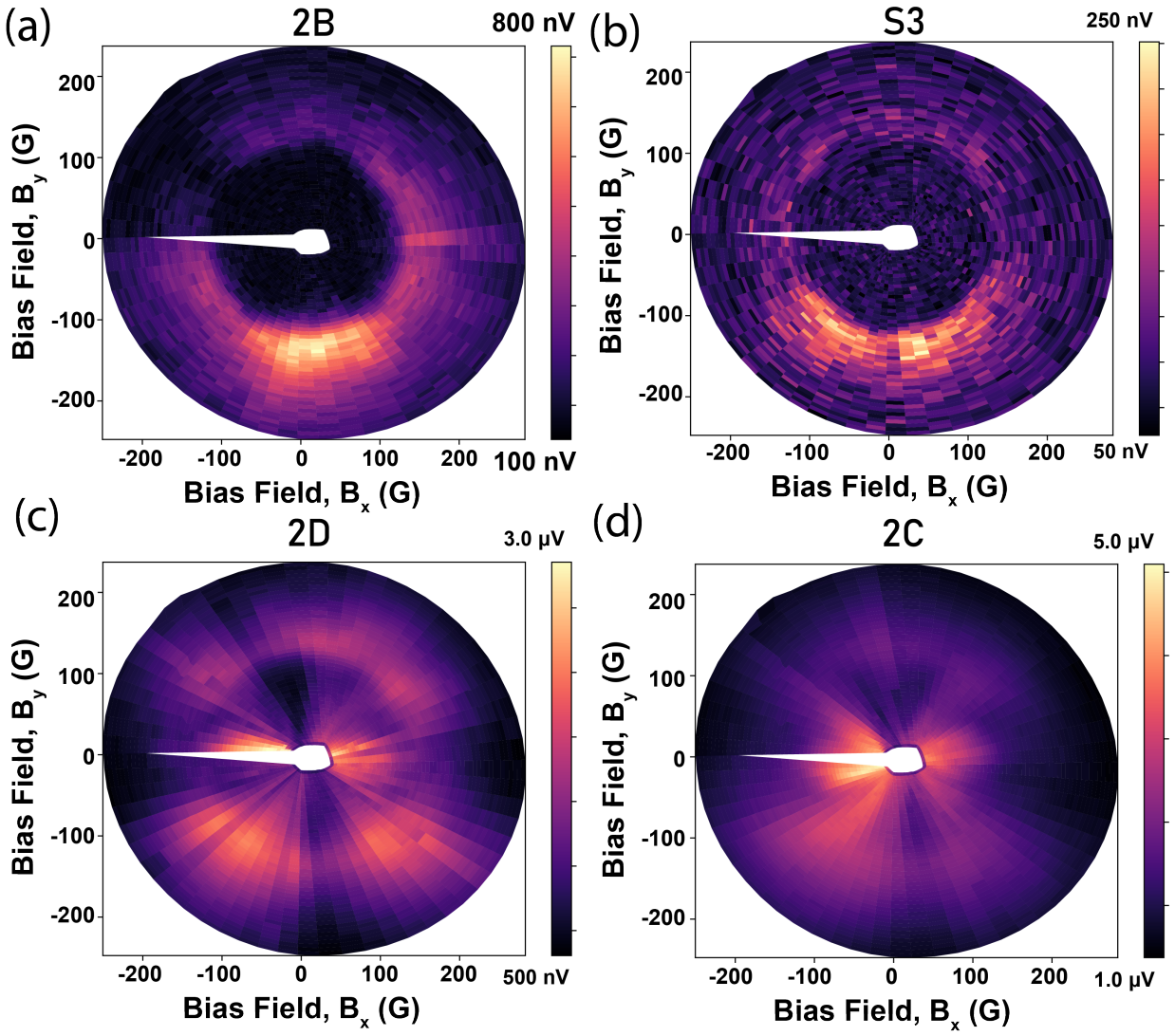

Figure 4.6: ODMR plots under varying magnetic field for locations 2B, S3, 2D, 2C. Two qualitatively different responses are seen, corresponding to two different nanodiamond droplets. (a-b) Locations 2B and S3 display a dipolar response consistent with a coupling to a spin-wave mode in the magnetic film. A visible Zeeman shift is seen, as ODMR signal increases significantly at a field of 90 G. Data here is nearly exactly consistent with the simulated response for a left-circularly polarized magnetic excitation. (c-d) Locations 2D and 2C display off-resonant coupling that cannot be explained by a linear magnetoelastic coupling.

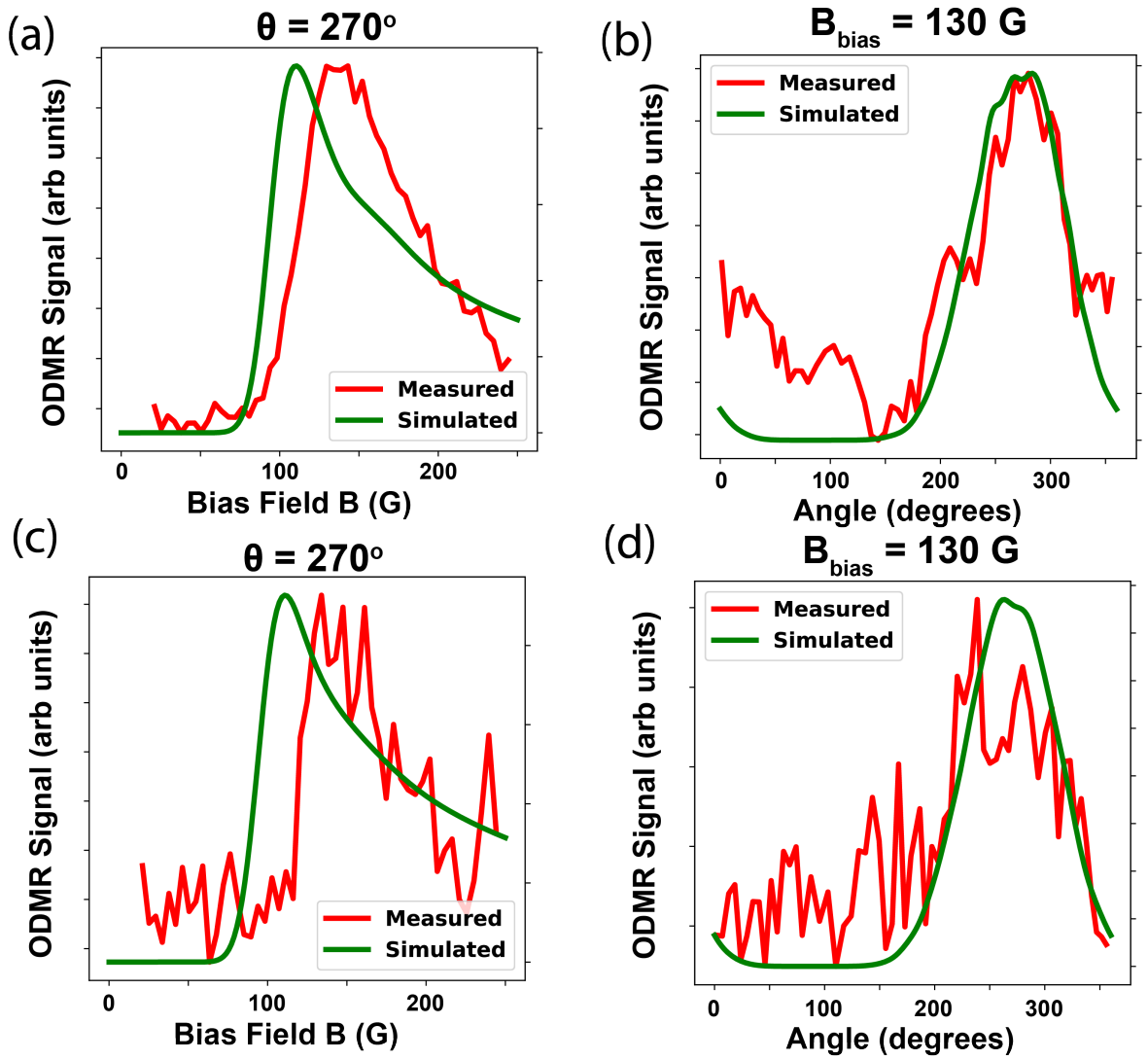

Figure 4.7: (a-b) Radial and angular line-cuts of the ODMR pattern for location 2B. The comparison shows a near exact overlap between simulation and measurement, but with an approximate field offset of 20 G. Angular dependence matches nearly exactly. (c-d) The same line-cuts for location S3, displaying a weaker and noisier, but qualitatively similar response.

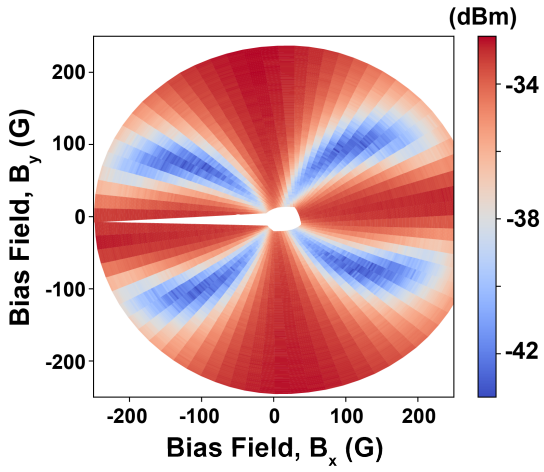

Figure 4.8: Measured magnetic field dependent ADFMR power absorption for the nanodiamond device discussed in this chapter. The device displays the 4-lobed absorption characteristic of ADFMR, similar to prior devices, indicating that the presence of nanodiamond clusters has not significantly impacted the device performance.

However, a closer look at the line-cuts, plotted in Figure 4.9, suggests that the dipolar model may still apply, but an additional, stronger coupling mechanism may be drowning out dipolar coupling. In particular, the angular cuts indicate an overlap between the ODMR signal and the ADFMR absorption lobes. Previous experimental work [61, 25, 62] has demonstrated a similar off-resonant response driven by both traditional ferromagnetic resonance and ADFMR at lower frequencies, and is hypothesized to originate from nonlinear damping effects within the magnet. Of particular interest is the strength of the response at near 0 field, which remains unexplained, but could be linked to the incomplete saturation of the magnetic film at low fields.

4.4 Fabrication of Single Crystal Diamond Devices

A major confounding effect preventing quantitative characterization of ODMR strength relative to delivered acoustic power was the scattering of the acoustic wave off nanodiamonds, which caused unpredictable variation in acoustic drive. As such, after demonstration of a dipolar coupling between magnetoelastic waves and nanodiamonds, the logical next step was to drive a single crystal diamond sample. Additionally, single crystal samples typically have significantly longer spin coherence times and narrower absorption linewidths, two parameters which are critical to quantum information and sensing applications. However, placing a diamond slab in direct contact with the magnetic film may result in acoustic energy transfer into the diamond film. This leads to two potential challenges: total acoustic losses will

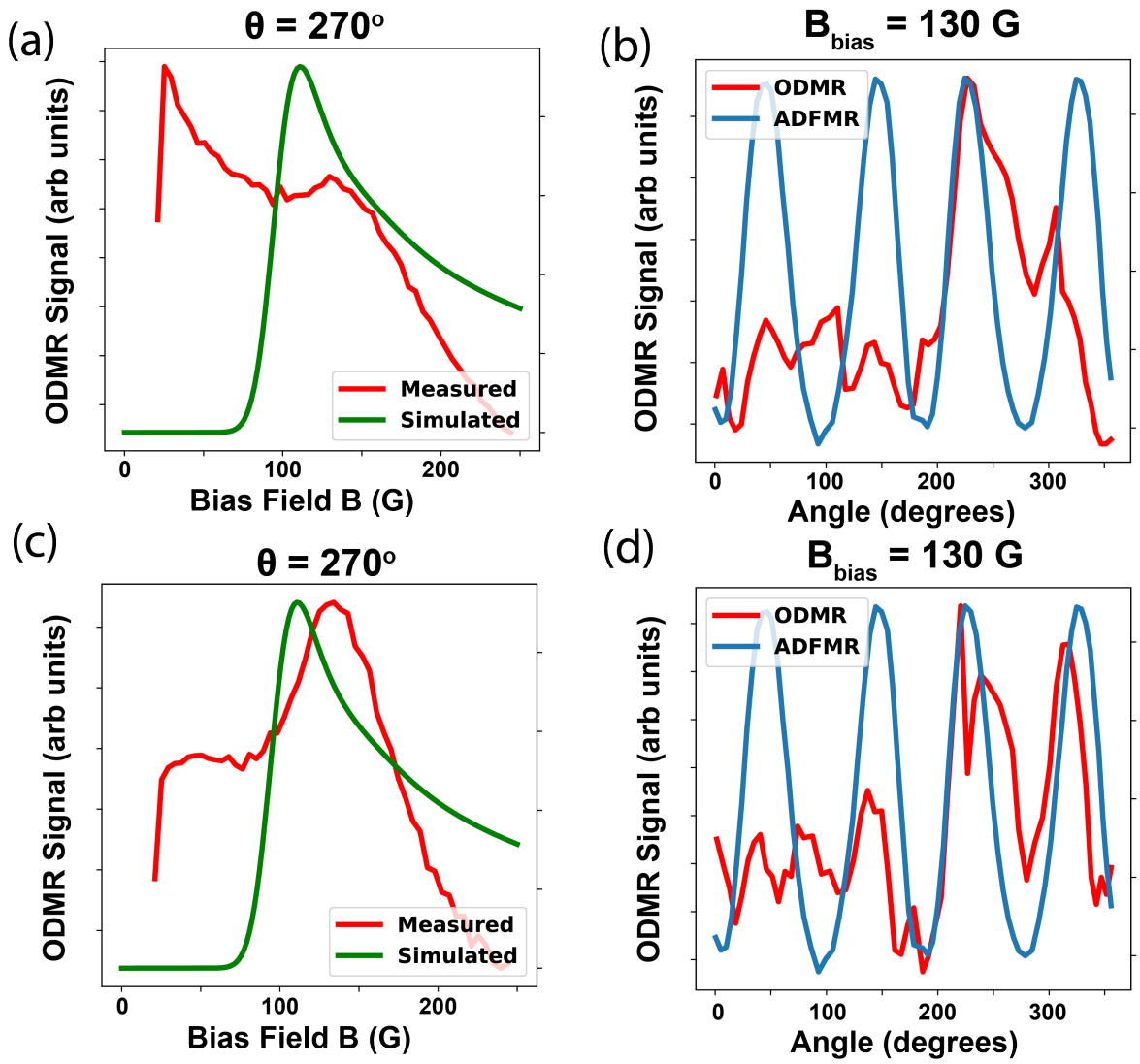

Figure 4.9: (a) Radial and angular line-cuts of the ODMR pattern for location 2C. A small peak is visible at the same field as seen in the dipolar regime, suggesting that the dipolar coupling is still present, but drowned out by a larger response. (b) Comparison of angular line-cut for location 2C to the ADFMR absorption. While strong noise due to acoustic scattering is present, ODMR maxima coinciding with the ADFMR absorption maxima are consistently present. (c-d) Identical line-cuts as in (a-b) for location 2D , displaying a similar appearance.

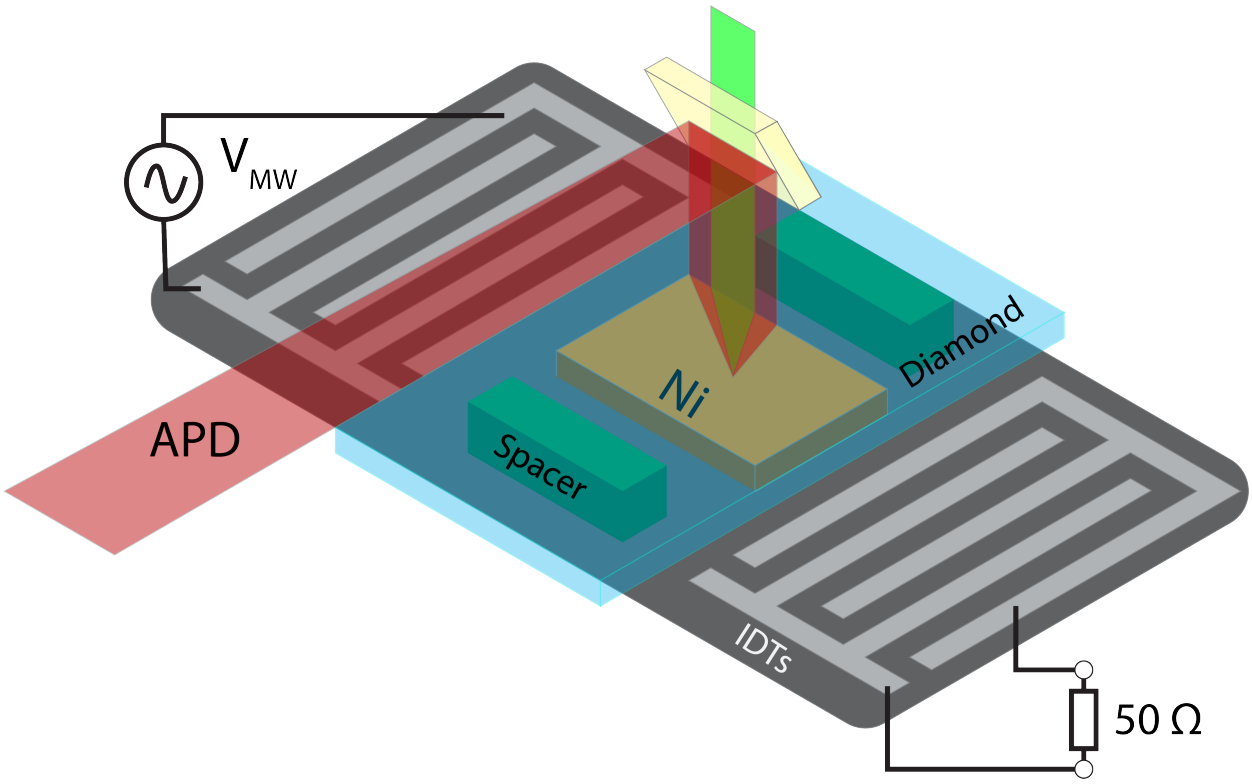

Figure 4.10: Structure of fabricated SAW device with a magnetic film and a diamond film separated from it by SU-8 spacer layers.

increase, and acoustic waves may directly interact with the NV centers as a confounding effect, as was intentionally demonstrated in [19].

To avoid this added complexity, photoresist spacers were patterned around the magnetic film, as shown in Figure 4.10. Due to the fact that TMAH-based developers can etch Al [63], SU-8 TF 6001 was chosen as the resist for chemical compatibility with the IDT material. This specific formulation of epoxy-based resist has low viscosity, and can be spun to thicknesses of approximately 1 μm. Following patterning, the remainder of the device was coated with another photoresist, and the SU-8 layers were etched via low power O_2 plasma. Following an acetone strip of the masking photoresist, the final SU-8 spacers were approximately 400 nm thick. The magnetic film was again 20nm thick Ni, but with smaller dimensions (200 μm wide, 50 μm) long. The change in dimensions was originally intended to make it possible to characterize data with bidirectional acoustic transmission.

Commercially available single crystal diamond samples (Thorlabs DNVB1) were diced by another commercial provider (Applied Diamond), yielding a 50 μm thick sample with a nominal NV concentration of 300 ppb. As the sample was mounted at a 90° angle to the ground, Kapton tape was used to secure the diamond to the surface, as shown in Figure

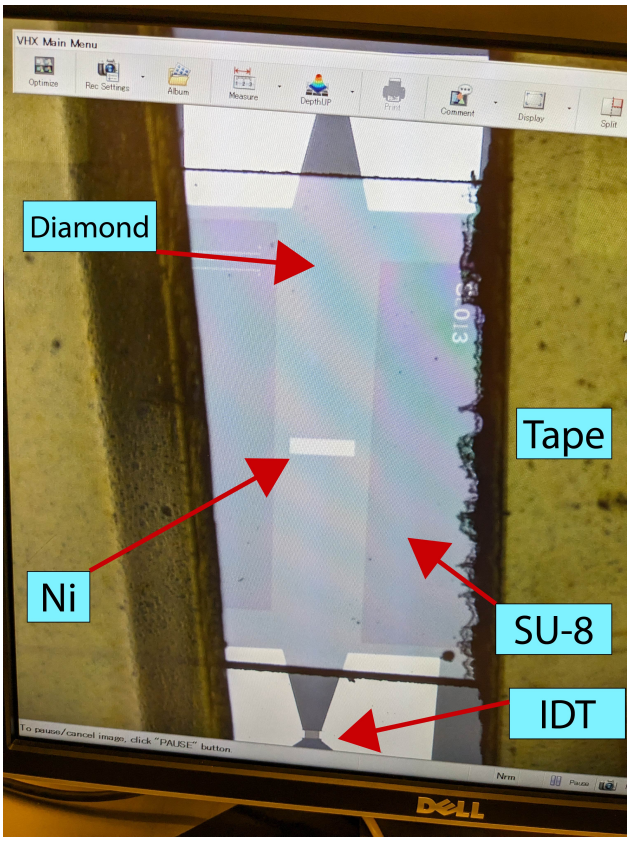

Figure 4.11: View of the taped down diamond film, mounted over a magnetic film. Dark rectangles to the left and right of the bright Ni film are SU-8 spacers.

4.11. During measurement, the laser focal plane was positioned approximately at the bottom surface of the diamond film, as determined by scanning the fluorescence intensity over objective lens spacing.

4.5 Initial Single Crystal Diamond Results

ADFMR absorption measurements were first taken on the taped device, plotted in Figure 4.12. This dataset was not calibrated to magnetic field, and is plotted with respect to current in electromagnet coils instead, though the range of field values approximately matches those used in the nanodiamond datasets above. The absorbed power is consistent with the expected absorption per unit length in the Ni film, though the field dependence of the absorption has significantly changed. The diamagnetic diamond would not be expected to have an impact on the field-dependence of the absorption, rather, the change in absorption lineshape is attributed to a difference in in-plane magnetic anisotropy due to the change in magnetic film

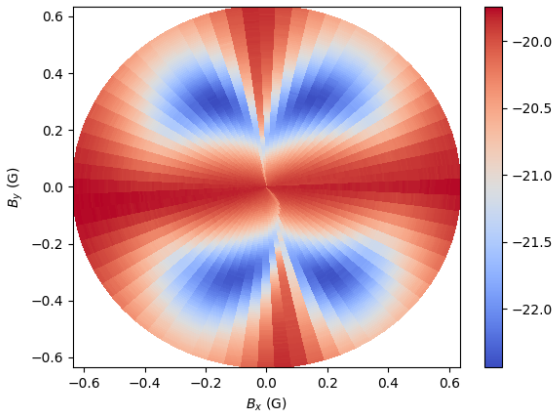

Figure 4.12: Measured ADFMR absorption for the device with a single crystal diamond taped over it. The difference in absorption pattern from Figure 4.8 is attributed to the change in magnetic film size and aspect ratio. This pattern is consistent with the presence of a uniaxial in-plane magnetic anisotropy, commonly seen in such devices.

size.

Following electrical characterization of ADFMR absorption, ODMR was characterized at a position at the center of the magnetic film with RF power +15 dBm, and the results are plotted in Figure 4.13. Within diamond, the theoretical depth of field of the objective was approximately 2 μm, significantly thinner than the diamond thickness of 50 μm. The position of the sample was adjusted such that the objective focal plane was roughly parallel to the bottom of the diamond, with a margin of error comparable to the depth of field. An approximately 2μm spacing difference was seen between the direct fluorescence of the diamond and its reflection off the metallic Ni film, suggesting that the true spacing of the diamond and NI film was not set by the SU-8 spacer, and may have been as large as 1 μm. This aligns with prior attempts to directly contact diamond films in the literature [53], where the limiting factor was dust particles on the substrate. The resulting ODMR signals are extremely weak and noisy, but approximately coincide with the absorption lobes seen in the ADFMR absorption. The weakness of the ODMR signal is attributed to the large diamond-magnetic spacing.

While this particular measurement is impractical as a quantitative tool for characterizing the interaction due to its weak intensity and noise, it provides confirmation that acoustic scattering was responsible for a large component of the noise observed in the nanodiamond datasets. When acoustic waves were allowed to travel unimpeded, ODMR coupling matched up exceptionally well with the ADFMR absorption lobes, confirming the presence of an off-resonant coupling mechanism. Ultimately, however, these results only serve to highlight the critical need for ODMR characterization of individual single-crystal NV-centers in very close

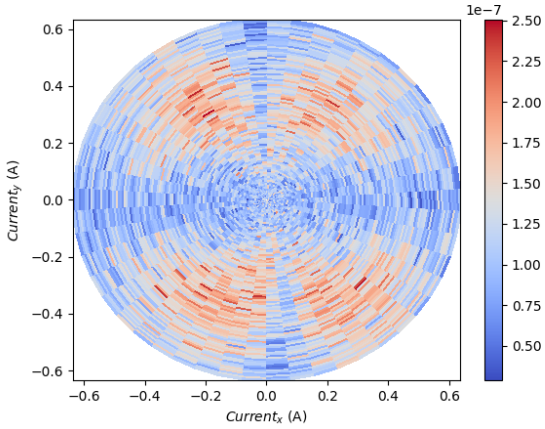

Figure 4.13: Measured magnetic field dependent ODMR power absorption for the single-crystal diamond device. Weak ODMR signals appear roughly overlapping with the ADFMR absorption lobes.

proximity to the surface of the magnetic film.

Chapter 5

Coherent Coupling of NV Centers and Magnetoelastic Waves

While randomly oriented nanodiamond NV centers were useful for initial exploratory studies, they are largely incompatible with quantum information applications and characterization. The quantum state occupied by each NV center under microwave drive has a time dependence linked to its relative orientation with respect to external magnetic field. Examples of coherent coupling to NV center ensembles have been largely limited to either single crystal diamond or individual nanodiamonds where the NV orientations are known relative to one another. [64, 23] In addition, even under highly optimized conditions, and with application of dynamic decoupling sequences to extend coherence time, nanodiamond-based NV centers display short coherence time relative to single-crystal diamond samples [65, 14]. This, in conjunction with the collection of fluorescence from many nanodiamonds simultaneously, means that it is infeasible to perform spin-state readout of any particular NV center with the experimental setup detailed in Chapter 3. As a result, while the dipolar coupling mechanism discussed in Chapter 4 would be expected to allow coherent transfer of information between an acoustic wave and the NV center, the nanodiamond results shown do not definitively demonstrate that such information transfer is possible. In this chapter, using an NV center in single-crystal diamond, we show that quantum information can be transferred between a SAW and an NV center mediated by a ferromagnet, and discuss additional measurements which suggest further avenues for research.

5.1 Experimental Configuration

A commercial product (QZabre AG, Quantum Scanning Microscope) capable of single-NV characterization using a scanning AFM tip was used to collect the data discussed in this chapter. A diagram of the experimental configuration is provided in Figure 5.1. In particular, unlike with the inkjet printed nanodiamonds, it was possible here to control the spacing between the NV center and the magnetic film. Throughout all measurements, the AFM tip

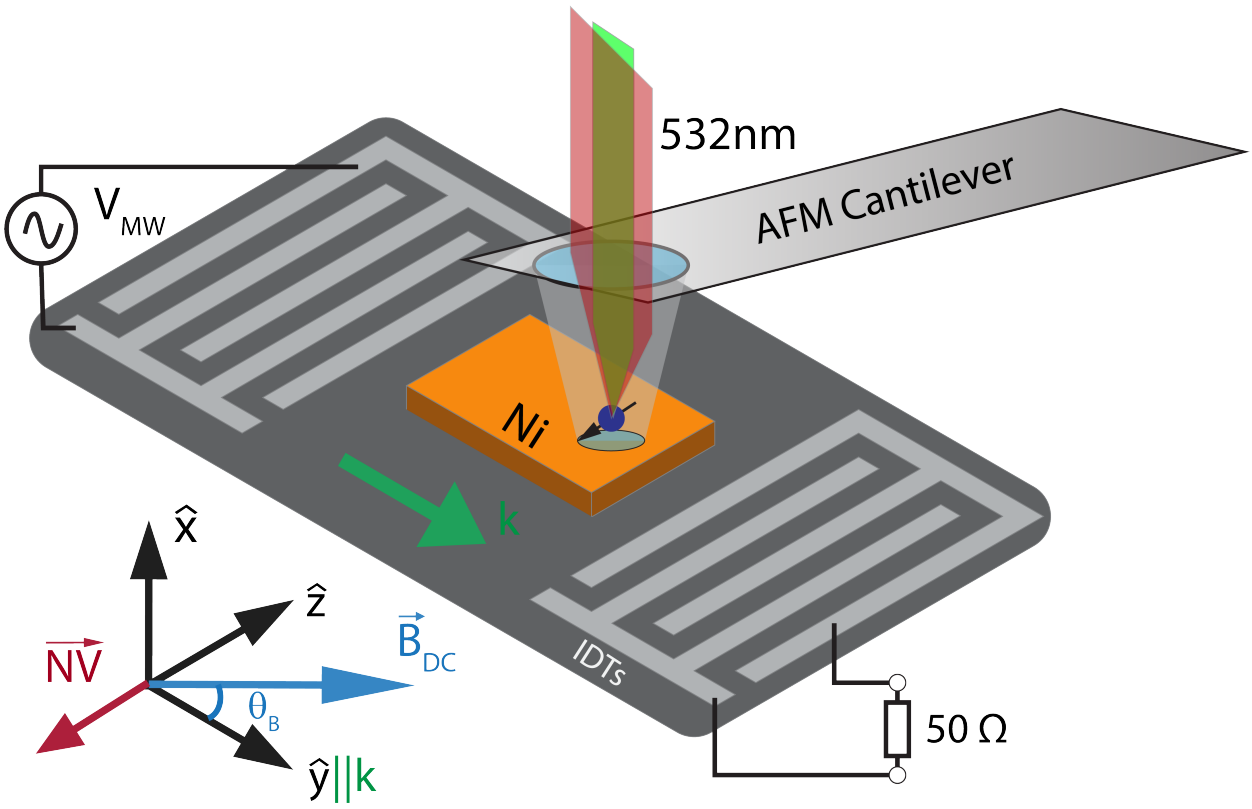

Figure 5.1: Diagram of experimental configuration. A QZabre-provided tuning-fork AFM tip containing a single NV center is positioned at the focal point of the laser in proximity to the magnetic film. The NV center was approximately oriented in the $-\hat{z}$ direction, while the acoustic wave propagated in the $\hat{y}$ direction.

was brought into contact with the magnetic film and then lifted via a piezoelectric stage periodically, with a time between corrections of 30 seconds. Due to active vibration isolation and temperature control within the measurement area, the resulting mechanical error was estimated to be at worst 5 nanometers. A photograph of the device loaded into the microscope chamber is provided in Figure 5.2; under normal measurement operation the microscope is enclosed within a structure to limit dust and airflow, and to control temperature.

FSL014 IDTs were wirebonded to the QZabre mounting PCB, and a 20nm thick, 200 μm wide, 500 μm long magnetic film was patterned in between the IDTs. The NV center AFM tip was, for all measurements detailed here, positioned within the center of the IDT acoustic window, approximately 10 μm away from the edge of the magnetic film closest to the transmitter IDT. ODMR contrast was measured across both a radially swept magnetic field and across excitation frequencies varying from 2.45 GHz to 2.75 GHz, a frequency range containing the full bandwidth of the FSL014 IDTs. Due to mounting alignment error, the

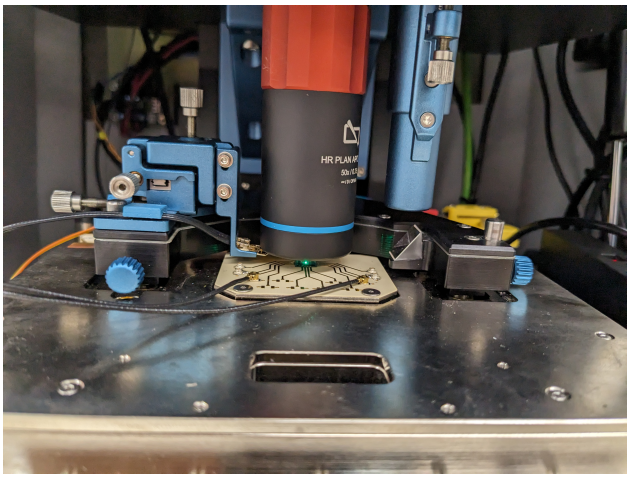

Figure 5.2: Photograph of device wirebonded and mounted in the QZabre Quantum Scanning Microscope. A piezoelectric stage is used to position the device, providing significantly improved positioning accuracy compared to motorized stages in prior measurement.

sample was rotated by approximately 5 degrees relative to the electromagnet pole axes, a rotation which is visible in the datasets below.

5.2 Single NV ODMR Results

As three different parameters were swept, the total datasets are impractical to plot in their entirety. Figures illustrating key results and conclusions are provided in this section, either by plotting the dataset under fixed frequency or magnetic field direction. Initial measurements were focused on replicating the nanodiamond datasets and identifying configurations which could isolate the dipolar and off-resonant coupling mechanisms from each other. To this end, measurements were taken at various RF input powers, and illustrative plots are provided in Figure 5.3. It is seen that at sufficiently low power, the off-resonant effects are negligible, and the dipolar coupling can be isolated. At high powers, however, a broadband ODMR response is observed across the full bandwidth of the IDTs, overlapping with the measured dipolar NV transition. This broadband response is by far the largest at low fields, and is seen to decrease with increasing magnetic field amplitude. Of particular interest here, these magnetic bias conditions do not coincide with the primary ADFMR absorption response, but suggest that even when longitudinal ADFMR absorption is minimal, significant incoherent magnetic dynamics are excited. A possible explanation is that the shear wave component of the Rayleigh wave, which would be expected to induce a strong response at this magnetic field bias, could be responsible for these incoherent dynamics.

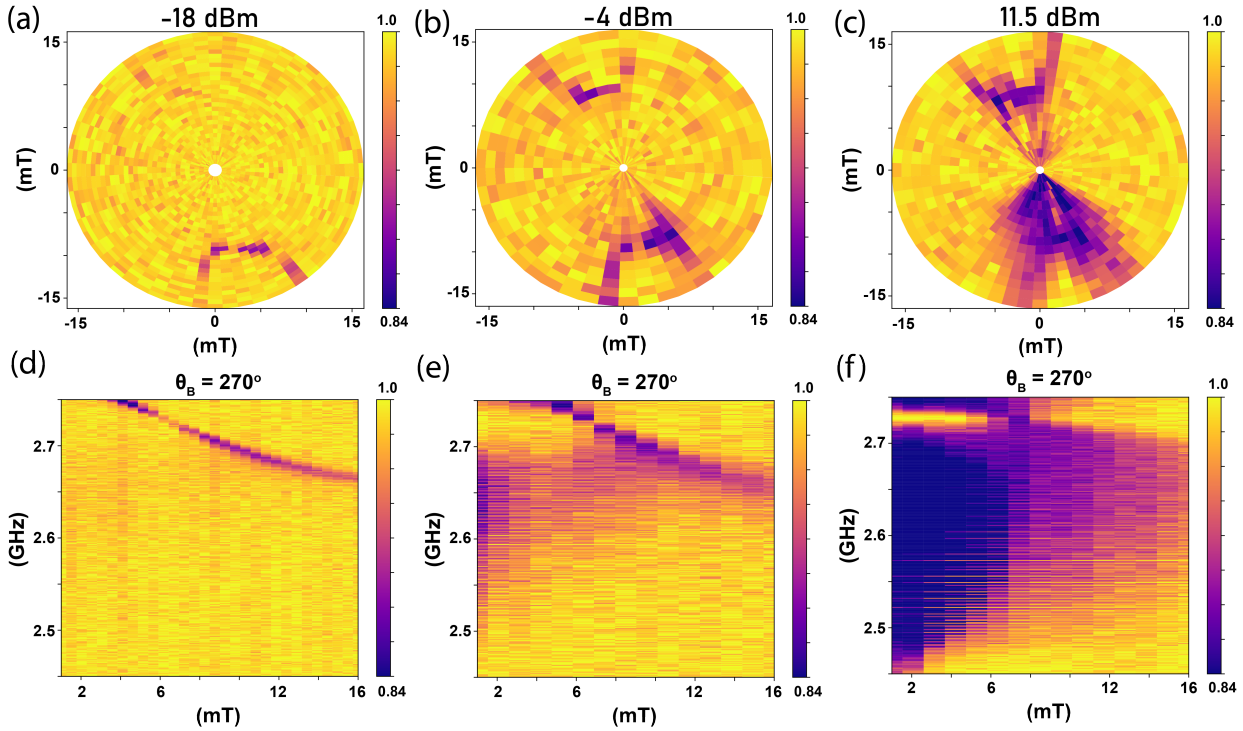

Figure 5.3: All measurements were taken with a tip-magnet spacing of 150 nm, with a laser excitation power of 2 mW. (a-c) ODMR contrast dependence on magnetic field at a frequency of 2.7 GHz for various input powers. At lowest power, a single energy level transition is visible, while at high power, ODMR response is seen across a wide range of magnetic fields. (d-f) ODMR spectrum when magnetic field is applied at 270° to the acoustic propagation direction. A single energy level following a Zeeman transition is seen at low power, at high power, ODMR is observed across the full acoustic transmission band. The region of no ODMR response at 2.72 GHz coincides with a minimum in acoustic transmission for this IDT, further confirming that the signal is acoustically modulated. Also visible is a broadening of the microwave linewidth of the NV energy levels as power is increased.

Power Dependence of Coupling

To confirm the hypothesis that dipolar coupling is responsible for the low power response, we repeat the modelling process detailed in Chapter 4 for the single NV orientation used here across the frequency range of interest. A comparison of experimental and modelling results is provided in Figure 5.4. While magnetic anisotropy and NV-axis alignment error can contribute to the discrepancy between the model and experiment, the qualitative overlap between the patterns makes it clear that this transition corresponds to a dipolar-driven energy level of the NV center. However, a significant deviation between the modelled pattern is present in the measured data. This deviation is similar to the nanodiamond data in that

for a given frequency, the observed ODMR occurs at a higher field bias than predicted. One partial contributor to this effect could be alignment error of the NV center, however, fully explaining this deviation would require an alignment error of over 45 degrees, which is unlikely to be the case. A definitive explanation of this discrepancy will require further study.

Following variation in delivered power, the effect of changing standoff distance between the NV center tip and magnetic film surface was explored. Under a fixed microwave and optical power, ODMR contrast measurements were taken at distances of 500 nm, 250 nm, and 150 nm, and the results are plotted in Figure 5.5. The effect of increasing standoff distance is qualitatively very similar to decreasing power, a response that is unsurprising given that dipolar fields are expected to decay exponentially with increasing standoff distance.

Standoff Distance Dependence of Coupling

Of particular interest here is the presence of ODMR contrast coinciding with the NV center energy level within the transmission minimum of the IDT pair at 2.72 GHz. At this frequency, the transmitted acoustic power is approximately three orders of magnitude lower than the excitation at 2.67 GHz, but still displays strong ODMR response. Such an excitation would be comparable in magnitude to the triple-transit signals at the center frequency of 2.67 GHz, suggesting that these triple-transit SAWs can contribute to the measured ODMR spectrum. This is a plausible explanation for the presence of ODMR signals at magnetic bias field $\theta_B = 90°$, which is not predicted by the dipolar model.

Another observed effect, which remains largely unexplained at this stage, is the variation of ODMR resonance with standoff distance at a fixed applied field bias, particularly at very close distances to the magnetic film surface, for which illustrated data is plotted in Figure 5.6. The ODMR resonance is seen to split into two separate resonances at distances of approximately 100 nm from the surface of the film. While this is not visible in the available dataset, during data collection, the exact amount of splitting appeared to change over timescales of seconds; a scale that suggests mechanisms other than acoustic propagation and magnetism may be responsible. Thermal mechanisms may be responsible, but further study of this effect is critical to understand its origin fully.

Laser Effects on ODMR

The effect of increasing laser intensity on the measured ODMR signal is plotted in Figure 5.7. Typical ODMR measurements performed on the QZabre system using an antenna as an RF power source regularly use laser powers in the 10s of mW, indicating that laser interactions with the magnetic film are the likely cause of the observed decay of ODMR signal with power. While the precise cause of this process has not been determined, light is known to interact with ferromagnetic materials in a wide range of ways, causing a variety of effects. One hypothetical approach that may hold promise for explaining this data is Brillouin Light Scattering (BLS) spectroscopy [66]. While outside the scope of this thesis, BLS spectroscopy

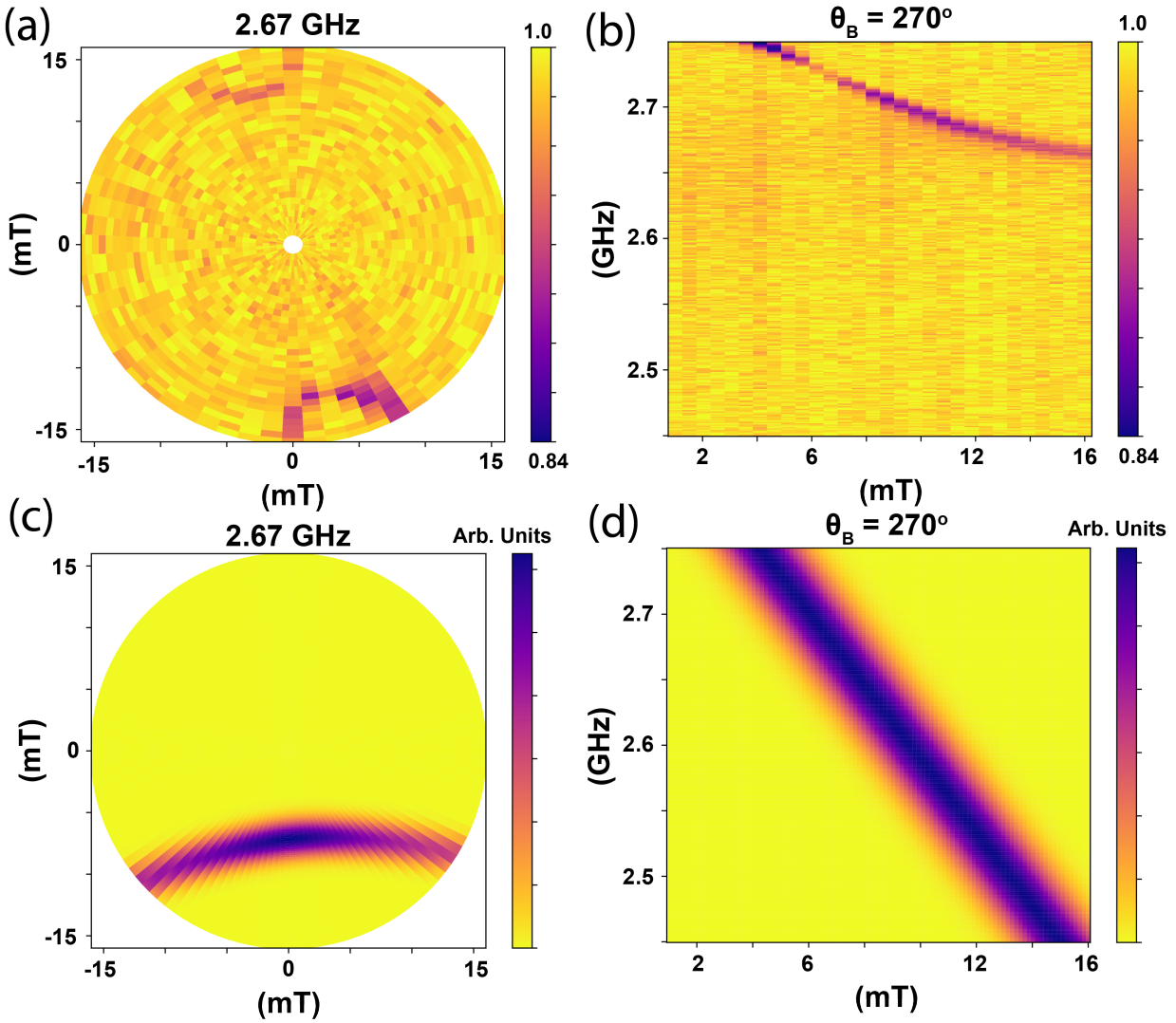

Figure 5.4: Comparison of experimental and modelling data, for a 150 nm NV-magnet spacing, with laser power of 2 mW and RF power of -18 dBm. (a) Measured ODMR response at 2.67 GHz, the frequency where acoustic transmission is maximized. (b) ODMR spectrum for magnetic field applied at 270° to acoustic propagation. (c-d) Modelled ODMR spectra under equivalent conditions. A similar field offset as seen in the nanodiamond dataset is observed here, where the measured ODMR spectra occur at higher fields than simulated. Additionally, alignment error in the NV-axis and magnetic anisotropy can further contribute to deviation from the model.

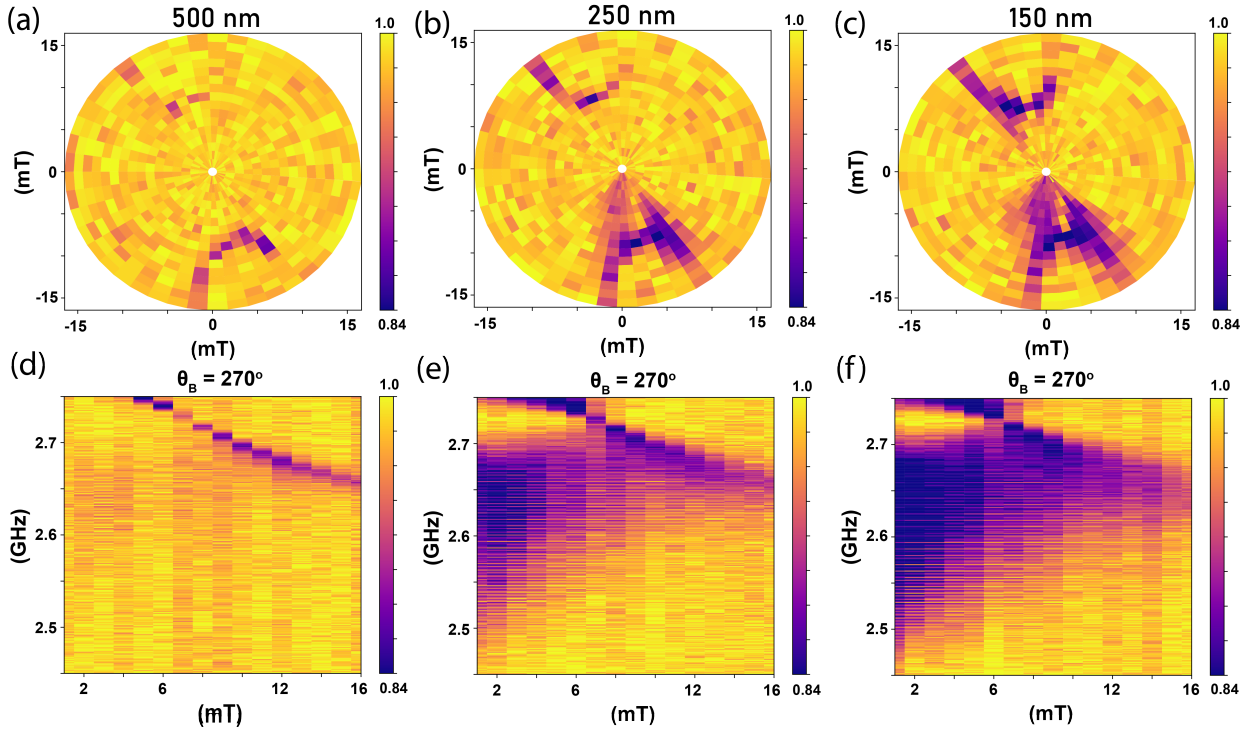

Figure 5.5: Measurements were taken at a microwave power of +2 dBm, with a laser excitation power of 2 mW. (a-c) ODMR contrast under varying magnetic field at a frequency of 2.7 GHz for various standoff distances. As the NV and magnet are brought into proximity, the strength and linewidth of the NV center ODMR increase, and an off-resonant response appears at low fields. (d-f) ODMR spectra for magnetic field applied at 270° to acoustic propagation. Again, the broadband ODMR response at low fields is observed in close proximity to the magnetic film, and is seen to span the transmission band of the acoustic IDT.

of magnetoelastic waves has been explored in prior work, and may be a promising path to understanding this effect further [67].

Isolation of Dipolar Coupling and Rabi oscillations

Given these datasets, the final goal of these measurements was to identify the conditions where a magnetoelastic excitation could be used to coherently excite NV dynamics. The dipolar coupling mechanism was hypothesized to be possibly coherent. To further confirm that a single NV energy level was being driven, the ODMR spectra are plotted for various frequency and field orientations in Figure 5.8. Assuming the dipolar model to be correct, the ODMR excitation behaves in a manner consistent with the Zeeman effect.

Once an NV energy level transition was identified, it was driven by RF pulses in a stan-

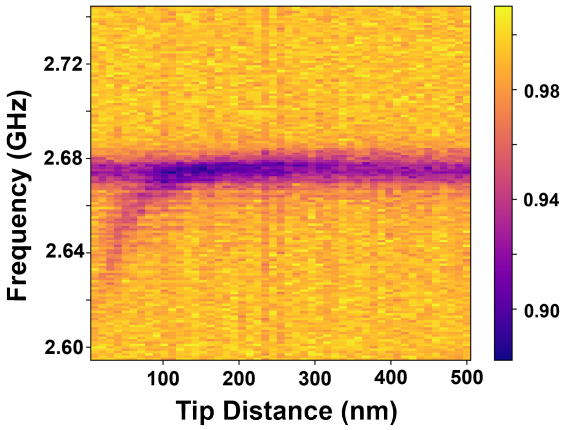

Figure 5.6: ODMR resonance frequency under a magnetic field of 10 mT at an angle of 270° to the acoustic propagation direction. A splitting into two separate resonances is observed at very close proximity to the magnetic film. This splitting appeared to decrease over timescales of seconds, suggesting that a mechanism not discussed in this work may be responsible.

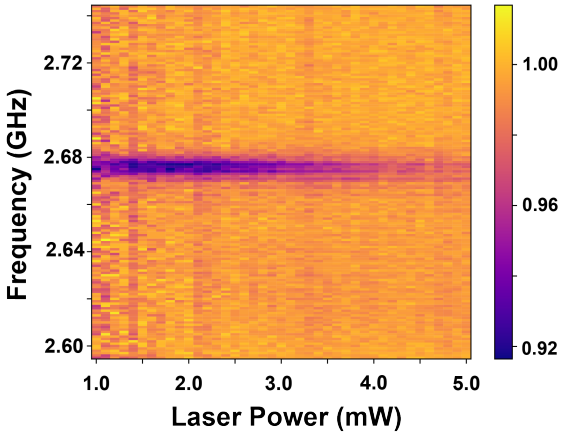

Figure 5.7: Plot of ODMR spectrum under increasing laser excitation power. Spectrum is measured at an RF power of -24 dBm, with standoff distance of 100 nm, and a magnetic bias field of 10 mT at a 270° angle to propagation, coinciding with the maximum dipolar ODMR contrast. The ODMR signal is seen to decay with increasing laser power, eventually decreasing to the point where it is not detectable.

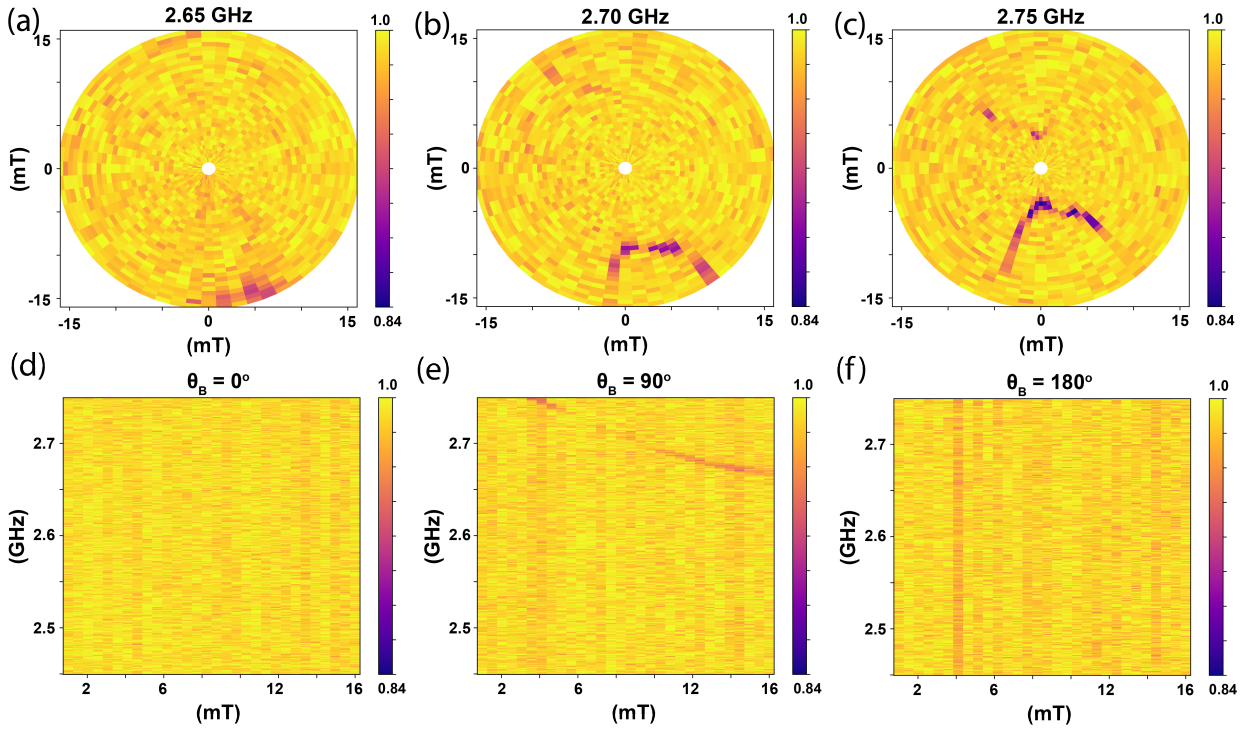

Figure 5.8: Data taken with a standoff distance of 150 nm, laser power of 2 mW, and RF power of -18 dBm. (a-c) ODMR dependence on magnetic field at various frequencies, displaying a response qualitatively consistent with the Zeeman effect. (d-f) ODMR spectra at various magnetic field bias angles. No signal is observable with magnetic field parallel to acoustic propagation, consistent with the expected dipolar field from a propagating spin wave. When magnetic field is at 90° to acoustic propagation, a weak ODMR signal is seen. This effect is hypothesized to be linked to weaker SAW reflections exciting magnetoelastic waves propagating in the reverse direction.

dard Rabi pulse sequence, shown in Figure 5.9; the resulting ODMR contrast is plotted in Figure 5.10. An oscillation is clearly visible, confirming the phase coherence of the magnetoelastic excitation. Furthermore, based on the geometry of the device and Rayleigh wave speed, the reflected acoustic pulse is expected to arrive at the position of the NV center 0.6 μs after the initial pulse passes through. We expect to see a partial loss of coherence with pulse lengths above that duration, as the reflected pulse will introduce an acoustic interference pattern. A clear increase in deviations from the Rabi oscillation fit is visible at that pulse duration, and longer durations display increased fitting error.

In short, under appropriate magnetic bias conditions, magnetoelastic waves have been demonstrated to generate phase-coherent stray dipolar magnetic fields, which can be used to drive spin dynamics in the nitrogen-vacancy defect center. Interestingly, this phase-

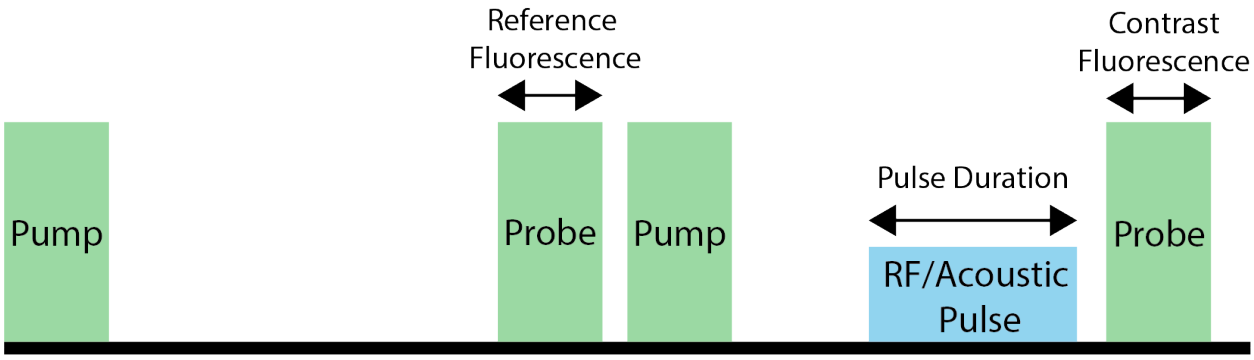

Figure 5.9: Pulse sequence for a standard Rabi oscillation measurement. A reference fluorescence intensity is measured following a fixed time delay. In a subsequent measurement, a microwave pulse, or in this case an acoustic pulse, is used to drive a transition in the NV center, following which the new fluorescence is measured. If the magnetoelastic wave drive is phase-coherent, under increasing pulse duration, the fluorescence is expected to display an oscillatory behavior with increasing pulse duration, corresponding to a coherent transition between the fluorescing and non-fluorescing NV states.

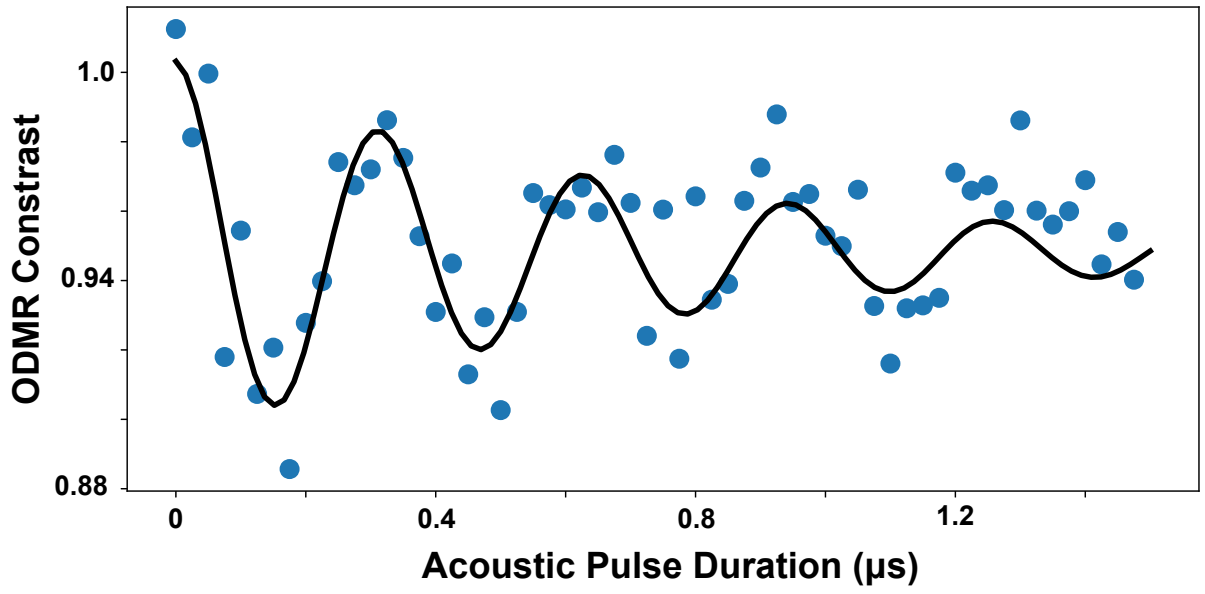

Figure 5.10: Measured ODMR contrast as a function of microwave pulse length, and a corresponding fit to a sinusoidal Rabi oscillation function. Deviation from the fit increases at pulse lengths of 0.6 μs, corresponding to the duration where a reflected acoustic wave would be expected to influence the NV fluorescence.

coherent coupling appears to occur under magnetic bias conditions where a Rayleigh mode excitation would not be expected to induce strong magnetic dynamics [8], indicating that a linear model of magnetoelasticity may only provide a complete description of these effects. However, the dynamics observed are very similar to the expected profile of a coupling to a coherent magnon mode [59], providing indirect evidence of a coherent magnon-phonon conversion under appropriate conditions.

One unique advantage of this approach is that these dipolar fields display a circular polarization, which allows spin-selectivity in the NV transition, a potentially useful feature for hypothetical spin qubits based on the NV center. Replicating this particular property in a traditional antenna system has been performed experimentally in the literature, but puts additional design constraints on an already nontrivial antenna design problem [68]. This excitation occurs even in polycrystalline Ni, suggesting that a long spin coherence length is not critical to this driving mechanism, and that a broad range of magnetic materials may be compatible with this approach. Critically, this implies the potential to excite coherent spin wave dynamics using materials beyond Yttrium Iron Garnet (YIG), potentially alleviating performance compromises associated with integration of spin wave devices.

Chapter 6

Summary and Outlook

In this work, we have investigated the phenomenon of acoustically driven ferromagnetic resonance and its coupling to the nitrogen vacancy defect center in diamond. We have demonstrated that the interaction contains a phase-coherent dipolar coupling, and have provided conditions where this coupling can be isolated from other incoherent mechanisms. Here we conclude with a brief summary of the major results and give an outlook for future work in the field. Continuing this work further should provide a deeper understanding of the underlying magnetoelastic dynamics, as well as suggest potential avenues toward practical integration of defect centers in sensing and quantum information applications.

6.1 Summary of this thesis

Chapter 2 of this thesis overviews the underlying physics behind magnetoelastic coupling, and introduces the structure of a typical characterization device. We discuss the structure of the Rayleigh mode, and provide parameters for reconstructing a 2-D model of the mode for the devices discussed throughout the remainder of the thesis. The origin of the 4-lobed response characteristic of acoustically driven ferromagnetic resonance is discussed, and using low-loss piezoelectric transducers, the acoustically driven ferromagnetic resonance absorption is experimentally characterized. We show that the magnetoelastic absorption remains linear at milliwatt power levels; ensuring that input power can be increased in such devices in a such a way that does not preclude quantum coherence. Chapter 3 overviews the construction of a setup for characterization of NV centers driven by magnetoelastic waves. A comprehensive description of the equipment used, signal processing pathway, and optical design is provided, along with commentary on the design choices and underlying reasoning. Mechanical noise was the dominant concern in the system, and was partially addressed through the use of rigid materials and adjustment of optic mounting geometry. The magnetic field calibration methodology was also detailed, along with an example of the calibration dataset. Further room for improvement remains; should the setup be intended for use in characterization of single nitrogen vacancy centers, a 3-axis piezoelectric stage

would be used instead, and a confocal element would be added to ensure a sufficiently small depth of field. Chapter 4 overviews characterization of nanodiamond ensembles deposited on magnetoelastic devices. Owing to the specific requirements of acoustic drive, extremely small volumes of nanodiamond suspension needed to be deposited, necessitating the use of specialized equipment. Following a control measurement, datasets were collected displaying two replicable, but qualitatively distinct regimes of coupling between the magnetoelastic waves and NV centers. Using a model for dipolar field coupling, it was found that one regime matched the simulated dipolar response. The other regime contained an off-resonant response previously observed in studies of coupling of the ferromagnetic resonance mode. Finally, an initial study of a single-crystal diamond coupling was performed, indicating that the off-resonant response could be isolated by increasing NV-magnet spacing, and that acoustic scattering off nanodiamonds has a significant confounding impact on measurement data. These results motivated the studies discussed in Chapter 5, where to avoid these confounding acoustic effects, studies using a commercial single-NV scanning microscope were performed. Through these studies, the conditions where the linear and off-resonant coupling mechanisms dominated were identified, and it was shown that under exceptionally low microwave input power, it is possible to coherently drive transitions in the NV center via the dipolar fields of magnetoelastic waves. In addition, auxiliary studies showed that complex transient responses exist within the system, and that high laser light intensity can severely weaken the dipolar coupling mechanism.

6.2 Outlook for Future Work

Both ADFMR and the coupling between spin waves and NV centers have been studied heavily in recent years; however, many open questions remain within the field. While the addition of the work in this thesis provides an answer to some questions, multiple new research questions become self-evident with the addition of these results. Below, a discussion of some such approaches that the author sees as promising is provided, though this is by no means exhaustive.

Shear Wave Transducer Devices

While the work in this thesis was performed using the 128° YX-cut $LiNbO_3$ cut as an acoustic substrate, this is not a requirement, and is in fact suboptimal in some key ways. The dipolar coupling mechanism is strongest under the bias condition where magnetic field is perpendicular to the acoustic propagation, but this is the very condition where the longitudinal mode dominated Rayleigh wave mode is weakest. The electrically measured magnetic absorption is seen to be maximized under bias conditions where magnetoelastic "tickle" fields are maximized. This implies that, should a SAW mode be dominated by shear waves, the spin waves which couple to the NV center would be preferentially excited, potentially reducing power requirements even further.

A prime example of a potential shear device for studying ADFMR is based on the 36° YX-cut $LiTaO_3$ substrate, which supports a shear strain dominated SAW. Despite this, relatively few studies have explored this substrate, focusing on the Rayleigh mode structure. An example of shear-driven ADFMR on the 36° YX-cut $LiTaO_3$ substrate is given in [42], displaying an absorption resonance largely aligning with ADFMR theory. However, this substrate was, like with many Rayleigh-mode studies, driven at high harmonics, massively increasing insertion losses at the modes of interest.

The 128° YX-cut $LiNbO_3$ cut contains shear components approximately an order of magnitude weaker than the longitudinal component. If the hypothesis that these weaker shear components within the Rayleigh mode are responsible for the dipolar coupling seen in the results detailed in Chapter 5 is true, a hypothetical shear-mode device would be expected to excite comparable ODMR response and contrast at a microwave power two orders of magnitude lower than shown here. This would offer significant additional improvement in power consumption, and simultaneously reduce the impact of potential thermal or scattering effects from the main longitudinal resonance. Beyond the potential performance enhancements, the transition to a shear SAW substrate opens up a range of new applications in the biological space. Commercial liquid sensors based on shear SAW devices already exist [69], and rely on the fact that the shear waves are capable of propagating even when liquids such as water and blood are present on top of them. As such, this suggests the possibility that magnetoelastic devices can be an interface for magnetic field excitation in aqueous systems, or if the relevant biocompatibility challenges are addressed, the human body.

Patterned Magnetic Films and Biosensing

A critical advantage of acoustic excitation over a standard electromagnetic excitation of spin waves is the long coherence length of acoustic pulses. As a result, a hypothetical NV center device could function with magnetic pads localized to the single spot where the NV center is located, eliminating the challenge of high magnetic absorption, as power will only be dissipated in the nanoscale areas where NV centers are present. This is expected to introduce a range of complexities; surface anisotropy effects and quantum confinement are known to impact the magnetic states of such nanopatterned magnetic structures. However, if these complexities can be understood and taken into account in the design stage, this offers a potential pathway to integration of NV centers. Prior attempts to fully integrate an NV center based sensor have used small inductive coils [70], but nanopatterned magnetic features would be capable of excitation at even smaller scale.

Under appropriate design conditions, patterned magnetic films have also been shown to couple to magnetic nanoparticles, the detection of which has applications in medical diagnostics [71, 72]. Biosensing of magnetic nanoparticles through spin dynamics has been an active area of research for an extended period [73], but has primarily used magnetoresistive sensing techniques. The efficient excitation of magnetic dynamics via elastic waves potentially allows magnetic films to efficiently couple to a wide range of magnetic field sensitive systems, not limited to the NV center. Nanoparticles can contain significantly more spins than single

atom defects, suggesting that with the right signal processing scheme, the coupling may be detectable electrically in a manner similar to that of electron paramagnetic resonance.

Alternative Material Exploration

In addition to adjusting geometry of the magnetic film, the choice of alternative materials offers a possible performance improvement. All studies of NV coupling in this thesis were performed using Ni, in large part because of its well characterized ADFMR performance. However, multiple alternative magnetic materials display strong magnetostriction with narrower linewidth [31], including FeGaB and FeCoSiB. A stronger magnetostrictive coupling with low magnetic resonance damping would be expected to improve the strength of the acoustically excited spin wave response, in turn increasing the effective strength of the dipolar driving fields on any NV center in proximity.

Beyond the use of the NV center, a range of defect centers in carbon and silicon lattices have seen significant research interest in recent years. The NV center, while displaying excellent performance at room temperature and acting as a convenient laboratory system, remains challenging to practically integrate for a range of reasons. Diamond is traditionally incompatible with currently existing chip fabrication processes, though diamond-based MEMS processes are an active research area. A comprehensive overview of all alternative defect centers is well beyond the scope of this work, but any optically addressable defect center with a spin-dependent photoluminescence can in principle be excited but magnetoelastic waves. One potential example with a microwave spin transition within the typical ADFMR operation band is the silicon T-center [74].

Ultimately, the magnetoelastic excitation offers the capability to solve a critical power consumption challenge associated with drive of quantum systems in a manner compatible with existing chip fabrication technology. Such an approach enables significant material flexibility in the excitation of spin dynamics as well, opening pathways to wide-ranging research to optimize performance. While true defect-based quantum information processing remains a tremendous challenge, this thesis makes a small contribution to that goal. It is also the author's belief that, even if true quantum information processing remains a distant goal for years to come, the capability to excite highly localized microwave magnetic fields can find application in broader interdiscplinary fields in substantial and tangible ways.

Bibliography

[1] J.P. Joule. "On the effects of magnetism upon the dimensions of iron and steel bars". en. In: *The London, Edinburgh, and Dublin Philosophical Magazine and Journal of Science* 30.199 (Feb. 1847), pp. 76–87. ISSN: 1941-5966, 1941-5974. DOI: 10.1080/14786444708645656. URL: https://www.tandfonline.com/doi/full/10.1080/14786444708645656 (visited on 06/01/2023).

[2] C. Kittel. "Interaction of Spin Waves and Ultrasonic Waves in Ferromagnetic Crystals". In: *Physical Review* 110.4 (May 1958), pp. 836–841. DOI: 10.1103/PhysRev.110.836. URL: https://link.aps.org/doi/10.1103/PhysRev.110.836 (visited on 04/11/2018).

[3] H. Bömmel and K. Dransfeld. "Excitation of Hypersonic Waves by Ferromagnetic Resonance". In: *Physical Review Letters* 3.2 (July 1959). Publisher: American Physical Society, pp. 83–84. DOI: 10.1103/PhysRevLett.3.83. URL: https://link.aps.org/doi/10.1103/PhysRevLett.3.83 (visited on 01/12/2021).

[4] A. Coon. "SAW filters and competitive technologies: a comparative review". In: *IEEE 1991 Ultrasonics Symposium,* Dec. 1991, 155–160 vol.1. DOI: 10.1109/ULTSYM.1991.234146. (Visited on 11/08/2023).

[5] R. F. Wiegert and M. Levy. "Effects of gas exposure on the surface-acoustic-wave attenuation and magnetoresistance of nickel thin films". In: *Journal of Applied Physics* 67.9 (May 1990), pp. 4992–4994. ISSN: 0021-8979. DOI: 10.1063/1.344700. URL: https://doi.org/10.1063/1.344700 (visited on 11/08/2023).

[6] J.H. Collins. "A Short History of Microwave Acoustics". In: *IEEE Transactions on Microwave Theory and Techniques* 32.9 (Sept. 1984). Conference Name: IEEE Transactions on Microwave Theory and Techniques, pp. 1127–1140. ISSN: 1557-9670. DOI: 10.1109/TMTT.1984.1132824. URL: https://ieeexplore.ieee.org/document/1132824 (visited on 11/08/2023).

[7] Per Delsing et al. "The 2019 surface acoustic waves roadmap". en. In: *Journal of Physics D: Applied Physics* 52.35 (July 2019). Publisher: IOP Publishing, p. 353001. ISSN: 0022-3727. DOI: 10.1088/1361-6463/ab1b04. URL: https://dx.doi.org/10.1088/1361-6463/ab1b04 (visited on 11/29/2023).

[8] L. Dreher et al. "Surface acoustic wave driven ferromagnetic resonance in nickel thin films: Theory and experiment". In: *Physical Review B* 86.13 (Oct. 2012). Publisher: American Physical Society, p. 134415. DOI: 10.1103/PhysRevB.86.134415. URL: https://link.aps.org/doi/10.1103/PhysRevB.86.134415 (visited on 11/13/2023).

[9] N. A. Spaldin and R. Ramesh. "Advances in magnetoelectric multiferroics". en. In: *Nature Materials* 18.3 (Mar. 2019). Number: 3 Publisher: Nature Publishing Group, pp. 203–212. ISSN: 1476-4660. DOI: 10.1038/s41563-018-0275-2. URL: https://www.nature.com/articles/s41563-018-0275-2 (visited on 11/08/2023).

[10] Yao Wang et al. "Multiferroic magnetoelectric composite nanostructures". en. In: *NPG Asia Materials* 2.2 (Apr. 2010). Number: 2 Publisher: Nature Publishing Group, pp. 61–68. ISSN: 1884-4057. DOI: 10.1038/asiamat.2010.32. URL: https://www.nature.com/articles/am201054 (visited on 11/08/2023).

[11] G. Davies, M. F. Hamer, and William Charles Price. "Optical studies of the 1.945 eV vibronic band in diamond". In: *Proceedings of the Royal Society of London. A. Mathematical and Physical Sciences* 348.1653 (Jan. 1997). Publisher: Royal Society, pp. 285–298. DOI: 10.1098/rspa.1976.0039. URL: https://royalsocietypublishing.org/doi/10.1098/rspa.1976.0039 (visited on 11/09/2023).

[12] Marcus W. Doherty et al. "The nitrogen-vacancy colour centre in diamond". In: *Physics Reports* 528.1 (July 2013). arXiv:1302.3288 [cond-mat], pp. 1–45. ISSN: 03701573. DOI: 10.1016/j.physrep.2013.02.001. URL: http://arxiv.org/abs/1302.3288 (visited on 11/09/2023).

[13] J. R. Maze et al. "Properties of nitrogen-vacancy centers in diamond: the group theoretic approach". en. In: *New Journal of Physics* 13.2 (Feb. 2011), p. 025025. ISSN: 1367-2630. DOI: 10.1088/1367-2630/13/2/025025. URL: https://dx.doi.org/10.1088/1367-2630/13/2/025025 (visited on 12/03/2023).

[14] E. D. Herbschleb et al. "Ultra-long coherence times amongst room-temperature solid-state spins". en. In: *Nature Communications* 10.1 (Aug. 2019). Number: 1 Publisher: Nature Publishing Group, p. 3766. ISSN: 2041-1723. DOI: 10.1038/s41467-019-11776-8. URL: https://www.nature.com/articles/s41467-019-11776-8 (visited on 11/29/2023).

[15] J. R. Weber et al. "Quantum computing with defects". In: *Proceedings of the National Academy of Sciences* 107.19 (May 2010). Publisher: Proceedings of the National Academy of Sciences, pp. 8513–8518. DOI: 10.1073/pnas.1003052107. URL: https://www.pnas.org/doi/10.1073/pnas.1003052107 (visited on 12/03/2023).

[16] Kento Sasaki et al. "Broadband, large-area microwave antenna for optically detected magnetic resonance of nitrogen-vacancy centers in diamond". In: *Review of Scientific Instruments* 87.5 (May 2016), p. 053904. ISSN: 0034-6748. DOI: 10.1063/1.4952418. URL: https://doi.org/10.1063/1.4952418 (visited on 11/10/2023).

[17] Daisuke Nishitani et al. "Loop-gap microwave resonator for millimeter-scale diamond quantum sensor". In: *Materials Today Communications* 31 (June 2022), p. 103488. ISSN: 2352-4928. DOI: 10.1016/j.mtcomm.2022.103488. (Visited on 11/09/2023).

[18] Oliver Roman Opaluch et al. "Optimized Planar Microwave Antenna for Nitrogen Vacancy Center Based Sensing Applications". In: *Nanomaterials* 11.8 (Aug. 2021), p. 2108. ISSN: 2079-4991. DOI: 10.3390/nano11082108. URL: https://www.ncbi.nlm.nih.gov/pmc/articles/PMC8400909/ (visited on 11/09/2023).

[19] E. R. MacQuarrie et al. "Coherent control of a nitrogen-vacancy center spin ensemble with a diamond mechanical resonator". EN. In: *Optica* 2.3 (Mar. 2015). Publisher: Optica Publishing Group, pp. 233–238. ISSN: 2334-2536. DOI: 10.1364/OPTICA.2.000233. URL: https://opg.optica.org/optica/abstract.cfm?uri=optica-2-3-233 (visited on 11/27/2023).

[20] D. Andrew Golter et al. "Optomechanical Quantum Control of a Nitrogen-Vacancy Center in Diamond". In: *Physical Review Letters* 116.14 (Apr. 2016). Publisher: American Physical Society, p. 143602. DOI: 10.1103/PhysRevLett.116.143602. URL: https://link.aps.org/doi/10.1103/PhysRevLett.116.143602 (visited on 11/29/2023).

[21] Dany Lachance-Quirion et al. "Hybrid quantum systems based on magnonics". en. In: *Applied Physics Express* 12.7 (June 2019). Publisher: IOP Publishing, p. 070101. ISSN: 1882-0786. DOI: 10.7567/1882-0786/ab248d. URL: https://dx.doi.org/10.7567/1882-0786/ab248d (visited on 10/24/2023).

[22] David D. Awschalom et al. "Quantum Engineering With Hybrid Magnonic Systems and Materials (Invited Paper)". In: *IEEE Transactions on Quantum Engineering* 2 (2021). Conference Name: IEEE Transactions on Quantum Engineering, pp. 1–36. ISSN: 2689-1808. DOI: 10.1109/TQE.2021.3057799. URL: https://ieeexplore.ieee.org/document/9350187 (visited on 11/29/2023).

[23] Paolo Andrich et al. "Hybrid nanodiamond-YIG systems for efficient quantum information processing and nanoscale sensing". In: *npj Quantum Information* 3.1 (July 2017). arXiv:1701.07401 [cond-mat, physics:quant-ph], p. 28. ISSN: 2056-6387. DOI: 10.1038/s41534-017-0029-z. URL: http://arxiv.org/abs/1701.07401 (visited on 11/27/2023).

[24] Dominic Labanowski. "Acoustically Driven Ferromagnetic Resonance for Device Applications". PhD thesis. EECS Department, University of California, Berkeley, Dec. 2019. URL: http://www2.eecs.berkeley.edu/Pubs/TechRpts/2019/EECS-2019-142.html.

[25] Dominic Labanowski et al. "Voltage-driven, local, and efficient excitation of nitrogen-vacancy centers in diamond". In: *Science Advances* 4.9 (Sept. 2018). Publisher: American Association for the Advancement of Science, eaat6574. DOI: 10.1126/sciadv.

aat6574. URL: https://www.science.org/doi/10.1126/sciadv.aat6574 (visited on 11/28/2023).

[26] Georg Schmidt et al. "Ultra Thin Films of Yttrium Iron Garnet with Very Low Damping: A Review". en. In: *physica status solidi (b)* 257.7 (2020), p. 1900644. ISSN: 1521-3951. DOI: 10.1002/pssb.201900644. URL: https://onlinelibrary.wiley.com/doi/abs/10.1002/pssb.201900644 (visited on 10/25/2023).

[27] Denis R. Candido et al. "Predicted strong coupling of solid-state spins via a single magnon mode". en. In: *Materials for Quantum Technology* 1.1 (Dec. 2020). Publisher: IOP Publishing, p. 011001. ISSN: 2633-4356. DOI: 10.1088/2633-4356/ab9a55. URL: https://dx.doi.org/10.1088/2633-4356/ab9a55 (visited on 11/28/2023).

[28] M. Pomerantz. "Excitation of Spin-Wave Resonance by Microwave Phonons". In: *Physical Review Letters* 7.8 (Oct. 1961). Publisher: American Physical Society, pp. 312–313. DOI: 10.1103/PhysRevLett.7.312. URL: https://link.aps.org/doi/10.1103/PhysRevLett.7.312 (visited on 01/12/2021).

[29] D. Labanowski, A. Jung, and S. Salahuddin. "Power absorption in acoustically driven ferromagnetic resonance". In: *Applied Physics Letters* 108.2 (Jan. 2016), p. 022905. ISSN: 0003-6951. DOI: 10.1063/1.4939914. URL: https://doi.org/10.1063/1.4939914 (visited on 10/31/2023).

[30] R. Sasaki et al. "Nonreciprocal propagation of surface acoustic wave in Ni/$LiNbO_3$". In: *Physical Review B* 95.2 (Jan. 2017). Publisher: American Physical Society, p. 020407. DOI: 10.1103/PhysRevB.95.020407. URL: https://link.aps.org/doi/10.1103/PhysRevB.95.020407 (visited on 09/13/2020).

[31] Derek A. Bas et al. "Acoustically Driven Ferromagnetic Resonance in Diverse Ferromagnetic Thin Films". In: *IEEE Transactions on Magnetics* (2020), pp. 1–1. ISSN: 0018-9464, 1941-0069. DOI: 10.1109/TMAG.2020.3019214. URL: https://ieeexplore.ieee.org/document/9175006/ (visited on 09/23/2020).

[32] Matthias Küß et al. "Nonreciprocal Dzyaloshinskii-Moriya magnetoacoustic waves". In: *arXiv:2004.03535 [cond-mat]* (Apr. 2020). arXiv: 2004.03535. URL: http://arxiv.org/abs/2004.03535 (visited on 09/13/2020).

[33] Piyush J. Shah et al. "Giant Nonreciprocity of Surface Acoustic Waves enabled by the Magnetoelastic Interaction". In: *arXiv:2004.14190 [cond-mat, physics:physics]* (Apr. 2020). arXiv: 2004.14190. URL: http://arxiv.org/abs/2004.14190 (visited on 09/13/2020).

[34] Mingran Xu et al. "Nonreciprocal surface acoustic wave propagation via magneto-rotation coupling". In: *Science Advances* 6.32 (Aug. 2020). Publisher: American Association for the Advancement of Science, eabb1724. DOI: 10.1126/sciadv.abb1724. URL: https://www.science.org/doi/10.1126/sciadv.abb1724 (visited on 11/29/2023).

[35] P. F. Bordui et al. "Chemically reduced lithium niobate single crystals: Processing, properties and improved surface acoustic wave device fabrication and performance". In: *Journal of Applied Physics* 85.7 (Apr. 1999), pp. 3766–3769. ISSN: 0021-8979. DOI: 10.1063/1.369775. URL: https://doi.org/10.1063/1.369775 (visited on 11/11/2023).

[36] Waldemar Soluch and Magdalena Lysakowska. "Surface acoustic waves on X-cut LiNbO 3". In: *IEEE transactions on ultrasonics, ferroelectrics, and frequency control* 52.1 (Jan. 2005), pp. 145–147. ISSN: 0885-3010. DOI: 10.1109/tuffc.2005.1397360.

[37] David Morgan. *Surface Acoustic Wave Filters with Applications to Electronic Communications and Signal Processing*. 2nd ed. Elsevier Ltd, 2007. ISBN: 978-0-12-372537-0.

[38] A.J. Slobondik, E.D. Conway, and R.T. Delmonico. *Microwave Acoustics Handbook: Surface wave velocities*. Vol. 1A. Air force Cambridge research laboratories, 1973. URL: https://books.google.com/books?id=7ygjzQEACAAJ.

[39] A. W. Warner, M. Onoe, and G. A. Coquin. "Determination of Elastic and Piezoelectric Constants for Crystals in Class (3m)". In: *The Journal of the Acoustical Society of America* 42.6 (Dec. 1967). Publisher: Acoustical Society of America, pp. 1223–1231. ISSN: 0001-4966. DOI: 10.1121/1.1910709. URL: https://asa.scitation.org/doi/abs/10.1121/1.1910709 (visited on 09/20/2020).

[40] Ken-ya Hashimoto. *Surface Acoustic Wave Devices in Telecommunications*. en. Berlin, Heidelberg: Springer, 2000. ISBN: 978-3-642-08659-5 978-3-662-04223-6. DOI: 10.1007/978-3-662-04223-6. URL: http://link.springer.com/10.1007/978-3-662-04223-6 (visited on 11/11/2023).

[41] Jorge Puebla et al. "Acoustic ferromagnetic resonance and spin pumping induced by surface acoustic waves". en. In: *Journal of Physics D: Applied Physics* 53.26 (May 2020). Publisher: IOP Publishing, p. 264002. ISSN: 0022-3727. DOI: 10.1088/1361-6463/ab7efe. URL: https://doi.org/10.1088%2F1361-6463%2Fab7efe (visited on 07/06/2020).

[42] Matthias Pernpeintner. "Magnon-Phonon Coupling in Ferromagnetic Thin Films". PhD thesis. Walther-Meißner-Institute for Low Temperature Research. URL: http://www.wmi.badw.de/publications/theses/Pernpeintner,Matthias_Diplomarbeit.pdf (visited on 09/20/2020).

[43] Soshin Chikazumi. *Physics of Ferromagnetism*.

[44] Thomas L. Gilbert. "A phenomenological theory of damping in ferromagnetic materials". In: *IEEE Transactions on Magnetics* 40.6 (Nov. 2004), pp. 3443–3449. ISSN: 0018-9464. DOI: 10.1109/TMAG.2004.836740. URL: https://ieeexplore.ieee.org/document/1353448 (visited on 11/12/2023).

[45] M. Weiler et al. "Elastically Driven Ferromagnetic Resonance in Nickel Thin Films". In: *Physical Review Letters* 106.11 (Mar. 2011). Publisher: American Physical Society, p. 117601. DOI: 10.1103/PhysRevLett.106.117601. URL: https://link.aps.org/doi/10.1103/PhysRevLett.106.117601 (visited on 02/15/2021).

[46] Haimei Zhang et al. "Little bits of diamond: Optically detected magnetic resonance of nitrogen-vacancy centers". In: *American Journal of Physics* 86.3 (Mar. 2018), pp. 225–236. ISSN: 0002-9505. DOI: 10.1119/1.5023389. URL: https://doi.org/10.1119/1.5023389 (visited on 11/28/2023).

[47] Yiwen Chu and Mikhail D. Lukin. *Quantum optics with nitrogen-vacancy centers in diamond*. arXiv:1504.05990 [quant-ph]. Apr. 2015. DOI: 10.48550/arXiv.1504.05990. URL: http://arxiv.org/abs/1504.05990 (visited on 11/28/2023).

[48] Donna J. Webb and Claire M. Brown. "Epi-Fluorescence Microscopy". In: *Methods in molecular biology (Clifton, N.J.)* 931 (2013), pp. 29–59. ISSN: 1064-3745. DOI: 10.1007/978-1-62703-056-4_2. URL: https://www.ncbi.nlm.nih.gov/pmc/articles/PMC3483677/ (visited on 12/12/2023).

[49] E. A. Donley et al. "Double-pass acousto-optic modulator system". en. In: *Review of Scientific Instruments* 76.6 (June 2005), p. 063112. ISSN: 0034-6748, 1089-7623. DOI: 10.1063/1.1930095. URL: http://aip.scitation.org/doi/10.1063/1.1930095 (visited on 12/12/2018).

[50] Masaya Fukami et al. "Opportunities for Long-Range Magnon-Mediated Entanglement of Spin Qubits via On- and Off-Resonant Coupling". In: *PRX Quantum* 2.4 (Oct. 2021). Publisher: American Physical Society, p. 040314. DOI: 10.1103/PRXQuantum.2.040314. URL: https://link.aps.org/doi/10.1103/PRXQuantum.2.040314 (visited on 11/28/2023).

[51] M. R. Page et al. "Optically detected ferromagnetic resonance in diverse ferromagnets via nitrogen vacancy centers in diamond". In: *Journal of Applied Physics* 126.12 (Sept. 2019), p. 124902. ISSN: 0021-8979. DOI: 10.1063/1.5083991. URL: https://doi.org/10.1063/1.5083991 (visited on 11/28/2023).

[52] M. S. Wolf, R. Badea, and J. Berezovsky. "Fast nanoscale addressability of nitrogen-vacancy spins via coupling to a dynamic ferromagnetic vortex". en. In: *Nature Communications* 7.1 (June 2016). Number: 1 Publisher: Nature Publishing Group, p. 11584. ISSN: 2041-1723. DOI: 10.1038/ncomms11584. URL: https://www.nature.com/articles/ncomms11584 (visited on 11/28/2023).

[53] Iacopo Bertelli et al. "Magnetic resonance imaging of spin-wave transport and interference in a magnetic insulator". In: *Science Advances* 6.46 (Nov. 2020). Publisher: American Association for the Advancement of Science, eabd3556. DOI: 10.1126/sciadv.abd3556. URL: https://www.science.org/doi/10.1126/sciadv.abd3556 (visited on 02/27/2023).

[54] Chunhui Du et al. "Control and local measurement of the spin chemical potential in a magnetic insulator". In: *Science* 357.6347 (July 2017). Publisher: American Association for the Advancement of Science, pp. 195–198. DOI: 10.1126/science.aak9611. URL: https://www.science.org/doi/10.1126/science.aak9611 (visited on 11/28/2023).

[55] E. R. MacQuarrie et al. "Continuous dynamical decoupling of a single diamond nitrogen-vacancy center spin with a mechanical resonator". In: *Physical Review B* 92.22 (Dec. 2015). Publisher: American Physical Society, p. 224419. DOI: 10.1103/PhysRevB.92.224419. URL: https://link.aps.org/doi/10.1103/PhysRevB.92.224419 (visited on 11/27/2023).

[56] Akashdeep Kamra et al. "Coherent elastic excitation of spin waves". In: *Physical Review B* 91.10 (Mar. 2015). Publisher: American Physical Society, p. 104409. DOI: 10.1103/PhysRevB.91.104409. URL: https://link.aps.org/doi/10.1103/PhysRevB.91.104409 (visited on 10/31/2023).

[57] Frederic Vanderveken, Florin Ciubotaru, and Christoph Adelmann. "Magnetoelastic Waves in Thin Films". en. In: *Chirality, Magnetism and Magnetoelectricity: Separate Phenomena and Joint Effects in Metamaterial Structures*. Ed. by Eugene Kamenetskii. Topics in Applied Physics. Cham: Springer International Publishing, 2021, pp. 287–322. ISBN: 978-3-030-62844-4. DOI: 10.1007/978-3-030-62844-4_12. URL: https://doi.org/10.1007/978-3-030-62844-4_12 (visited on 11/28/2023).

[58] Tomosato Hioki, Yusuke Hashimoto, and Eiji Saitoh. "Coherent oscillation between phonons and magnons". en. In: *Communications Physics* 5.1 (May 2022). Number: 1 Publisher: Nature Publishing Group, pp. 1–8. ISSN: 2399-3650. DOI: 10.1038/s42005-022-00888-1. URL: https://www.nature.com/articles/s42005-022-00888-1 (visited on 11/28/2023).

[59] Tao Yu et al. "Chiral excitation of spin waves in ferromagnetic films by magnetic nanowire gratings". In: *Physical Review B* 99.13 (Apr. 2019). Publisher: American Physical Society, p. 134424. DOI: 10.1103/PhysRevB.99.134424. URL: https://link.aps.org/doi/10.1103/PhysRevB.99.134424 (visited on 12/29/2022).

[60] Keunhong Jeong et al. "Understanding the Magnetic Resonance Spectrum of Nitrogen Vacancy Centers in an Ensemble of Randomly Oriented Nanodiamonds". In: *The Journal of Physical Chemistry C* 121.38 (Sept. 2017). Publisher: American Chemical Society, pp. 21057–21061. ISSN: 1932-7447. DOI: 10.1021/acs.jpcc.7b07247. URL: https://doi.org/10.1021/acs.jpcc.7b07247 (visited on 12/29/2022).

[61] C. S. Wolfe et al. "Spatially resolved detection of complex ferromagnetic dynamics using optically detected nitrogen-vacancy spins". In: *Applied Physics Letters* 108.23 (June 2016), p. 232409. ISSN: 0003-6951. DOI: 10.1063/1.4953108. URL: https://doi.org/10.1063/1.4953108 (visited on 11/23/2023).

[62] C. S. Wolfe et al. "Off-resonant manipulation of spins in diamond via precessing magnetization of a proximal ferromagnet". In: *Physical Review B* 89.18 (May 2014). Publisher: American Physical Society, p. 180406. DOI: 10.1103/PhysRevB.89.180406. URL: https://link.aps.org/doi/10.1103/PhysRevB.89.180406 (visited on 02/23/2023).

[63] K.R. Williams, K. Gupta, and M. Wasilik. "Etch rates for micromachining processing-Part II". In: *Journal of Microelectromechanical Systems* 12.6 (2003), pp. 761–778. DOI: 10.1109/JMEMS.2003.820936.

[64] P. L. Stanwix et al. "Coherence of nitrogen-vacancy electronic spin ensembles in diamond". In: *Physical Review B* 82.20 (Nov. 2010). Publisher: American Physical Society, p. 201201. DOI: 10.1103/PhysRevB.82.201201. URL: https://link.aps.org/doi/10.1103/PhysRevB.82.201201 (visited on 11/27/2023).

[65] B. D. Wood et al. "Long spin coherence times of nitrogen vacancy centers in milled nanodiamonds". In: *Physical Review B* 105.20 (May 2022). Publisher: American Physical Society, p. 205401. DOI: 10.1103/PhysRevB.105.205401. URL: https://link.aps.org/doi/10.1103/PhysRevB.105.205401 (visited on 11/29/2023).

[66] Thomas Sebastian et al. "Micro-focused Brillouin light scattering: imaging spin waves at the nanoscale". In: *Frontiers in Physics* 3 (2015). ISSN: 2296-424X. URL: https://www.frontiersin.org/articles/10.3389/fphy.2015.00035 (visited on 11/29/2023).

[67] Nandan K. P. Babu et al. "The Interaction between Surface Acoustic Waves and Spin Waves: The Role of Anisotropy and Spatial Profiles of the Modes". In: *Nano Letters* 21.2 (Jan. 2021), pp. 946–951. ISSN: 1530-6984. DOI: 10.1021/acs.nanolett.0c03692. URL: https://www.ncbi.nlm.nih.gov/pmc/articles/PMC7844825/ (visited on 11/29/2023).

[68] Vitaly Yaroshenko et al. "Circularly polarized microwave antenna for nitrogen vacancy centers in diamond". In: *Review of Scientific Instruments* 91.3 (Mar. 2020), p. 035003. ISSN: 0034-6748. DOI: 10.1063/1.5129863. URL: https://doi.org/10.1063/1.5129863 (visited on 11/29/2023).

[69] Chia-Hsuan Cheng et al. "Application of Shear Horizontal Surface Acoustic Wave (SH-SAW) Immunosensor in Point-of-Care Diagnosis". en. In: *Biosensors* 13.6 (June 2023). Number: 6 Publisher: Multidisciplinary Digital Publishing Institute, p. 605. ISSN: 2079-6374. DOI: 10.3390/bios13060605. URL: https://www.mdpi.com/2079-6374/13/6/605 (visited on 12/02/2023).

[70] Donggyu Kim et al. "A CMOS-integrated quantum sensor based on nitrogen–vacancy centres". en. In: *Nature Electronics* 2.7 (July 2019). Number: 7 Publisher: Nature Publishing Group, pp. 284–289. ISSN: 2520-1131. DOI: 10.1038/s41928-019-0275-5. URL: https://www.nature.com/articles/s41928-019-0275-5 (visited on 11/30/2023).

[71] Teresa A. P. Rocha-Santos. "Sensors and biosensors based on magnetic nanoparticles". In: *TrAC Trends in Analytical Chemistry* 62 (Nov. 2014), pp. 28–36. ISSN: 0165-9936. DOI: 10.1016/j.trac.2014.06.016. URL: https://www.sciencedirect.com/science/article/pii/S0165993614001617 (visited on 11/29/2023).

[72] P. J. Metaxas et al. "Sensing magnetic nanoparticles using nano-confined ferromagnetic resonances in a magnonic crystal". In: *Applied Physics Letters* 106.23 (June 2015), p. 232406. ISSN: 0003-6951. DOI: 10.1063/1.4922392. URL: https://doi.org/10.1063/1.4922392 (visited on 11/29/2023).

[73] P. P. Freitas et al. "Spintronic platforms for biomedical applications". en. In: *Lab on a Chip* 12.3 (Jan. 2012). Publisher: The Royal Society of Chemistry, pp. 546–557. ISSN: 1473-0189. DOI: 10.1039/C1LC20791A. URL: https://pubs.rsc.org/en/content/articlelanding/2012/lc/c1lc20791a (visited on 11/29/2023).

[74] L. Bergeron et al. *Characterization of the T center in ^{28}Si*. arXiv:2006.08794 [cond-mat]. June 2020. DOI: 10.48550/arXiv.2006.08794. URL: http://arxiv.org/abs/2006.08794 (visited on 11/27/2023).